Systems Approaches to Enhance Performance and Applicability of Microbial Fuel Cells

Hitesh Chandubhai Boghani

PhD Thesis

A submission presented in partial fulfilment of the requirements of the University of South Wales/Prifysgol De Cymru for the degree of Doctor of Philosophy

October 2014

Dedication

My God is none other than my parents who gave me life, and my teachers in all forms who enlightened me with their knowledge, experience and wisdom; to whom I dedicate my work, my religion (Dharma).

Acknowledgement

I would like to sincerely thank all those who have directly or indirectly supported me in pursuing my postgraduate research study. I would like to express my sincere gratitude to my Director of Studies, ***Professor Giuliano C. Premier*** for providing me the opportunity to carry out research in Microbial Fuel Cells, his unquestionable immense technical and moral support and guidance, his meticulous supervision and for also believing in me. I consider him my *Guru* and my 'role model' and without him my research would not have been possible. I would also like to thank the following for their contribution, technical and moral support, help and advice.

Prof. Richard M. Dinsdale	Supervisor	University of South Wales
Prof. Alan J. Guwy	Supervisor	University of South Wales
Dr. Jung Rae Kim	Assistant Professor	University of Pusan
Ms. Katrin R. Fradler	Research student	University of South Wales
Ms. Amandeep Kaur	Research student	University of South Wales
Dr. Iain Michie	Post-doctoral researcher	University of South Wales
Mr. Arseniy Popov	Research student	University of South Wales
Ms. Romane Wilders	Project student	ERASMUS student
Mr. Paul Marshman	Higher technical officer	University of South Wales
The staff at Sustainable Environment Research Centre (SERC)		University of South Wales
The staff at Graduate Research Office (GRO)		University of South Wales
The technicians at manufacturing workshop		University of South Wales

I would like to extend my gratitude further to EPSRC for funding the project under Supergen Biological Fuel Cell Consortium (project grant: EP/H019480/1) which made this work possible.

Furthermore, I would like to thank my parents *Manjulaben* and *Chandubhai Boghani*, my sister *Asmita Kachhadiya*, my brother-in-law *Mallikarjun Kachhadiya*, my brother *Hiren* and my lovely wife *Bhagvati* for their belief in me, their moral support, sacrifices, patience and providing motivation to pursue further studies against all the odds and reach higher altitude.

Likewise, my thanks go to all my friends without a doubt, for their moral support and motivation.

The algorithm for maximum power point tracking on microbial fuel cells presented in this study (Chapter 3 and 4) utilised sub-routines to control the digital potentiometers which was written by *Prof. Giuliano C. Premier*.

Tubular reactors used in the study presented in Chapter 5 were maintained by *Ms. Katrin Fradler* for more than a year prior to the experimentation and; molecular analysis on the anodic biofilm in the voltage reversal experiments was performed by *Dr. Iain Michie* and I thank them for their contributions. Also, I would like to thank *Mr. George Papaharalabos*, *Dr. Ioannis Ieropoulos* and *Prof. John Greenman* from the University of West of England, for providing the opportunity through the collaboration under the Supergen Biological Fuel Cell Consortium, to test the microbial fuel cell stack connectivity strategy on their reactors.

The concept of helical anode design (Chapter 6) was conceived by *Prof. Giuliano C. Premier* and developed through undergraduate projects at the University of Glamorgan from 2007 to 2010.

Abstract

Wastewater treatment is an energy intensive process and sustainable processes/technologies for the treatment of wastewaters need to be considered. One such contender might be the microbial fuel cell (MFC), a subset of bioelectrochemical system (BES) which generates electricity in the process of electrogenic (generating electrons) degradation of soluble organic contaminants present in the water (or wastewater) by electrogens (electron producing bacteria) at the anode in absence of oxygen. Several issues related to the power performance (also somewhat linked to the cost) of MFCs exist causing barriers in the deployment of up-scaled MFC system and the continual research from a multitude of discipline is focusing on overcoming these issues.

Implementation of an MFC system for wastewater treatment would require a large array of MFCs to meet the treatment capacity of the wastewater treatment plant. Commissioning and continual operation of such MFCs would require rapid and cost-effective start-up and improvement in their performance. Optimisation of the power performance is addressed through a systems approach in this study, where improvement in the performance is sought through the system design and control strategies applied to the MFCs. The start-up rate of MFCs has been reduced by 45% using maximum power point tracking (MPPT), which is believed to be cost-effective as exogenous energy (such as in the case of poised-potential) is not required for the rapid start-up. The control of MFC power would need to be considered when up-scaled MFC system is realised. The controller implementation benefits from linearised system models. The viability of such piecewise linearisation of the nonlinear MFC system was demonstrated and the data were shown to be reasonably represented by the 1st order process models throughout its operating range. The occurrence of voltage reversal during stack operation of MFCs is a concern in large arrays particularly, and has been shown to be avoidable by adopting the hybrid stack connectivity. Further enhancement of the performance was sought through the detailed design and fluid dynamics modeling to obtain highly mixed anolyte at low input power, using improved helical anodes which increased the MFC performance at all the tested flow rates (1, 3 and 8 mL min^{-1}) compared to previously studied helical anodes. The up-scaling of MFCs by modularisation was demonstrated and it was shown that the use of improved helical anodes can increase the modular length of the MFC without compromising the power performance. Aggregated power produced from the multi-module MFC (containing 5 modules) was 28.05 ± 3.5 mW (19.75 ± 2.47 W m^{-3}) with an

individual MFC power of 5.61 ± 0.7 mW, when fed with 10 mM sodium acetate at 3 mL min^{-1} flow rate and at 22 ± 3 °C.

So, this thesis presents the strategies for improvement in the performance of MFCs for their applications in wastewater treatment and such strategies may also be transferable to their other applications.

Table of Contents

List of figures

List of tables

Abbreviations

2D	Two dimension(al)
3D	Three dimension(al)
Ac^-	Acetate
ACP-HFC	Alternate Converging Plates in Helical Fluid Channel
AD	Anaerobic Digester
An	Anode
ARX	AutoRegressive with eXtra inputs
BES	Bioelectrochemical System
Cath	Cathode
CEM	Cation Exchange Membrane
CFD	Computational Fluid Dynamics
COD	Chemical Oxygen Demand
CP-HFC	Converging Plates in Helical Fluid Channel
CP-SFC	Converging Plates in Straight Fluid Channel
CS	Case Study
CV	Cyclic Voltammetry
EIS	Electrochemical Impedance Spectroscopy
emf	Electromotive force
GHG	Greenhouse Gas
HFC	Helical Fluid Channel
MEA	Membrane Electrode Assembly
Med	Mediator
MFC	Microbial Fuel Cell

MMCC	Micro-porous Monolith Conductive Carbon
MPP	Maximum Power Point
MPPT	Maximum Power Point Tracking
Mtoe	Million tonnes of oil equivalent
OCV	Open Circuit Voltage
OLR	Organic Loading Rate
PEM	Proton Exchange Membrane
PEMFC	Proton Exchange Membrane Fuel Cell
P-HFC	Pillars in Helical Fluid Channel
PRBS	Pseudo-Random Binary Signal
P-SFC	Pillars in Straight Fluid Channel
PTFE	Polytetrafluoroethylene
RC	Resistance-Capacitance
RVC	Reticulated Vitreous Carbon
SFC	Straight Fluid Channel
SIM	Simulation
SOFC	Solid Oxide Fuel Cells
STP	Standard temperature and pressure
TTL	Transistor-transistor logic
UASB	Upflow Anaerobic Sludge Blanket
UMFC	Upflow Microbial Fuel Cell
VFA	Volatile Fatty Acids

Nomenclature

Symbol	Description	Unit
E_{emf}	Cell electromotive force	V
E^0_{emf}	Standard cell emf	V
R	Universal gas constant	J mol^{-1} K^{-1}
T	Temperature	K
n	Number of electrons	Dimensionless
F	Faraday constant	C mol^{-1}
π	The reaction quotient	Dimensionless
$E_{cathode}$	Potential of the cathode half-cell	V
E_{anode}	Potential of the anode half-cell	V
E_{cell}	Theoretical cell emf	V
η_{an}	Overpotential occurring at the anode	V
η_{cat}	Overpotential occurring at the cathode	V
I or i	Electrical current	A
P	Electrical power	W
R_Ω	Internal resistance of the MFC	Ω
j_{an}	Internal currents at the anode	A
r_{an}	Internal resistance of the part section of the anode	Ω
j_{cat}	Internal currents at the cathode	A
r_{cat}	Internal resistance of the part section of the cathode	Ω
S_p	Positive slope of the power curve	W A^{-1}
S_n	Negative slope of the power curve	W A^{-1}
dS_p	Positive rate of change of slope of the power curve	W A^{-2}

dS_n	Negative rate of change of slope of the power curve	W A^{-2}
Inc	Increase the load	-
Dec	Decrease the load	-
Con	No change in the load, constant	-
MFC-PP-MPPT	MFC operated on load controlled by maximum power point tracking (MPPT) algorithm preceded by poised-potential	-
MFC-MPPT	MFC operated on load controlled by the MPPT algorithm	-
MFC-*Control*	MFC operated on a constant electrical load for comparison in Chapter 3	-
$i_{threshold}$	Threshold current	A
V_{sys}	MFC voltage	V
E_{poised}	Poised-potential	V
$t_{timeOut}$	Time-out	sec
t	Time	sec
V	Voltage	V
R	Electrical resistance	Ω
V_o	Voltage output	V
R_i	Input load	Ω
s	Laplace variable	-
k or K	Steady-state gain	mV $Ω^{-1}$
T_p or τ	Time constant	sec
t-MFC	Tubular MFC studied in Chapter 4	-
ρ	Density of the fluid	kg m^{-3}
$\mathbf{u}$	Velocity vector	m s^{-1}
∇	Vector differential operator	-

p	Pressure	Pa
$\mathbf{I}$	Identity matrix	-
μ	Dynamic viscosity	kg m^{-1} s^{-1}
$\boldsymbol{T}$	Transpose	-
ε_{p}	Porosity, the ratio of void volume to the total volume	Dimensionless
K_{br}	Permeability of the porous medium	m^2
j	Chemical species, acetate (ac) or proton (H^+)	-
D_j	Diffusion coefficient for the species *j*	m^2 s^{-1}
c_j	Concentration of the species *j*	mol m^{-3}
R_j	Reaction rate expression for the chemical species *j*	mol m^{-3} s^{-1}
N_j	Concentration flux into or out of the surrounding environment	mol m^{-2} s^{-1}
$R^e_{ac,max}$	Volumetric consumption rate of acetate by electrogens	mol m^{-3} s^{-1}
K^e_{ac}	Half-saturation constant of acetate degradation into electrons	mol m^{-3}
c_{ac}	Concentration of acetate	mol m^{-3}
c_{H^+}	Concentration of protons (H^+)	mol m^{-3}
S_{outlet}	Mixing ratio	Dimensionless
$\boldsymbol{n}$	Normal vector	-
x, y and z	Cartesian coordinates	-
O1-MFC	Only 1 MFC	-
2P-MFC	MFC 1 and 2 in parallel	-
3P-MFC	MFC 1, 2 and 3 in parallel	-
4P-MFC	MFC 1, 2, 3 and 4 in parallel	-
ϵ_c	Coulombic efficiency	Dimensionless

C_{gen}	Coulombs generated	C
C_{th}	Theoretical coulombs	C
t_{lag}	Time taken in the lag phase	sec
$t_{s.r.}$	Time taken in the slow rise phase	sec
$t_{f.r}$	Time taken in the fast rise phase	sec
t_{stbl}	Time taken in the stabilisation phase	sec
t_{total}	Total time taken to reach the steady-state	sec
$R_{f.r.}$	Rate of voltage rise during the fast rise phase	V d^{-1}
$R_{s.r}$	Rate of voltage rise during the slow rise phase	V d^{-1}
m	Coefficient of phase time per module	day unit- $length^{-1}$
l	Position of the MFC in multi-module MFC	unit-length
c	Intercept considered as the bias time, linear curve fitting in Chapter 7	day
a	Coefficient of voltage rise	V day^{-1}
b	Normalisation factor for length	unit-$lenth^{-1}$

1. Introduction

World energy demand has been increasing, particularly since the industrial revolution and is forecast to increase 56% by 2040 according to the International Energy Agency (2013). Depleting fossil fuel reserves, security of supply and greenhouse gas (GHG) emissions make alternative renewable and sustainable energy sources highly desirable, and considerable international efforts are being expended in their pursuit. Ever growing world population would require more and more of the water supply for drinking, domestic, industrial and agricultural usages and also impact the environment due to water pollution. Therefore, removal of pollutants and recycling of water through the treatment of wastewater is important to meet the safe water discharge limit and the water supply demand but it is currently an energy intensive process. About 3% of produced electricity in the UK is used by the water industry (Rothausen and Conway, 2011). This includes the treatment of industrial and municipal wastewaters and as of the year 2012, the UK government statistics report suggests that the water industry had utilised 4.446 million tonnes of oil equivalent (Mtoe) of energy in year 2012, which is substantial amount of energy consumption. Bearing in mind that the fossil fuels are depleting, a more sustainable energy source through the renewable energy and/or sustainable processes must be innovated and implemented to sustain and meet the energy demand. In the treatment of wastewaters, the energy is predominantly used in aeration (typically 60%) to sustain the aerobic biological processes that are most commonly used processes and in pumping (typically 30%) of the wastewater (Brandt et al., 2010). A shift to anaerobic technologies for the wastewater treatment therefore, could save much of the electrical energy usage by the wastewater treatment plants.

Microbial Fuel Cell (MFC), a type of Bioelectrochemical System (BES) represent promising emerging anaerobic treatment for wastewaters, which can degrade organic substrate and produce electricity directly, to enhance cost effectiveness and energy autonomy. While they may use oxygen from the atmosphere, they are not expected to require forced aeration and will recover energy available from wastewaters they treat. MFCs can operate at low substrate concentration which makes it attractive as it may find applications integrated into anaerobic digester (AD) utilising the end product (rich in volatile fatty acids, VFAs) of AD (Fradler et al., 2014a). The present form of MFC technology is limited in power and they may not achieve the power levels of conventional fuel cells but, concomitant recovery of energy in terms of electricity during the treatment of wastewaters along with the absence of forced aeration and is certainly an attractive part. Much of the research is focused in augmentation of

power from MFCs and the MFC scalability to be able to compete or at least supplement the existing wastewater treatment technologies.

An MFC consists of an anode and cathode frequently separated by an ion exchange membrane with several architectural, material and operational variations (discussed later in Chapter 2). The anode compartment usually contains organic substrate (carbon source), buffer medium (to maintain near neutral pH), electrogenic bacteria (electron generating bacteria, biocatalyst) either in suspension or an attached biofilm on the electrode. The cathode provides the terminal electron acceptor which may be an oxidant such as ferricyanide, or atmospheric oxygen. The reduction process may be catalysed by e.g. Pt, Co based alloys or biological systems. At the anode electrode, electrons liberated from oxidation of carbon based substrate by the electrogens are transported to the electrode; directly via pili (or nano-wires) or cytochrome matrix; or indirectly via electron shuttles (also called mediators) as shown

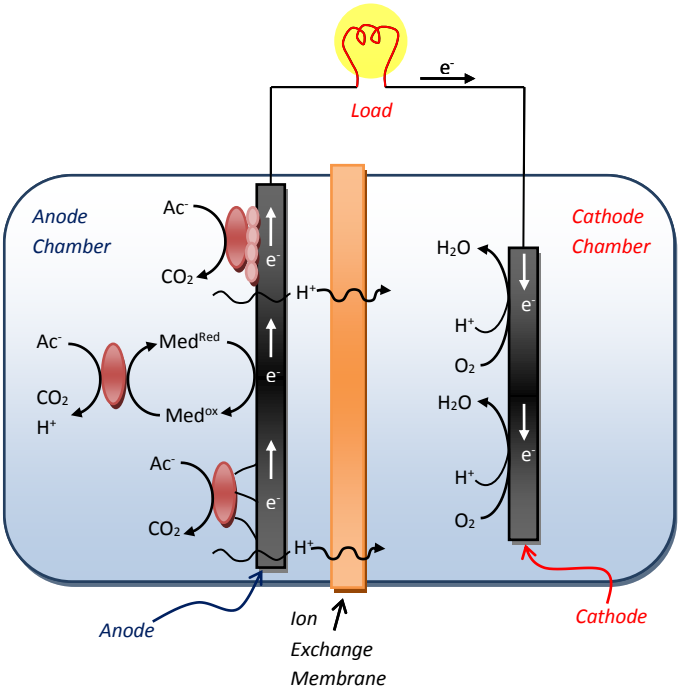

Figure 1.1: Schematic of a typical microbial fuel cell (MFC).

in Figure 1.1. The electrons are then transferred to the cathode electrode via external circuit (load) where they are accepted by electron acceptor which is being reduced with the help of catalyst.

MFCs are limited by their performance, to be able to compete with conventional wastewater process (Oh et al., 2010) or conventional fuel cells with power densities in the ranges of kW m^{-3} (Kirubakaran et al., 2009); as opposed to the range of a few hundred W m^{-3} in

MFCs (Ringeisen et al., 2006). However, due to the organic/inorganic matter degradation capabilities of MFCs, their potential application lies predominantly in the treatment of wastes (Allen and Bennetto, 1993, Ieropoulos et al., 2010, Katuri and Scott, 2010, Kim et al., 2010, Oh et al., 2010, Zhuang et al., 2012b) and have potential to contribute to sustainable wastewater treatment processes. The potential uses of derivative BES processes include hydrogen and other reduced substance production (Manuel et al., 2010, Sun et al., 2009), biosensors (Chang et al., 2004, Yoshida et al., 2000, Di Lorenzo et al., 2009b, Kaur et al., 2013), toxicity sensor (Dávila et al., 2011, Di Lorenzo et al., 2014), recovery of dissolved metals from wastewater (Fradler et al., 2014b, Choi and Cui, 2012, Zhang et al., 2012) and desalination (Cao et al., 2009), all of which may benefit from developments derived from this study.

When considering MFC systems for wastewater treatment plants, a large array of MFCs would be required, given current MFC arrangements. Commissioning of the MFCs to their full operational status at which they reach their highest achievable performance, is expected to be limited by time, which can increase the capital and the operational expenses. Also, enhancements in MFC performance and unimpaired performance from stacked MFC arrays are desirable in order to control operational costs. Keeping these considerations in mind, the following objectives were set.

1. To improve the MFC start-up time and the performance. Decreasing the start-up time and simultaneously improving performance may be beneficial for the MFC's rapid deployment and applicability in wastewater treatment.
2. To model the MFC process and obtain simple models that represent input/output relationships, applicable in the design and implementation of control.
3. To investigate the MFC stack performance and to avoid adverse effects, particularly voltage reversal, during the stack operation of the MFCs.
4. To improve the performance of MFCs through optimisation of the anode; using engineering design and analysis tools and techniques.
5. Having fulfilled objective 4, to build a pilot scale MFC system and analyse its power performance with respect to its use in the wastewater treatment with simultaneously electrical energy generation.

This study sought to optimise and improve the performance of MFCs in terms of the power output, for projected application to the treatment of wastewaters. It is expected that the enhancement of the power performance will affect the chemical oxygen demand (COD) removal and so the treatment efficiency, as the higher power generation (through higher

electron generation due to the oxidation of organic contaminants by the electrogens) is related to greater COD removal. However, COD removal efficiency was not investigated in this study as it was to be investigated in the parallel PhD studies of a colleague, Ms. Katrin Fradler, also working on the same project as the author (UKERC SUPERGEN Biological Fuel Cell Consortium project, grant: EP/H019480/1).

1.1 Structure and organisation of the thesis

Since the 'materials and methods' were largely distinct for each objectives/tasks listed above, the relevant information on materials utilised in the experimentation/modeling and the methodologies used are provided within the chapters concerning the study. In view of the retaining relevant information and keeping the links to the 'materials and methods' to the results associated, this is thought to facilitate the reader. In case of any cross-over of usage of materials and/or the methodologies, the relevant section is referred to where it appears first in this thesis.

Chapter 1 introduces the reader to the wider context and motivation of the work presented herewith in the field of MFCs. Chapter 2 then goes on to assessing and reviewing the current state of the relevant literature from which the study is derived in attempt of making contribution to the current state-of-the-art of MFC technology and its knowledge.

Chapter 3 presents the study on improving the start-up time and biocatalytic activity. Chapter 4 presents the study on piecewise linearization of MFC process using the system identification approach, for its utility in control. Chapter 5 is on the investigation on electrical connectivity in order to circumvent the voltage reversal in MFC during its stack operation. Chapter 6 seeks to optimise the anode geometry for the improvement in the MFC performance utilising the finite element method modeling approach for the fluid flow and mass transport and Chapter 7 investigates into the up-scaling of the tubular MFC, lengthwise without compromising the power production.

Chapter 8 discusses the study presented in Chapter 3 – Chapter 7 in a wider context. Chapter 9 presents the conclusions drawn and the future prospects of the presented work. Chapter 11 provides supporting information for Chapter 3 and Chapter 12 provides the list of peer-reviewed journal publications and, oral and poster presentations at conferences; derived from this study.

2. Literature Review

Microbial Fuel Cells (MFCs) are Bioelectrochemical system (BES) which utilise electrogenic bacteria as a catalyst to oxidise organic and/or inorganic substrates anaerobically to produce electricity (Logan et al., 2006, Potter, 1911). This novel bacterial phenomenon was first discovered by Potter (1911) in the early 20s and showed that glucose degradation by yeast in an anaerobic environment produced an electromotive force (emf) of 0.32 V in a cell which included the oxidation of glucose in anodic chamber and platinum as counter electrode. The 'bio-fuel cell', as it was known then, was recognised by the symposium on bioelectrochemistry of microorganisms (Lewis, 1966), as low power devices useful for niche applications but it was not until Allen and Bennetto (1993) who realised its application into treatment of wastes. According to Pant et al. (2010), this phenomenon was not explored until recently, showing that biological fuel cells gained interest in recent years by looking at the number of research articles published, saw a 60-fold increase in publications over the decade 1998-2008. Many MFC designs, developments and optimisations that focus on improving the performance and hence applicability in real-world processes have since been carried out and are continuing. In particular, the improvements in their performance through engineering principles are of interest amongst all the others as the final application of MFCs for example, in treatment of wastewaters would require scaling-up and addressing the engineering challenges and during their implementation.

2.1 MFC fundamentals

From thermodynamic point of view, microorganisms (electrogens) in the MFC gain energy by donating electrons that are generated in their metabolism, to the electrode (anode) as per the Gibbs free energy under standard conditions (298.15 K temperature, 1 bar pressure and 1 M concentration for all chemical species) and can be derived as (Logan et al., 2006, Rabaey, 2009):

$$E_{emf} = E^0_{emf} - \frac{RT}{nF}\ln(\pi) \qquad \textit{Eq. 2.1}$$

Where;

E_{emf} is cell electromotive force, emf (in volts),

E^0_{emf} is the standard cell emf (in volts),

R is universal gas constant (8.314 J mol^{-1} K^{-1}),

T is the temperature (in K),

n is the number of electrons,

F is the Faraday constant (96.485 × 10^4 C mol^{-1}) and

π is the reaction quotient.

Eq. 2.1 is known as Nernst equation and it is useful in calculating theoretical emf generated by the half-cells.

The cell emf, E_{cell} (in volts) can be calculated by (Logan et al., 2006),

$$E_{cell} = E_{cathode} - E_{anode} \qquad \textit{Eq. 2.2}$$

Inferred from equation 2.1 and 2.2, as detailed by Logan et al. (2006), the theoretical cell emf (between anode and cathode) of MFC running on acetate at its anode and oxygen reducing cathodes, is 1.101 V under standard conditions. Here, $E_{cathode}$ and E_{anode} are potentials of cathode and anode half-cells, respectively, in the MFC.

The MFC voltage can also be represented by the following equation (Larminie et al., 2003, Schröder and Harnisch, 2009),

$$E = E_{cell} - |\sum \eta_{an}| - |\sum \eta_{cat}| - IR_{\Omega} - j_{an}r_{an} - j_{cat}r_{cat} \qquad \textit{Eq. 2.3}$$

Here, E is cell or more precisely, MFC potential (or voltage),

E_{cell} is the theoretical cell emf of MFC,

$|\sum \eta_{an}|$ is overpotential occurring at the anode,

$|\sum \eta_{cat}|$ is overpotential occurring at the cathode,

IR_{Ω} is the losses related to internal resistance of the MFC,

$j_{an}r_{an}$ is losses due to internal currents at the anode and

$j_{cat}r_{cat}$ is losses due to internal currents at the cathode.

Overpotentials at the electrodes (anode and cathode) include activation losses and concentration (or mass transfer) losses (Logan et al., 2006, Schröder and Harnisch, 2009). Typically, overpotential is defined as the difference between the thermodynamic reduction

potential (theoretical) and the experimentally determined reduction potential of a particular electrochemical reaction. In the case of anode in MFC, bacterial metabolic losses may also occur (Logan et al., 2006, Schröder and Harnisch, 2009). Activation losses, shown in Figure 2.1, occur due to the activation energy required by the oxidation/reduction reactions at the electrodes, ohmic losses occur due to the resistance of electrode materials through which electrons must travel and resistance of electrolyte through which the ions must pass during the oxidation/reduction reactions and; concentration losses occur at high current densities where the mass transfer is limited compared to the electrical current demand, the rate of substrate conversion by biocatalyst, rate of electron transport from electrogens to the anode and rate of proton transport through the membrane as well as out of the biofilm is limited. Higher bacterial metabolism losses occur in the anodes of MFCs when the potential difference between the anode and the bacteria (electrogens) is higher (Logan et al., 2006, Schröder and Harnisch, 2009).

Figure 2.1 shows a typical polarisation curve (voltage, *E* vs. current, *I*, in red) resulting from the MFC when an external electrical load connected to the MFC is varied/swept from highest to the lowest while measuring the voltage (Logan et al., 2006). The power curve (power, *P,* in green) is obtained when the voltage from polarisation is multiplied to the corresponding value of current. The power can also be represented against voltage or the load axes. The polarisation and power curves are essential tools that can determine the performance of MFCs and able to compare among them by normalising power (sometimes

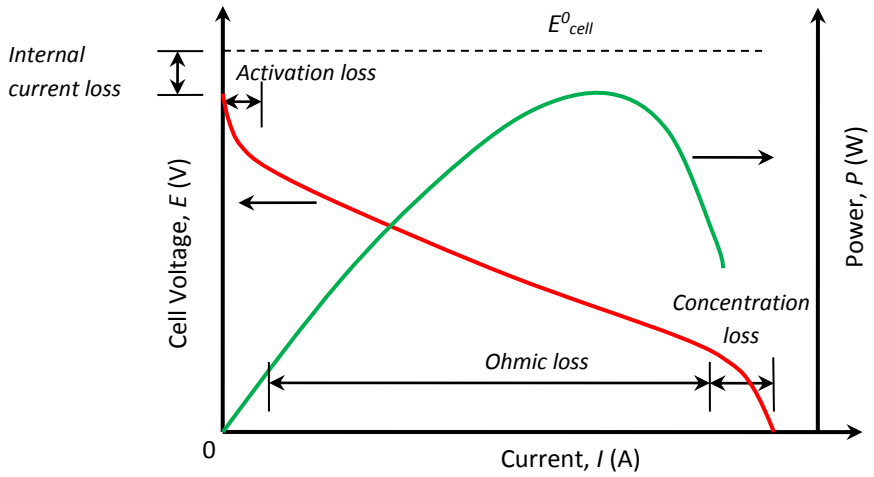

Figure 2.1: Typical polarisation (voltage in red) and power (in green) curves resulting from MFCs. The regions A, O, C and ICL show activation losses, ohmic losses, concentration losses and internal current losses, respectively.

also current) to the surface area (projected or actual) or the volumetric capacity (generally empty bed volume of the anode).

Schröder and Harnisch (2009) suggests that the activation overpotentials can be decreased by the usage of more effective catalysts (may also be applicable to the biocatalyst on anode), increasing the 'turn-over' rate of individual catalytic centre or increasing the number or active centre, i.e. loading of catalysts. Increase of reaction surface area on the electrode, operational temperature and higher concentration of substrate (for example, by increasing the oxygen pressure for the cathode (Fornero et al., 2008)) can also help in decreasing the activation potential. The increase in pressure however, can reflect the operational cost in running the MFC. So, increase in the available surface area (at anode and cathode) for the catalyst/biocatalyst and the increase in the amount of biocatalyst and or the activity seems achievable and could be cost-effective in increasing the performance of the MFC.

Ohmic losses could be decreased by decreasing the internal resistance of the MFC by means of using high conductivity electrolyte, low electrical resistant electrode/membrane materials, reducing the electrode spacing and minimising contact resistances. Again, increasing ionic strength to increase the solution conductivity to some extent may be acceptable but may pose operational cost and it would be desired to minimise the ohmic losses through use of highly conductive materials and effective MFC design (Logan et al., 2006, Schröder and Harnisch, 2009).

Concentration losses could be lowered by using reactor mixing for enhancement of the mass transport but such uses may increase the required input energy and increase of buffering capacity to compensate the pH gradients which can increase the operational costs through the use of chemicals (Schröder and Harnisch, 2009).

Internal current losses (as shown in Figure 2.1), occurs in the substrate cross-over situation where the substrate from the anode compartment could permeate through the membrane to the cathode and similarly, oxygen can diffuse through the membrane into the anode compartment. At the cathode, oxidation of organic substrate can take place, catalysed by Pt and using those electrons, the oxygen can be reduced at the same reaction site and thus, losing the substrate and the consequent potential through the loss of electrons even under open circuit conditions. This may be avoided by using less selective cathode catalyst such as laccases (Schröder and Harnisch, 2009, Schaetzle et al., 2009) but the life-time of such enzyme

based catalyst may be an issue for the scaled-up MFC systems. Likewise, aerobic oxidation (by the aerobes) in the anode compartment can increase the anode potential (decreasing the overall cell potential) (Schröder and Harnisch, 2009).

Also, pH splitting may occur between the anode and cathode of the MFC where metal ions instead of protons are transported from anode to cathode via the cation exchange membrane (CEM), resulting in acidification of anode and alkalization of cathode (Harnisch et al., 2008, Rozendal et al., 2006). This could be tackled by using the membrane-less MFC designs or by providing acidified anode effluent to the cathode to counterbalance the proton consumption during reduction reaction at cathode (Freguia et al., 2008). Membrane-less MFCs can contribute to the internal current loss and that would be undesirable.

2.2 The MFC start-up

The start-up of MFC process is accompanied by the colonisation of electrogens (whole cell bacteria) in their anodes and the process can be competitive due to the presence of other forms of anaerobes (such as methanogens) in the precursor inoculum from the anaerobic digester and/or preference of the electrogens for alternate metabolism to electron generation and therefore can be limited until the favourable conditions are met for the electrogens. Consequently, one of the factors which delay the peak performance is the time required for the formation of an active electrogenic biofilm at the anode electrodes, after the inoculation.

To accelerate the anodic biofilm (containing mainly electrogens) formation in BES, many approaches have been explored. The selection of inocula had an effect whereby Erable et al. (2009) showed that the MFC inoculated with the natural marine biofilm performed better than that of the sediment biofilms and; Kim et al. (2005) showed that using the biofilm scrapped from pre-enriched the acclimation time and the power performance of the MFC can be improved. Rabaey et al. (2004) showed that the enrichment process by successively transferring a bacterial consortium harvested from an active anode compartment increased the power production from 0.6 W m^{-2} to 4.31 W m^{-2}. The application of high shear fluid dynamics was also shown to have positive impact, in microbial electrolysis cells (MECs) (Ajayi et al., 2010) and MFCs (Michie et al., 2014, Oliveira et al., 2013, Pham et al., 2008). Borole et al. (2009) showed that the combination of variation in electrical load with the reduction in availability of substrate applied selective pressure for the electrogens to develop on the anode. The operating temperature (Michie et al., 2011, Min et al., 2008) and application of fixed or poised potential (Finkelstein et al., 2006, Wang et al., 2009) have also shown to influence the

acclimation of electrogens on the anode. Liu et al. (2008) showed that when an un-colonised (blank) electrode was immersed and poised with +0.2 V (vs. Ag/AgCl), in the same anode compartment containing a colonised (with electrogens) electrode, a new electrode respiring biofilm on the blank electrode, with twice the current density of the original (from 250 to 500 mA m^{-2}) was obtained. Wang et al. (2009) achieved shorter start-up time (40%, from 59 to 35 days) and higher current density of 600 mA m^{-2} as opposed to 84 mA m^{-2} by the application of positive poised-potentials to the anode of MFCs as opposed to the MFC operated under 1 kΩ constant load. These techniques have all suggested the possibilities of performance improvement at the biofilm formation stage.

The 'power overshoot' phenomenon has been frequently observed, regardless of the MFC configuration or operating conditions and it is widely accepted that it is caused by the biofilm on the anode (Winfield et al., 2011, Hong et al., 2011, Nien et al., 2011, Watson and Logan, 2011). Power overshoot is considered to be present in the MFC system when during the polarisation of the MFC, a sudden drop in the electrical current is observed while sweeping the MFC potential from one extreme to another (for example, from higher potential to the lower potential). Winfield et al. (2011) suggests that the occurrence of power overshoot as observed in power curves could be due to the immature biofilm and they observed the characteristic power curve overshoot after 5 days of MFC operation (since inoculation), which disappeared after 5 weeks of operation and it was concluded that the early development of the electrogenic biofilm could not sustain the higher current demand. The power overshoot can lead the MFCs to underperform in terms of chemical oxygen demand (COD) removal. Also, it was shown by Hong et al. (2011) that operating the MFC at higher current demand (in the region of power overshoot) the biofilm can form adaptation and the power overshoot disappears.

Considering the up-scaling of MFCs for their application in treatment of wastewaters, deployment of MFCs initiated with the application of poised-potential and high shear enrichment could be expensive and so can be the delayed start-up at lower temperature (Michie et al., 2011). Similarly, the scrapping of the biofilm and serial transfer of the electrogens to apply selection pressure could be time consuming and impractical for the up-scaled MFC system. Therefore, a cost-effective and automated rapid start-up of the MFC should be considered to achieve the peak power attainable by the MFC within its physical design constrains and the rapid enrichment and adaptation (maturation) of electrogenic biofilm with continual performance enhancement could support MFC/BES industrial adoption.

A maximum power point tracking (MPPT) has been proved to be beneficial in terms of posing a selective pressure on electrogens to perform better in terms of coulombic efficiency (Premier et al., 2011), which applies peak power point load in real-time. Therefore, with slight adaptation of the MPPT algorithm to pose high current loading right from the point of inoculation of the MFC and operating the MFC at its peak power may apply selective pressure on the electrogens over the methanogens that are normally found in the precursor inoculum, the activated anaerobic sludge, to adapt and perform better. Such controllers can be transferrable to the ultra-low power and low cost electronic devices such as micro-controllers. The use of such controllers with the control strategies can decrease the commissioning costs or the costs associated with the re-start of the MFC system after the necessary maintenance, should the need arise.

2.3 MFC system identification

MFCs are complex systems as the anodic biofilm and its interaction with the substrate and system components are; bio-, physico- and electrochemical processes and their coupled phenomena (Kato Marcus et al., 2007, Picioreanu et al., 2007, Pinto et al., 2010). They are affected by various operating conditions such as temperature, pH, OLR and electrical load (Jadhav and Ghangrekar, 2009, Michie et al., 2011, Zhang and Halme, 1995) and therefore, exhibit multiple dynamic processes. So, in order to maintain the optimised conditions, identification of the behaviour of the MFC output due to such input(s) is of great importance and consequently control the process. Given that the other operating conditions are optimum, the electrical load determines the maximum electrical power and the current drawn from the biofilm is affected by the applied load. The electrical load can allow the matching of impedances (internal and external) of the MFC and consequently the maximum power transfer and these electrical signals, intrinsic to BES due to electrogenesis, can readily be employed for the analysis of MFC systems.

As exemplified by the modeling of Picioreanu et al. (2007) and the discussions of impedance presented by Zhao et al. (2009a), the performance of MFC is expected to be nonlinear in nature. The variations in power and the MFC voltage with effected with variation in load indicates that the MFC cannot be represented by a single linear model. The anode of MFC can be considered vaguely similar to an anaerobic digester (AD) where the degradation of organic matter takes place by the electrogens in absence of oxygen. Those bioprocesses are known to be nonlinear in nature and complex (Emmanouilides and Petrou, 1997, Steyer et al., 1999). Control of the AD can be achieved by using nonlinear controllers such as the application

of neural network (Wilcox et al., 1995) and neural-fuzzy control system (Waewsak et al., 2010). However, in the context of MFCs, it would be desired and advantageous to seek simpler and cost-effective controller/control strategy in terms of its implementation, without increasing unnecessary complexity if not required.

Assuming that the performance of MFC over small perturbations (Khalil, 2002) can be reasonably represented by linear black box or process models, the system can be modeled and represented by series of linear models using piecewise linearisation methodologies. To represent the nonlinear dynamics, series of linear models can be scheduled according to the applied loads and the parameters of the models may be interpolated between the model instances. Also, recursive identification methodologies (Wang et al., 2011, Young, 2011) by using system identification approach can track changes in the model parameters should they change due to the time variation of the system caused by for example, biofilm evolution or adaptation, the substrate feed, temperature, pH, solution conductivities and so forth bearing that the order and structure of the model are not affected unpredictably with time. Modeling of the system by identification process has been applied to AD and various other physical and chemical processes such as in Ref. (Gustavsson, 1975, Kristinsson and Dumont, 1992, Premier et al., 1999, Tan et al., 1995) as well as conventional fuel cells such as solid oxide fuel cells (SOFCs) (Jurado, 2004). However, this has not been explored yet for the MFCs/BESs and such models are aimed at developing the control strategies.

A current distribution model was developed by Di Lorenzo et al. (2010) in order to optimise the design of their MFC. The time domain transient response of the MFC voltage caused by step change in electrical load from very low (20 Ω) to very high (30 kΩ) was considered by Ha et al. (2010) to determine the charge transfer resistance and the double layer capacitance. Frequency domain characteristics were considered by Ramasamy et al. (2008), using equivalent electrical circuit model in order to determine the internal resistance of the MFC. Montebelli et al. (2010) presented a resistance-capacitance (RC) network model of MFCs and similarly, several impedance models have been determined using Electrochemical Impedance Spectroscopy (EIS) e.g. (Borole et al., 2010, Manohar et al., 2008, Zhao et al., 2009b). Borole et al. (2010) investigated the time variation in MFC performance using EIS models and electrochemical analysis of MFCs were elaborated by Zhao et al. (2009b). Time dependent dynamics were considered by Di Lorenzo et al. (2009a) in order to assess the response time by their biosensor. Also, linearised state-space models and their parameters were identified by Stein et al. (2012) to represent the behaviour of their MFC based biosensor

to detect toxic components in the water/wastewater. However, piecewise linearisation of the MFC by considering the cause (electrical load) – effect (MFC voltage) has not been studied yet over their whole operational loading range.

So, the dynamic cause and effect relationship that is present in the MFC system was studied as in aforementioned objective 2 introduced in Chapter 1 aiming to utilise the models for control of power/voltage/current from the MFC.

2.4 Avoiding voltage reversal in MFC stack

Operating the MFC with acetate as the substrate in its anode and oxygen as terminal electron accepter in cathode, the theoretical open circuit voltages of only 1.1 V can be achieved (Logan et al., 2006) at normal temperature and pressure (NTP), pH 7 and acetate concentration of 5 mM. The highest open circuit voltage is achieved in the laboratories *circa* 0.8 V and the working voltages of approximately 0.5 V (Oh et al., 2009).

For most practical applications such as powering electronics or charging batteries, the voltage generated by individual MFCs is insufficient, so they need to be stacked electrically in series to increase the voltage. Aelterman et al. (2006) demonstrated boost in the voltage by connecting 6 individual MFCs electrically in series and they were able to persistently extract power. However, towards the maximum power available from the MFCs, the voltages from some of the MFCs diverged and reversed. This phenomenon was also observed by several researchers in their MFCs (Dekker et al., 2009, Zhang and Angelidaki, 2012). Taniguchi et al. (2004) had observed voltage reversal in their proton exchange membrane (PEM) fuel cells which they attributed the cause of the voltage reversal to fuel starvation, including during the start-up; and it was confirmed by Oh and Logan (2007) that the deprivation of fuel could have the same effect in MFC systems. During the voltage reversal, the MFCs underperform and the power is lost within the stack in sustaining the voltage of the reversed cell(s) and therefore, it should be avoided. In the stack of MFCs, the MFCs should be operating at similar and sufficient substrate concentration, while fully functional anodes and cathodes, their electrical and ionic currents may be expected to be similar and so, the voltage reversal should not occur during their stack operation as demonstrated by Zhuang et al. (2012b). In the practical applications of MFCs such as wastewater treatment, the MFCs are likely to receive an imbalanced organic strength of substrate since the MFCs would tend to be connected hydraulically in series for the high volumetric throughput requirement and it is expected that the substrate will be progressively consumed as it passes through the MFC system (Kim et al., 2010, Zhuang et al., 2012b, Zhuang and Zhou, 2009).

Ieropoulos et al. (2010) demonstrated that the bank of capacitors can be connected electrically in series to harvest energy from the MFCs and perform useful task using the charge accumulated. Kim et al. (2011b) showed that the capacitors can be arranged in such a way that they can be charged by the MFCs in parallel and then discharged simultaneously in series across a load. This approach requires the relays which can consume substantial amount of power compared to the power produced (in mW range) by the MFCs. Also, due to the change in operational parameters of the MFC such as substrate concentration, temperature, buffer concentration, pH and flow rate (Greenman et al., 2011, He and Mansfeld, 2009, Manohar et al., 2008) for example, in wastewater treatment, the impedance of an MFC varies and the state of the system is often likely to be dynamic. The real-time impedance of MFC system could be matched and operated at as in Ref. (Premier et al., 2011, Woodward et al., 2009) and such controllers can be connected to the charging/discharging of capacitors by suitable means of current sourcing.

So, the possibilities need to be investigated which may utilise appropriate electrical connectivity and is capable of extracting peak power in real-time while avoiding the voltage reversal.

2.5 MFC designs and up-scaling

2.5.1 MFC architecture

Many laboratory scale MFC designs have emerged in pursuit of increasing power production. The dual chamber H-type MFC that is made of two glass bottles forming cathode and anode chambers and a tube connecting them with a membrane to separate catholyte and anolyte, is shown in Figure 2.2a. This configuration offers a valuable and well accepted research tool for studying parameters and/or materials in MFCs but is limited in its direct application as the power performance is very low (Logan et al., 2006). Flat-plate MFCs are designs that have planar electrode(s) arrangements (Logan et al., 2006, Cheng et al., 2005, Du et al., 2007, Min and Logan, 2004). Flat plate MFCs can be a single chamber MFC (as shown in Figure 2.2b) which utilises air as cathode and so, cathode electrode is exposed to the air; or dual chamber MFCs have anode, as well as cathode chambers that utilises liquid cathode such as ferricyanide or continuous aerated phosphate buffer solution (Mohan et al., 2001, You et al., 2006, Di Lorenzo et al., 2009c). Fan et al. (2007) have demonstrated that the flat-type MFC with j-cloth sandwiched between the anode and cathode electrodes can produce power density of up to 1010 W m^{-3} with coulombic efficiency of up to 71%. But, the anodic volume of

this MFC was 2.5 mL which seems impractical for its application into wastewater treatment processes. j-cloth and cathode (with Polytetrafluoroethylene, PTFE diffusion layers) assembly may have held the hydrostatic pressure generated from the anolyte in their MFC but increasing the scale of the reactor could be problematic as it may not hold the pressure generated by the liquid, static pressure head due to the height of the reactor and dynamic pressure due to the pumping.

Tubular MFC designs (as shown in Figure 2.2c) have concentric/annular electrode arrangements where the anode is inside a tube and cathode usually on the outside (Kim et al., 2010, Rabaey et al., 2005, Zuo et al., 2007, Zhuang et al., 2012a) but others have cathodes concentrically inside the tube containing the anode (Liu et al., 2004). Power production of up to 90 W m^{-3} has been seen from acetate consuming MFCs with granular graphite as the anode and potassium ferricyanide ($K_3Fe(CN)_6$) as the cathode (Rabaey et al., 2005). However, the use of ferricyanide is not sustainable due to the lack of regeneration capability once it is utilised

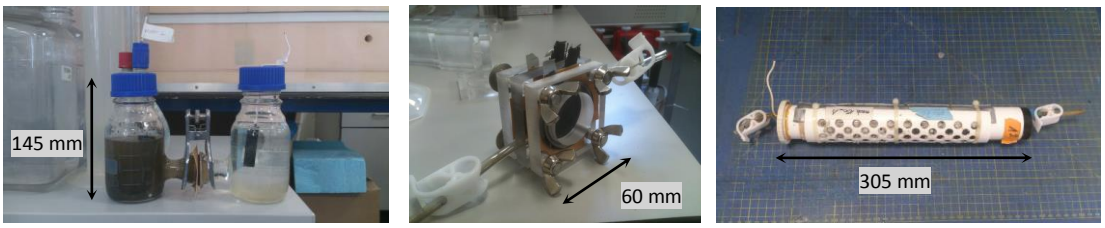

Figure 2.2: Various designs of MFCs. (a) H-type bottle MFCs, (b) Flat-type single-chamber MFC, (c) Tubular MFC with air-cathode.

and needs replenishing and it is not safe for its use in the wastewater treatment application (Rinaldi et al., 2008). Also, issues of clog-up in anode chamber due to biomass and mass transport may arise when fluid paths are narrower e.g. with a granular graphite matrix (Aelterman et al., 2008, Di Lorenzo et al., 2010). Increasing power densities from 6.1 W m^{-3} to 60.5 W m^{-3} have been reported using MFC designs suggested to be scalable (Kim et al., 2012, Kim et al., 2009), but in the latter case, power density was determined using a potentiodynamic method, which may generate higher power estimates than the potentiostatic method. Nevertheless, these systems could achieve higher power densities as exemplified by Michie et al. (2014) who was able to generate 11.63 W m^{-3} with their MFCs with anodic volumes of 147 mL. These could be up-scaled by replication for application in real wastewater treatment processes (Kim et al., 2011a). Table 2.1 compares a few commonly investigated reactor designs, materials, key operational parameters and their performances.

Table 2.1: Comparison of power production from various designs of MFCs found in literature

MFC type	anode capacity (mL)	Cathode	Anode	Feed	Buffer	Temperature (°C)	Membrane	Maximum power density (W m^{-3}) [power, in mW]	Reference
Dual* chamber MFC	1.2	50 mM $K_3Fe(CN)_6$ in 100 mM phosphate buffer (graphite felt)	Graphite felt	Sodium lactate (0.6 - 20 mL min^{-1})	Growth medium for Shewanella oneidensis DSP10	25	PEM, Nafion 117	500 [0.6 mW]	(Ringeisen et al., 2006)
Flat type	2.5	Air (0.5 mg cm^{-2} Pt on 30% wet proof carbon cloth)	Plain non-wet proof carbon cloth	20 - 30 mM acetate (0.6 mL min^{-1})	50 mM Phosphate buffer	30	Membraneless, j-cloth electrode assembly	1010 [2.525 mW]	(Fan et al., 2007)
Tubular	210	50 mM $K_3Fe(CN)_6$ in 100 mM phosphate buffer (Graphite mat)	Graphite granules	Acetate (1.1 kg COD m^{-3} d^{-1})	50 mM Phosphate buffer	-	CEM	90 [18.9 mW]	(Rabaey et al., 2005)
Flat type	12	Air-cathode (0.5 mg cm^{-2} Pt on carbon cloth)	Ammonia treated plain non-wet proof carbon cloth	1 g L^{-1} sodium acetate (Batch fed)	200 mM Phosphate buffer	30	Membraneless	115 [1.379 mW]	(Cheng and Logan, 2007)
Flat type	16.11	Air-cathode (40% cobalt tetramethylphenylporphyrin (CoTMPP, 1.2 mg cm^{-2}) on 30% wet proof carbon cloth)	Ammonia gas treated graphite fibre brush anode	1 g L^{-1} glucose	50 or 200 mM phosphate buffer	23 ± 3	Membraneless	73 [1.176 mW]	(Logan et al., 2007)
Tubular	200	Air-cathode (0.5 mg cm^{-2} Pt on carbon cloth)	Monolith activated	40 mM acetate (Batch fed)	50 mM Phosphate buffer	26 ± 2	CEM	6.1 [1.22 mW]	(Kim et al., 2009)

* Pure culture of Shewanella oneidensis DSP10 was used in the anode

MFC type	anode capacity (mL)	Cathode	Anode	Feed	Buffer	Temperature (°C)	Membrane	Maximum power density (W m^{-3}) [power, in mW]	Reference
			carbon						
Tubular	10000	Air-cathode (Ni based conductive paste with MnO_2 catalyst)	Graphite felt	Brewery wastewater (1.06 g COD L^{-3} d^{-1})	-	30 ± 1	Air-permeable layer and a GORE-TEX® cloth	4.1 [41 mW]	(Zhuang et al., 2012a)
Single chamber	12.5	Air-cathode (0.3 mg cm^{-2} Pt on carbon cloth)	Graphite pellets	1 g L^{-1} glucose (Batch fed)	50 mM Phosphate buffer	21 ± 2	CEM	8.1 [1.013 mW]	(Di Lorenzo et al., 2010)
Tubular	147	Air-cathode (0.5 mg cm^{-2} Pt on carbon cloth)	Carbon veil	40 mM sodium acetate (270 mL min^{-1})	50 mM Phosphate buffer	-	CEM	11.63 [1.7 mW]	(Michie et al., 2014)
Tubular	0.075	50mM $K_3Fe(CN)_6$	Carbonised bamboo charcoal	0.68 g L^{-1} sodium acetate (Batch fed)	8.3 mM phosphate buffer	30 ± 1	CEM	3303 [2.48 mW]	(Li et al., 2014)

It can be seen from Table 2.1 that the net power produced from the MFCs that are researched widely is only in the magnitude of a few milliwatts. Higher power density is apparent from the smaller volume of the anode chamber which contains the anolyte. For practical purposes, such as in wastewater treatment, anodic capacity (volume) would need to be increased to be able to treat such a large quantities of wastewater such as demonstrated by researchers in Ref. (Kim et al., 2009, Michie et al., 2014, Zhuang et al., 2012a). This has a consequence of decrease in available surface area compared to the volume and therefore, the net power generated decreases due to less biocatalyst (Michie et al., 2014) or aforementioned mass transport issues if granules or porous carbon is used (Di Lorenzo et al., 2010, Kim et al., 2012). Li et al. (2014) showed enormous power density of 3303 W m^{-3} from their carbonised bamboo charcoal anode based on the inside volume of the bamboo charcoal only and did not account for the net anodic volume in which it was present. Given that it produces the power of 2.48 mW from a charcoal that is 2 mm in diameter and 24 mm long, it can be comparable to the anode materials that have been used in single chamber MFC of the similar size (Cheng and Logan, 2007, Di Lorenzo et al., 2010, Logan et al., 2007).

Derivative of carbon materials are generally used as anode (also as cathode) material as they are versatile, chemically stable and can offer a good electrical conductivity as well as provides a bio-compatible surface for the electrogenic bacterial attachment (Logan et al., 2006, Wei et al., 2011). Several different carbon materials, textures and configurations have been used as anode electrodes; such as carbon paper, carbon cloth, electrospun carbon, granular carbon, carbon veil, monolithic carbon, reticulated vitreous carbon (RVC), grapheme, carbon nanotubes, etc. (Chen et al., 2011, He et al., 2005, Kim et al., 2012, Kim et al., 2010, Logan et al., 2006, Rabaey et al., 2005, Di Lorenzo et al., 2010, Di Lorenzo et al., 2014, Mink et al., 2012, Yong et al., 2012). However, various biocompatible metals have also been used such as Au decorated, iron-oxide coated, Pd-decorated and Pt-coated titanium to enhance the power performance of the MFC (Lowy et al., 2006, ter Heijne et al., 2008, Kim et al., 2005, Fan et al., 2011).

Cathode and anode are usually separated by ion exchange membranes (Logan et al., 2006, Oh et al., 2010, Pant et al., 2010) but use of j-cloth have also been found to provide physical separation between them (Fan et al., 2007). Having no membrane (membraneless) that separates cathode to the anode, can result in lower internal resistance due to removal of the membrane and consequently improve the power performance of the system (Cheng and

Logan, 2007, Logan et al., 2007). However, this can result into internal current losses as discussed in section 2.1 and lower the coulombic efficiency.

2.5.2 Optimisation of MFCs and up-scaling

There are several factors that can affect the MFC performance as discussed in section 2.1 and the mass transport and overpotential limitations can be identified as the most important issues that would need to be addressed for up-scaling of the MFC (Logan et al., 2006, Oh et al., 2010). Anode surface area to volume ratio defines the amount of biocatalyst (electrogenic bacteria) that anode can have on its surface for the given volume and so, when the available area is increased, the power density also increases due to increase in the electrical current. Use of carbon brush, granular graphite and porous carbon is seen to have improved the systems (He et al., 2005, Kim et al., 2012, Logan et al., 2007, Di Lorenzo et al., 2010). But, if these designs have narrow fluidic channels like in Ref. (He et al., 2005, Logan et al., 2007), clogging up issues are likely to arise along with the mass transport issues that were identified by Di Lorenzo et al. (2010) and the comparison between granular and graphite disc electrode by Di Lorenzo et al. (2009c) evidenced that the MFC operated with granular anode electrode produced the power 3 times lower than that of the MFC employing graphite disc and so, use of the granular electrode or similarly arranged carbon brush anodes may not generate high power when the MFC system is up-scaled.

Helical anode designs have been proven to have produced more power compared to the annular electrodes since they offer higher projected surface area compared to the annular electrode designs, provide high shear to the biofilm surface and offer better mass transport evidenced by the studies in Ref. (Kim et al., 2012, Kim et al., 2009, Michie et al., 2014). Di Lorenzo et al. (2010) showed that their model of current distribution in packed bed electrode was able to inform the design parameters of their MFC and so have Kim et al. (2012), Michie et al. (2014) and Kim et al. (2014) by using computational fluid dynamics approach to better understand the mass transport in the anode and improve the system further.

So, if the physics of mass transport were coupled to the fluid flow, it would better inform the design in terms of improvement in the parameters or system elements and therefore, further improve the performance.

Also, when up-scaling the MFCs is considered by modularisation, loss in power performance along its forward length (feed direction) is known to be a major issue (Kim et al., 2011a, Zhuang et al., 2012a, Zhuang et al., 2012b, Zhuang and Zhou, 2009) where the cross-

conduction and parasitic currents have been proposed causes (Zhuang and Zhou, 2009, Schröder and Harnisch, 2009) for lower power performance, which can also lead to voltage reversal if stacked electrically in series (Dekker et al., 2009). Optimisation of MFC (here anode is considered) for the better mass transport and lower internal resistance can improve the stack (hydraulically) performance when scaled-up. So, this study (objectives 4 and 5 in Chapter 1) aims to improve the MFC performance by improving the anode design for the improved mass transport by using finite element method modeling approach and demonstrate the scalability by up-scaling using the improved MFC reactors.

In considering the application of MFC systems in the treatment of wastewaters, it is evident that cost-effective and rapid start-up needs to be achieved. Control of the MFC output would require an understanding of the system dynamics, achieved through modeling typically, but models useful to control are often less concerned with fundamental processes and frequently more concerned with function (i.e. cause and effect relationships). The MFC stack performance needs to be improved, from that typically achieved and addressed through the control. The concomitant advantage of avoiding the adverse effect of voltage reversal also required attention. The power performance improvements through the optimisation of system element design (here the anode) would also need to be considered. Furthermore, the up-scaling of the MFC needs to be achieved without compromising the power performance.

3. On improving initiation and the performance of MFCs

3.1 Introduction

Since MFCs are biologically catalysed systems, they rely on physical attachment between electrogenic bacteria and the electrode (in particular anode although MFCs can consists of biological cathode which is not considered in this study) and/or other electron transfer mechanisms such as electrochemical mediators. Typically, the electron transfer is facilitated by an electrogenic biofilm on the anode electrode, but may also be carried out through the mediated electron transfer from electrogenic bacteria in suspension form in the liquid media.

The enrichment of the anode, i.e. electrogen adhesion on the anode or dominance in the planktonic form can be influenced by providing favourable conditions to the MFC such as temperature, pH, growth medium, anaerobic environment and an electron sink. Wang et al. (2009) have shown that poising the anode at +200 mV vs. Ag/AgCl (Saturated KCl) can accelerate the MFC start-up process and achieve its full potential for power generation in relatively short period of time (35 days vs. 59 days) compared to the MFC that was loaded with a constant electrical load of 1 kΩ. Studies by Woodward et al. (2009) and Premier et al. (2011) showed the possibilities of maintaining the optimum load on MFC by using the maximum power point tracking (MPPT) strategies and clearly showed that the performance of electrogenic anodic biofilm could be enhanced by applying such selective pressure (Premier et al., 2011). This chapter presents a study of control to improve the start-up time and increasing the bioelectrochemical activity of electrogens by the use of such MPPT strategies, which could outperform the statically electrically loaded MFCs. This could be useful when deploying the large arrays of scaled-up MFCs which are expected to have large time delays in the start-up than the lab scale MFCs and therefore may benefit from such an automatic faster start-up.

3.2 Materials and methods

3.2.1 MFC set-up and inoculation

Three identical H-type MFCs were constructed using the 250 mL bottles connected by a tube (Cambridge Glassblowing Ltd., UK) as shown in Figure 3.1. An anode was constructed from carbon electrode (TGPH – 120 Toray carbon paper, E-Tek, NJ, USA) with size 2.5 cm × 4.5 cm and cathode of the same size from carbon electrode containing Pt catalyst (0.35 mg cm^{-2};

10% Pt; E-Tek, NJ). The thickness of anode and cathode electrodes were 0.4 mm. Copper wires (1/0.8 HR WHITE 100M, pro-POWER, Farnell, Leeds, UK) were clamped on to the electrodes and an adhesive (Araldite® Rapid, Go-Araldite®, Switzerland) was applied to the bare wires and connections to protect the connections and avoid corrosion of copper under water. The two chambers (anode and cathode) were separated by cation exchange membrane, CEM (CMI-7000, Membrane International Inc., NJ, USA).

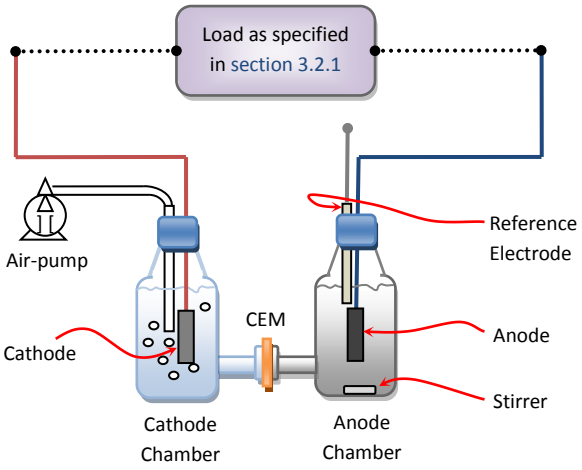

Figure 3.1: H-type MFC set-up with loading as specified in section 3.2.1 for MFC-PP-MPPT, MFC-MPPT and MFC-*Control*.

An inoculum containing sludge (Cog Moors Wastewater treatment plant, Cardiff, UK) and media with ratio of 1:10 was used to inoculate anode chambers. The media contained 40 mM sodium acetate in 50 mM phosphate buffer, nutrients and traces of minerals as shown in Table 3.1 (Kim et al., 2009). The anode chambers were inoculated in aerobic condition (i.e. not in an anaerobic glove box). Cathode chambers were filled with 50 mM buffer and were continuously aerated by a pump (AP-180, TRIXIE Heimtierbedarf GmbH & Co. KG, Germany) to provide oxygen as the terminal electron accepter. Phosphate buffer was used to maintain pH 7 in the anode chamber.

Table 3.1: Ingredients of 50 mM phosphate buffer, nutrients and minerals

Contents	Concentration (g L^{-1})
Buffer	
NH_4Cl	0.31
$NaH_2PO_4 \cdot H_2O$	2.69
Na_2HPO_4	4.33

Contents	Concentration (g L^{-1})
KCl	0.13
Vitamins/Nutrients	
Biotin	0.002
Folic acid	0.002
Pyridoxine HCl	0.010
Riboflavin	0.005
Thiamin	0.005
Nicotinic acid	0.005
Pantothenic acid	0.005
B-12	0.0001
4-aminobenzoic acid	0.005
Lipoic acid	0.005
Minerals	
Nitrilotriacetic acid	1.5
$MgSO_4 \cdot 7H_2O$	6.2
$MnSO_4 \cdot H_2O$	0.5
NaCl	1.0
$FeSO_4 \cdot 7H_2O$	0.1
$CaCl_2 \cdot 2H_2O$	0.1
$CoCl_2 \cdot 6H_2O$	0.1
$ZnCl_2$	0.13
$CuSO_4 \cdot 5H_2O$	0.01
$AlCl_3 \cdot 6H_2O$	0.0052
H_3BO_3	0.01
$Na_2MoO_4 \cdot 2H_2O$	0.0261
$NiCl_2 \cdot 6H_2O$	0.024
$Na_2WO_4 \cdot 2H_2O$	0.025

Three different start-up strategies were applied to the H-type MFCs; (a) MFC-PP-MPPT, load was applied using an MPPT algorithm preceded by poised-potential; (b) MFC-MPPT, load was applied using an MPPT algorithm alone; and (c) MFC-*Control*, a constant electrical load of 1 kΩ was applied to act as a *Control* against MFC-PP-MPPT and MFC-MPPT. The MPPT and PP-MPPT algorithms are described below, in section 3.2.2.

After the start-up of MFCs, voltage from MFC-MPPT was observed to have dropped and therefore, 40 mM sodium acetate was injected into the anode of MFC-MPPT on day 25. Likewise on day 29, 50 mM, 34.3 mM and 34.3 mM Sodium acetate were injected into the anode chambers of MFC-*Control*, MFC-MPPT and MFC-PP-MPPT, respectively. When the power generation from each MFCs appeared to stabilise, the anolyte was completely discarded, the anode chamber was scrubbed, washed (to remove any biomass on the glassware) and content replenished with fresh media containing 10 mM of sodium acetate (in 50 mM buffer, nutrients and minerals). The procedure was constructed in an anaerobic environment within a glove box (Vinyl Anaerobic Airlock Chamber, Coy Scientific Products, MI, USA). Also, the anodes were gently rinsed with distilled water to remove any loosely attached biomass, extracellular materials and sludge particulates from the electrode and to retain only the well attached biofilm on the electrode. Any further replacement of media (since the MFCs were run in the fed batch mode) was carried out in the glove box to maintain the anaerobic environment in the anode. All MFCs were operated in a heated chamber at 30 ± 2 °C temperature. The anode chambers were stirred continuously using magnetic stirrer (OxITop® IS 6-Var, WTW, Xylem Analytics UK Ltd., UK).

3.2.2 Start-up strategies

The H-type MFCs were operated under different control regimes implemented through virtual instrumentation as follows.

MFC-MPPT and MFC-PP-MPPT reactors were electrically loaded with the MPPT loads independently (across the anodes and cathodes as in Figure 3.1) but preceded by the application of a poised-potential on MFC-PP-MPPT. MFC-*Control* was loaded with a constant electrical load of 1 kΩ across the anode and cathode. The electrical load of 1 kΩ on MFC-*Control* was selected based on the internal ohmic load impedance occurring at peak power for a similarly operated MFC at stable enriched condition. However, the load was then reduced to 500 Ω on the basis of the power curve measurements after the start-up, on day 41.

The MPPT algorithm was based on a hill-climbing algorithm (as shown in Figure 3.2) to track peak power in real-time and was encoded as follows:

For the given MFC, the slope of its power curve (power (P) against current (i)) is given by,

$$SPi = sign(\partial P/\partial i) \qquad \text{Eq. 3.1}$$

and the rate of change of slope is given by

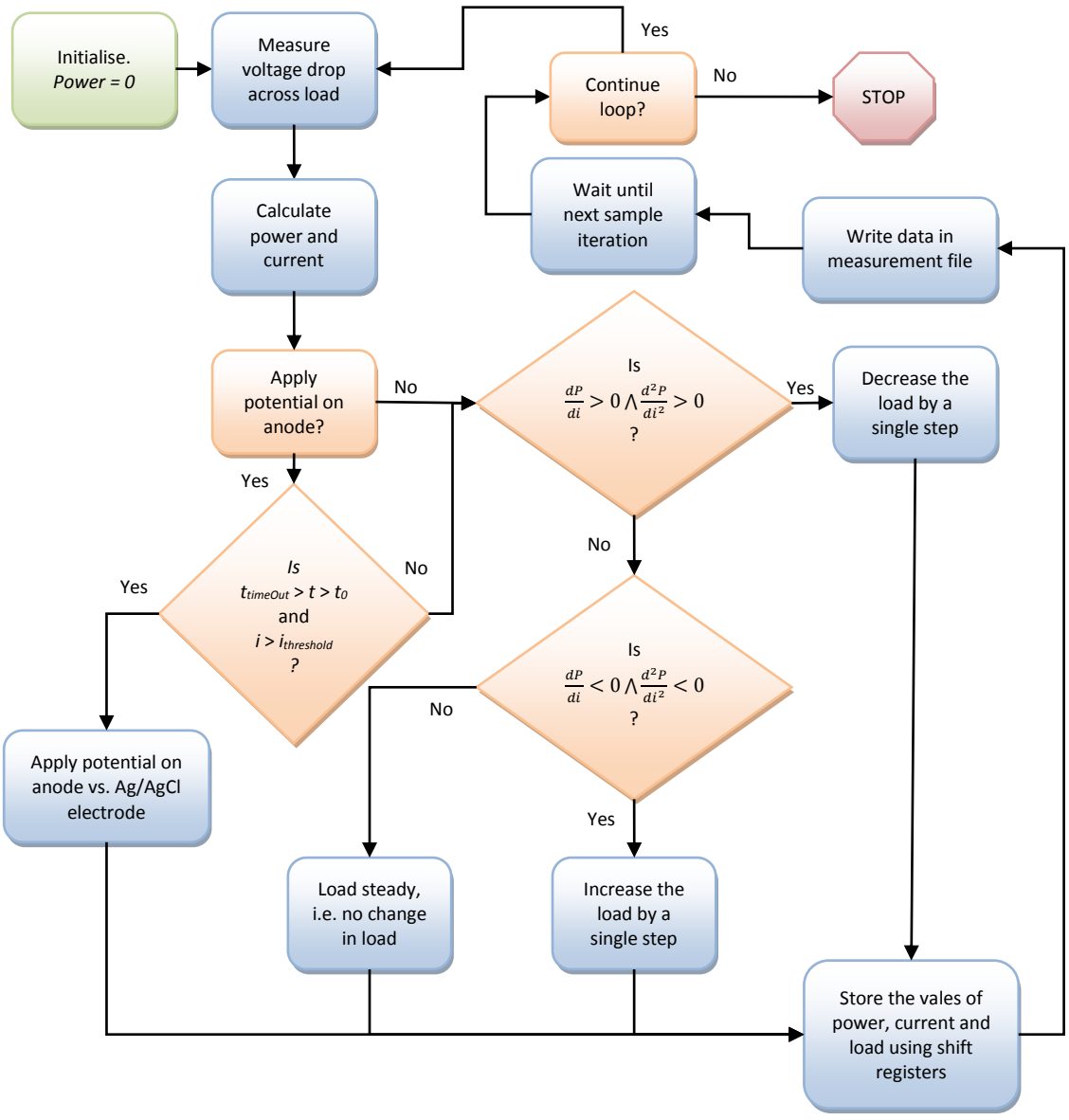

Figure 3.2: Flow chart showing a typical routine (algorithm) for application of poised-potential on anode (only on MFC-PP-MPPT) along with the maximum power point tracking (MPPT) on H-type MFCs.

$$dSPi = sign(\partial^2 P/\partial i^2) \qquad \text{Eq. 3.2}$$

By normal convention, the slopes (*SPi*) can be considered positive (S_p) and negative (S_n) when *Spi > 0* and *Spi < 0*, respectively. Likewise, the rate of change of slope (*dSPi*) can be considered positive (dS_p) or negative (dS_n) when *dSpi > 0 and dSpi < 0*, respectively. $\partial p/\partial i$ and $\partial^2 p/\partial i^2$ were estimated using Euler's method from sampled data. The ohmic load was increased (*Inc*), decreased (*Dec*) or unaltered and steady (*Con*) as per the decisions provided by Boolean logic formulated as below:

$$Inc = (S_n) \wedge (dS_n) \qquad \text{Eq. 3.3}$$

$$Dec = (S_p) \wedge (dS_p) \qquad \textit{Eq. 3.4}$$

$$Con = \overline{Inc} \wedge \overline{Dec} \qquad \textit{Eq. 3.5}$$

A digital potentiometer MAX5450 (MAXIM, Reading, UK) was used as variable load (MPPT load) to represent a mechanism which would control the sourcing of current from the MFCs. The apparent electrical resistance of the MAX5450 was controlled digitally by applying specific bit patterns to the device. The control signal to MPPT load as per the decisions from Boolean logic (Eq. 3.3 – 3.5) was provided by a personal computer equipped with NI USB-6009 and LabVIEW™ (National Instruments™, Newbury, UK) to actuate the MPPT load. Three MAX5450 were connected in parallel to give a range of 160 Ω – 3.3 kΩ and step size of ±12 Ω for each MPPT loads on MFC-MPPT and MFC-PP-MPPT.

Poised-potential on the anode of MFC-PP-MPPT was applied according to the following formulation:

Immediately after inoculation; at t_0, if $i < i_{threshold}$ then, $V_{sys} = E_{poised}$; and at $t > t_0$, if $I > i_{threshold}$ *or* $t > t_{timeOut}$, then employ MPPT algorithm as above (also in Figure 3.2). Here, t_0 is the initial time, when MFC is inoculated, i is sampled value of current delivered by the MFC; $i_{threshold}$ is a threshold current, above which the MFC is thought to have established electrical current generation (from biofilm), V_{sys} is the potential across the MFC; E_{poised} is poised-potential applied to the anode against a reference electrode (Ag/AgCl, Saturated KCl, +0.210V vs. NHE, BASi, UK), t is time and $t_{timeOut}$ is time after which application of poised-potential will time-out and terminate. Here, $i_{threshold}$ of 0.1 mA was selected using *a priori* knowledge from a similar system and time-out ($t_{timeOut}$) was defined to be 24 hours. E_{poised} = +0.645 V (vs. Ag/AgCl, Saturated KCl, BASi, IN, USA) was selected to emulate a cathode potential based on $E_{cell} = E_{cathode} - E_{anode}$ where E_{cell} is considered to be a theoretical maximum potential for MFCs (at STP), 1.1 V (Logan et al., 2006), and E_{anode} is taken to represent a biofilm operating in an MFC, which is expected to tend toward -0.455 V (vs. Ag/AgCl, Saturated KCl, BASi) in an acetate fed MFCs (Cheng et al., 2008). Initially, there was a delay of two sample (1 minute) observed in running the subroutine during execution of the MFC-PP-MPPT algorithm. To remove the delay, the decision making algorithm for application of poised-potential was removed on day 48, as it was no longer needed when tracking the peak power.

3.2.3 Electrochemical Analyses

3.2.3.1 Electrical power measurements

The power performance of each MFCs was measured by connecting to a variable electrical load, *R* (Resistance Decade Box, TENMA, Japan; 1% tolerance) and varying the load from highest to the lowest in a stepwise manner with load values of 5000, 3000, 1500, 1000, 800, 500, 300, 200, 150, 100 and 50 Ω. Voltage drop (*V*) across the load was measured (after 15 – 40 minutes of step change depending on the value of electrical load and associated settling time) and; power (*P*) and current (*I*) was calculated using V^2/R and V/R, respectively.

Power from MFC-PP-MPPT and MFC-MPPT was measured on day 23, 39 and 46 and from MFC-*Control* on day 42, 49 and 56 after the inoculation and during the biofilm development. Once stable power generation had been established, 'spent' inoculum from the anodes of MFC-PP-MPPT and MFC-MPPT was discarded on day 47 and from anode of MFC-*Control* on day 57; and replaced with the fresh anode media as stated in section 3.2.1. Power performance was measured on day 65 and 180 for MFC-PP-MPPT and MFC-MPPT and; day 85 and 180 for MFC-*Control*. Fresh anode media was provided at least 1 day prior to each power performance measurements (except in the case of inoculation, before discarding the inoculum).

During the power performance measurements and continuous monitoring, the voltage drop across the loads connected to the MFCs were measured and recorded using a personal computer equipped with LabVIEW™ and NI USB-6009 (National Instruments™) at 30 s sampling intervals.

3.2.3.2 Cyclic voltammetry

Once the biofilm was believed to have been established on day 65 for MFC-PP-MPPT and MFC-MPPT and on day 85 for MFC-*Control*, cyclic voltammetry was performed on each anodes using standard procedure as described by Logan et al. (2006). A three electrode system, with anode as working electrode, cathode as counter electrode and Ag/AgCl (Saturated KCl, BASi) electrode as reference electrode (as shown in Figure 3.1) was used and the anode potential was ramped from -0.8 V to +0.8 V and back to -0.8 V vs. Ag/AgCl (Saturated KCl, BASi) at a rate of 10 mV s^{-1}, while measuring the electrical current via Solartron 1287A (AMETEK® Inc., Cambridge, UK). The CVs were measured after the power curve measurements on the days mentioned above, with three continuous cycles of CV, out of which the last of the three CV cycles was taken as the final result.

3.3 Results and discussion

3.3.1 Start-up of MFCs under different electrical loading

Figure 3.3 shows Voltage generated from the MFCs during the first 15 days after inoculation. The data shown in Figure 3.3 and Figure 3.4 were re-sampled off-line at 1 hour intervals to decrease the density of the data for clarity of presentation, without loss of generality. As is evident from Figure 3.3, all MFCs were electrically loaded by a 1 kΩ, resistive load initially. Within the first 24 hours, on 8 occasions, an increase in current was observed when the PP-MPPT algorithm on MFC-PP-MPPT was applied (voltage variations are not obvious in Figure 3.3, however electrical load variations are evident in the first 24 hours). It appears that on ten occasions the threshold current ($i_{threshold}$) condition was satisfied by fluctuations in the current signal, with the consequence that, the PP-MPPT algorithm applied the MPPT load. However, this was short-lived, up to about 2 minutes and the poised-potential was re-established. After the application of poised-potential timed-out, the voltage generation was virtually zero, from the MFC-PP-MPPT and remained so until day 11, after which, the

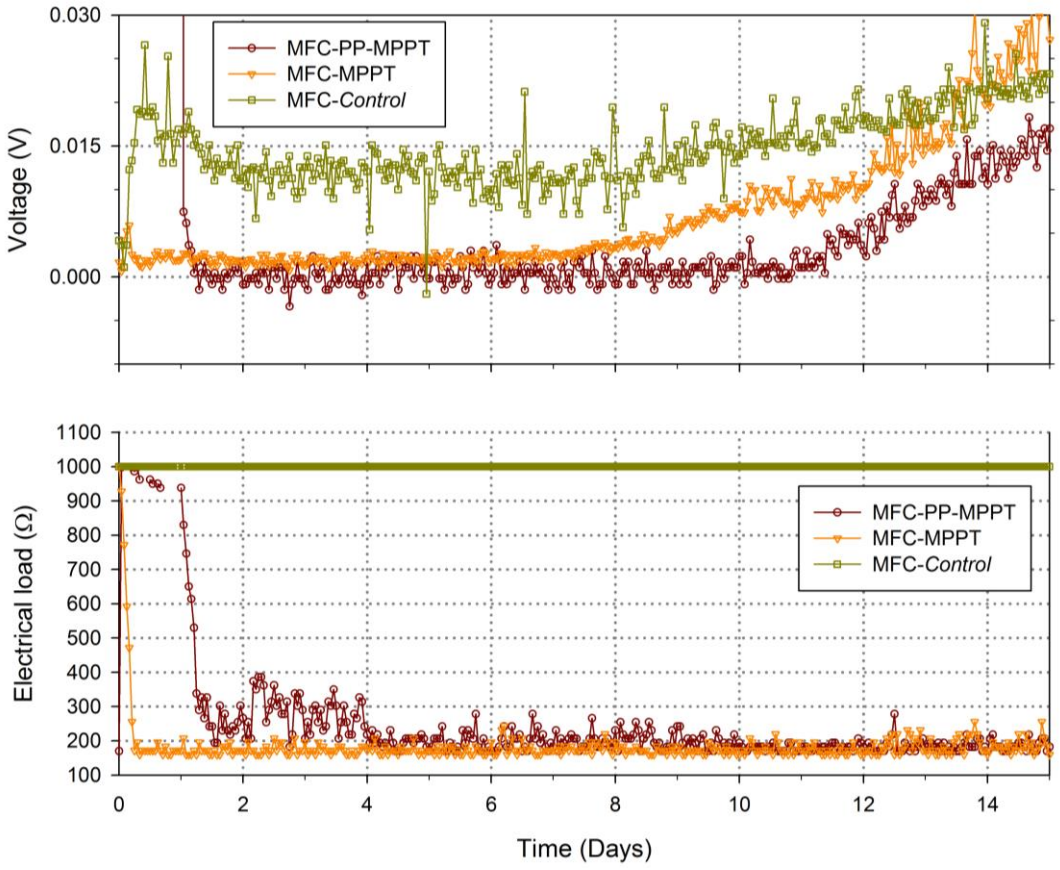

Figure 3.3: Voltage generation from MFC-PP-MPPT, MFC-MPPT and MFC-*Control* during early stages of start-up (From the day of inoculation until day 15).

voltage responded suddenly and began to rise at a rate of 5 mV day^{-1} up to day 18. The application of poised-potential on MFC-PP-MPPT may have surpassed the limit of current production from a large proportion of the electrogenic bacteria to deliver the demanded current, which could have led to an extended period (day 1 – day 10) of low (almost nil) power generation from MFC-PP-MPPT. By contrast, MFC-MPPT and MFC-*Control* showed virtually an immediate and continuous voltage drops of approximately 2.5 mV and 15 mV across 160 Ω and 1 kΩ were observed until day 8, after which they increased at rates of approximately 3 mV day^{-1} and 1 mV day^{-1} until day 15 and day 30, respectively (Figure 3.3).

Figure 3.4 shows the real-time power from each of the three H-type MFCs. It is evident that the power from MFC-PP-MPPT and MFC-MPPT increased to 0.17 mW and 0.22 mW between day 11 – 22 and day 15 – 22, respectively. However, power from MFC-*Control* increased to 0.15 mW much later, between the day 30 – 42. The power generation from MFC-PP-MPPT and MFC-MPPT seemed to have stabilised by day 23 and from MFC-*Control* by day 42. This implies that an active approach for current sourcing can greatly reduce the start-up time, by *circa* 3 weeks in this case, which is almost half the time that of taken by the statically loaded MFC. Here, from the electrical load plot in Figure 3.4, it is evident that the MPPT algorithm (on MFC-PP-MPPT and MFC-MPPT) applied the minimum load (160 Ω) in the absence of discernable power. Also, it was later determined by an identical experimental regime that the start-up time of MFC-*Control* loaded with 500 Ω was still higher relative to the MPPT loaded MFC (Appendix A). As seen in this study, relatively lower loads tend to facilitate earlier start-up compared to those matching the internal resistance (determined *a* priori when the MFC is fully operational and generating power) or indeed higher than this internal resistance. This has also been confirmed by Molognoni et al. (2014) who was able to start their MFC loaded with MPPT load in 14 days in comparison to 49 days taken by the MFC loaded with static load that represented internal resistance (when anode is fully acclimated), thereby reducing the start-up time of their MFC by 2.5 times.

An immediate loss of power was observed when the inoculum media was replaced with the fresh media (as described in section 3.2.1) in MFC-PP-MPPT and MFC-MPPT on day 47 (Figure 3.4) and; in MFC-*Control* on day 56 (Figure 3.5). This could be due to loss of planktonic electrogens and natural mediation. Also, a steady decrease in power after day 48 from MFC-PP-MPPT and MFC-MPPT was observed, which is attributed to the depletion of acetate (Figure 3.4).

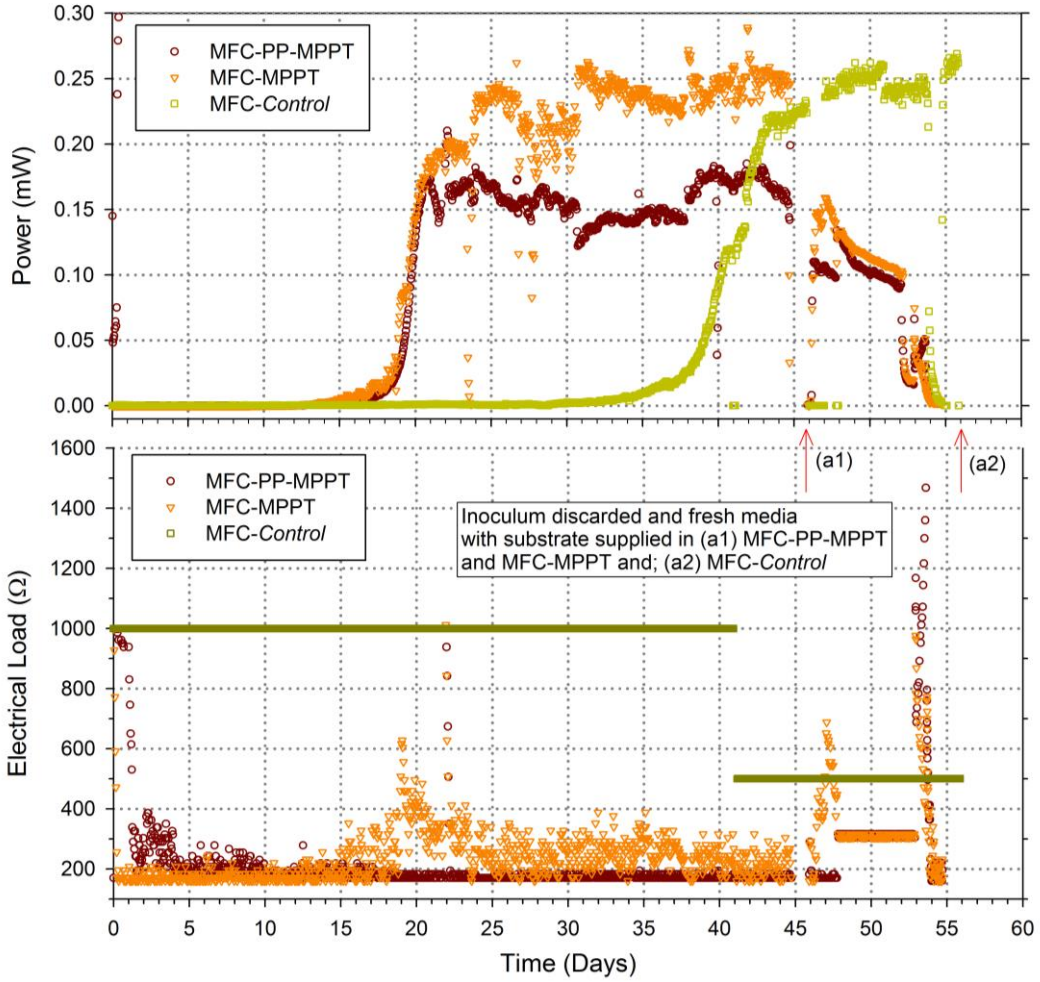

Figure 3.4: Power generation from MFC-PP-MPPT, MFC-MPPT and MFC-*Control* during the start-up. Almost instantaneous power drop intermittently is due to disconnection of MFCs for measurements of power to determine the power curve.

When the subroutine for the application of poised-potential in PP-MPPT algorithm was removed, the algorithm was able to track the peak power as is evident from electrical load plots in Figure 3.5. The delays caused in the decision making and for load alteration by Boolean logic algorithm in PP-MPPT, could be avoided with an improved program structure able to avoid the posed-potential poling subroutine, when it is not needed. Nevertheless, tracking of peak power from MFC-PP-MPPT is evident in Figure 3.5. All three of the MFCs were started with the same initial load of 500 Ω and it is observed that, the MPPT algorithm on MFC-PP-MPPT and MFC-MPPT lowered the load to a minimum value of 160 Ω in the absence of discernable power and increased and varied the load between 200 Ω and 430 Ω in real-time to match the impedance, as opposed to the constant load of 500 Ω applied to the MFC-*Control*. Also, an earlier increase in power from MFC-PP-MPPT and MFC-MPPT can be observed (approximately 4.5 hours compared to 11 hours) than that of MFC-*Control*.

As observed on day 180, the open circuit voltages (OCV) of MFC PP-MPPT, MFC MPPT and MFC Control were 0.838 V, 0.865 V and 0.870 V, respectively.

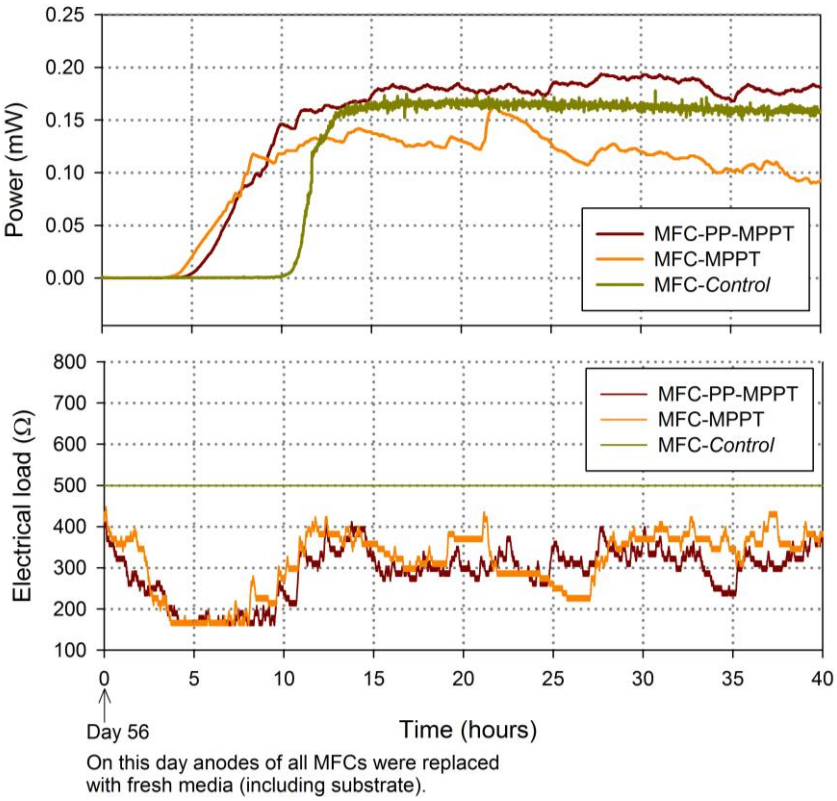

Figure 3.5: Power generation from MFCs (enriched under different start-up strategies) when their anodes were replaced with fresh media.

3.3.2 Development of power

Power level from an MFC is an indication of its performance in response to variations in operating parameters and given that the test systems have identical anode and cathodes materials, geometrical designs and electrolytes; can also be indicative for establishment of an electro-active biofilm.

As per the power measured immediately after the first rise of power seen after inoculation on day 23, the maximum power generated was 0.22 mW (Figure 3.6a), which remained relatively constant until day 46 (0.23 mW). This is because the PP-MPPT algorithm was not able to track the peak power and applied a virtually constant lower limit of loading (approximately 160 Ω). However, an increase in the current associated with the maximum power was observed as per day 46, with a shift in the load from 500 Ω to 300 Ω (Figure 3.6a).

The maximum power fell to 0.14 mW by day 65 when the inoculum media was replaced with the fresh media, but resumed to 0.23 mW by day 180.

Maximum power from MFC-MPPT was 0.21 mW (Figure 3.6b) on day 23 which increased to 0.28 mW by day 39 and further to 0.30 mW by day 46. The shift in the internal resistance (apparent from the power curve) from 500 Ω to 300 Ω was observed as per the power measurements on day 39. Again, like MFC-PP-MPPT, the maximum power from MFC-MPPT had fallen to 0.20 mW after replacing the media on day 65. Further decrease in power of 0.17 mW was noticed as per day 180.

On the contrary, the maximum power from MFC-*Control* reactor as per the day 42 (after the first significant rise in power) was 0.15 mW (Figure 3.6c) at 500 Ω and the power curve presented a considerable, what is referred to as 'power overshoot' peaking at around 250 Ω (0.04 mW) external loading. From this information, the static load value of MFC-Control was reduced to 500 Ω (on day 42) which better represented the maximum power point than the *a priori* selected 1 kΩ. Comparing this power curve (on day 42) to the other power curves by the same system, MFC-*Control* on later days, it appears that it produced lower power at higher current loading on day 42 than it was capable of, as on day 49. Therefore, in this context it should be referred as 'power undershoot' as opposed to 'power overshoot' in the study by Boghani et al. (2013). However, the normal usage is 'power overshoot' which is widely used by researchers in the field of MFC/BES. This phenomenon has been observed and argued previously (Hong et al., 2011, Winfield et al., 2011) and one of the reasons for its occurrence in MFCs is attributed to insufficient electrogen selection/enrichment at higher currents loading range. After 7 days of operation, the maximum power increased to 0.22 mW as per the measurements on day 49 and also the power undershoot disappeared and power further increased to 0.24 mW by day 56, having maintained 500 Ω loading. After replacing the inoculum with the media in anode chamber, the maximum power measured was 0.19 mW on day 85 which increased to 0.25 mW by day 180.

MFC-PP-MPPT and MFC-MPPT produced 46.7% (0.22 mW) and 40.0% (0.21 mW) more power initially (as per measured on day 23) compared to the power produced by MFC-*Control* (0.15 mW on day 42) and also, MFC-*Control* suffered from the power undershoot at the start-up. Operating the MFC-*Control* at 'snap-shot' maximum power point load of 500 Ω eliminated the power undershoot and increased the power but only up to maximum attainable power (0.24 mW on day 56) and did not increase further as opposed to the MFC-MPPT which showed 0.30 mW in 46 days. Power from MFC-PP-MPPT did not seem to increase either, after the

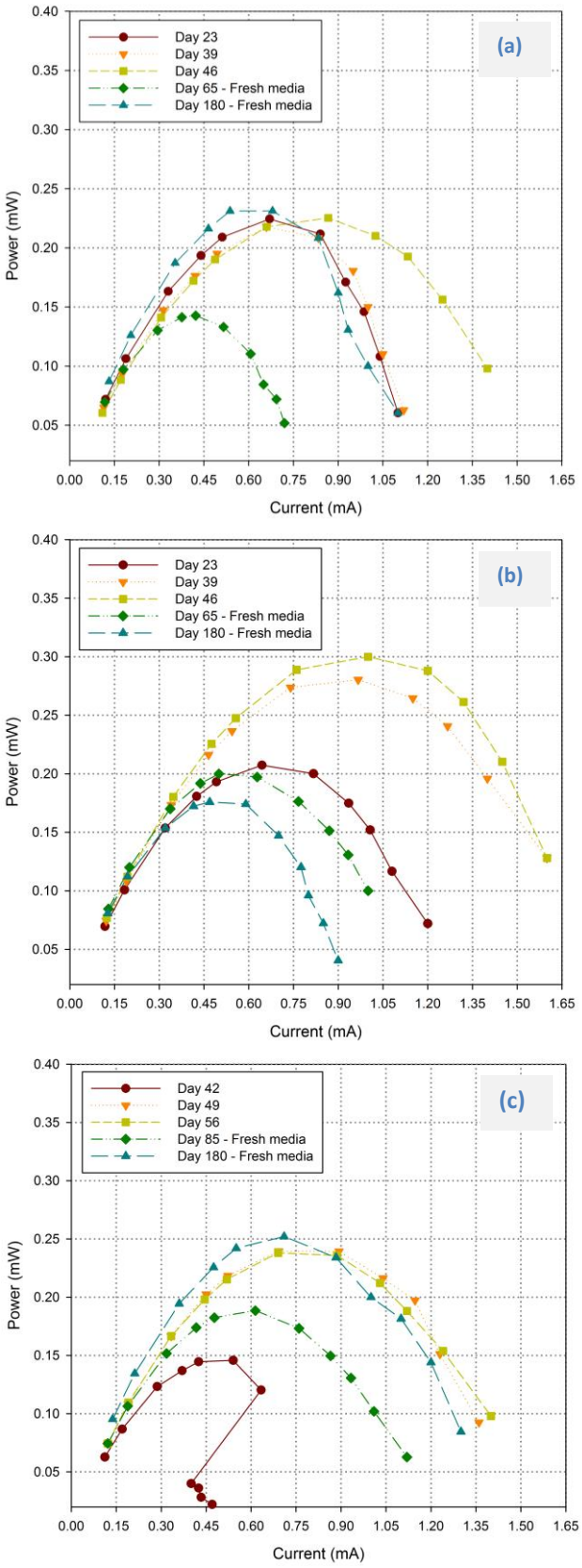

Figure 3.6: Power curves (power against current) showing power from (a) MFC-PP-MPPT, (b) MFC-MPPT and (c) MFC-*Control*.

initial increase, which can be attributed to a virtually constant loading (170 Ω – 194 Ω, shown in Figure 3.4) applied by the PP-MPPT algorithm to MFC even after the start-up. In case of MFC-MPPT, the maximum power progressively increased and the internal resistance (apparent from the power curves) seemed to have reduced up to approximately 300 Ω. This indicates that the continuous impedance matching using peak power point tracking techniques can be beneficial to the MFCs compared to the static load, no matter the load is higher, lower or same as the 'snap shot' maximum power point load.

Removing the conditional statement from PP-MPPT algorithm (as the application of poised-potential was no longer needed) on day 56 enabled the algorithm to track the peak power point more closely (Figure 3.5). In future, the implementation of PP-MPPT should be considered for fixed duration rather than the 'on/off' poised-potential application based on conditional statement. Doing so, would easily avoid execution delay caused in the PP-MPPT. Furthermore, the application of poised-potential was for a much shorter period of time in comparison to study by Wang et al. (2009) who had poised the anode at potential of +200 mV vs. Ag/AgCl electrode (Saturated KCl, BASi) for 41 days. Also, the potential of +600 mV has been shown to have positive effect on the performance of MFCs (Srikanth et al., 2010) and so in this study, it would be difficult to believe that the application of +645 mV vs. Ag/AgCl (Saturated KCl, BASi) would have made a significant difference in MFC-PP-MPPT compared to operating it on only MPPT. And therefore, a mere application of MPPT would probably suffice which can start the MFCs in relatively shorter time period with a head start on peak power as also suggested by Mologni et al. (2014). Although, a long term improvement in the power by MPPT could further be investigated.

3.3.3 Bioelectrochemical activity

Figure 3.7 shows cyclic voltammograms for MFC-PP-MPPT, MFC-MPPT and MFC-*Control*. The oxidation peaks (associated with oxidation of acetate) resulting from the biofilm at the anodes are evident at -0.211 V, -0.215 V and -0.225 V (vs. Ag/AgCl, Saturated KCl) with their associated current 2.94 mA, 2.74 mA and 0.77 mA for MFC-PP-MPPT, MFC-MPPT and MFC-*Control*, respectively. An additional peak is also observable at -0.157 V (vs. Ag/AgCl, Saturated KCl) in the case of MFC PP-MPPT. During the backward scan of CV (from +0.8 V to -0.8 V), oxidation peaks can be seen at similar potentials to those in the forward scan but the associated currents were 0.67 mA for MFC-PP-MPPT and MFC-MPPT; and 0.41 mA for MFC-*Control*.

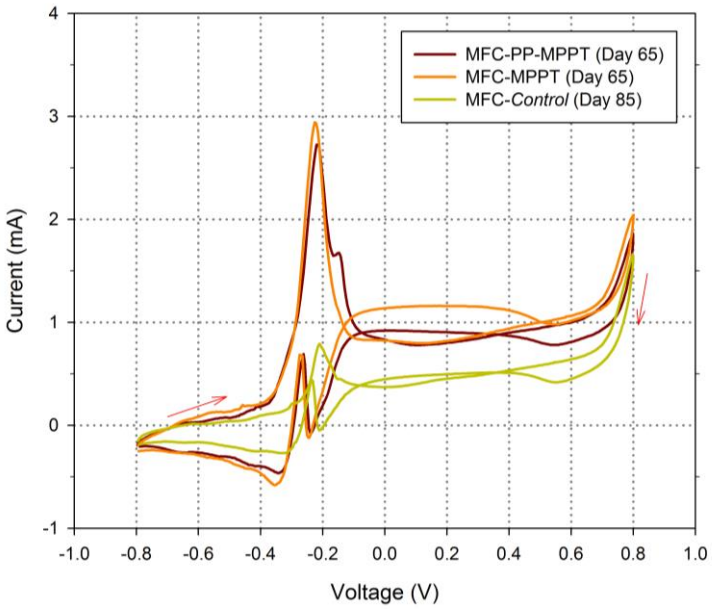

Figure 3.7: Cyclic voltammetry for enriched electrogenic biofilms on anodes (vs. Ag/AgCl reference electrode, Saturated KCl) of H-type MFCs started with different start-up strategies. The red arrows indicate voltage sweep direction.

In the study by Kim et al., (2006), the oxidation peak potential observed in cyclic voltammograms of their MFC was -0.200 V vs. Ag/AgCl (Saturated KCl) which they attributed to have resulted from electrogenic bacteria with Fe-reducing capability, from e.g. strain GEB-1 (from *Gammaproteobacteria* electrode biofilm). The oxidation peak potentials observed in this study seem to be in close match to theirs and it is expected that this oxidation peak observed would be due to the electrogenic bacteria much like in their study and confirms the bioelectrochemical activity. The current measured associated with the oxidation peak from the CVs of MFC-PP-MPPT and MFC-MPPT shows a 3.5-fold higher than that of the MFC-*Control* (Figure 3.7). This could imply that the electrogenic bacterial population/bioelectrochemical activity from MPPT assisted enriched anodes were higher than that of the MFC-*Control*. Here, the internal resistance of H-type MFC is much higher (300 Ω - 500 Ω) compared to a similar anodic volume MFCs studied by Kim et al. (2011a) and Aelterman et al. (2006) and thus, the bioelectrochemical activity was not necessarily evident in the power performance. However, it is expected that the MPPT strategy would be more favourable in delivering high power performance from MFCs with lower internal resistance. The study by Premier et al. (2011), suggests that the anodes developed through the enforced demand of continuously maximum power can cause selective pressure on the electrogenic biofilm to develop better and efficient electron transport chains with greater amount of electrogens.

The experiment presented in this chapter demonstrated for the first time that the application of much lower electrical loading than that of the MFC's internal resistance during the start-up could facilitate fast growth (or colonisation) of electrogens on the anode of MFC and automated start-up through the 'hill climbing' algorithm to match impedance of MFC in real-time could improve biocatalytic performance of the MFC. This is a cost-effective strategy for the enrichment of electrogens on the anode of MFCs with enhanced start-up time, power performance and the biocatalytic activity. This automated start-up of MFCs will be useful in deploying MFCs at an industrial scale.

4. Modeling of the MFC process – a black box approach

4.1 Introduction

Applications of MFCs to wastewater treatment and waste streams may benefit from their operation at high current densities and power as the COD removal through electrogenic metabolism in their anodic biofilm is directly related to the current density. So, controlling the cell potential or power production from MFCs will be of an importance amongst other amenable enhancement of power production through the materials, architectural design and many more. For effective controller design, the dynamic behaviour of MFC should be identified and models should be obtained over the entire operational range of the MFC for their use in controllers.

4.2 Materials and methods

4.2.1 Fabrication and operation of MFC

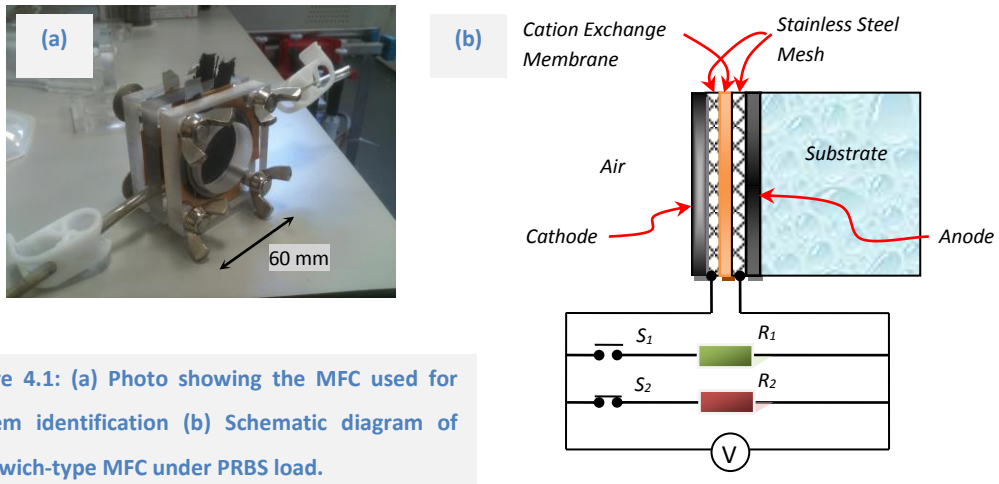

Figure 4.1: (a) Photo showing the MFC used for system identification (b) Schematic diagram of sandwich-type MFC under PRBS load.

Three Perspex sheets of 10 mm thickness with 35 mm diameter were used to hold two sandwich assemblies of anode, current collectors, membrane and cathode (Figure 4.1a). Plain carbon cloth (BASF Fuel Cell Inc., NJ, USA) and 5 mg cm^{-2} Pt coated carbon cloth (BASF Fuel Cell Inc.) were used as anodes and cathodes, respectively. Stainless steel woven wire mesh (size 70, 0.2 mm aperture) was used as current collectors (Mesh Direct, Burslem, UK). The anode volume was 9.6 (+0/-1.0) mL.

To start the MFC, the inoculum was provided to MFC along with sodium acetate, phosphate buffer and nutrient media as previously described in section 3.2.1 but the MFC was

connected to an electrical load of 1 kΩ. Once the stable power generation was established, inoculum was discarded and the anode chamber was filled with fresh media containing 40 mM acetate. Throughout this experiment, the MFC was fed well in the batch mode.

4.2.2 Perturbation of MFC through PRBS and step inputs

A pseudo-random binary signal (PRBS) of 8-bit was generated in LabVIEW™ software (National Instruments™) and communicated through NI USB 6009 DAQ™ device (National Instruments™) to provide transistor-transistor logic (TTL) signal (0-5 V). TTL signal caused two relays (PVN012PbF, International Rectifier, CA, USA) to switch through a transistor array (ULN2003A, STMicroelectronics, Geneva, Switzerland) following the logic NOT, i.e. switch *S1* would be off when switch *S2* would be on and vice versa, to apply the load (*input/cause*) to the MFC as shown in Figure 4.1b. Load steps of 50 ± 5 Ω intervals, ranging from 100 Ω to 1 kΩ were modulated through the PRBS signal. The minimum switching time period of PRBS signal was 5 s and the potential drop (*output/effect*) across the load was measured at sampling rate of 2 samples sec^{-1}. Load steps of 1.7 kΩ to 2 kΩ and 4.4 kΩ to 5 kΩ were also used and the amplitude of these steps was larger to compensate for very low static gain for the linear models at higher loading on MFCs.

Responses (in terms of voltage drop across the load) from MFCs were also measured when they were subjected to input loads ranging from 100 Ω to 1 kΩ in 50 Ω load steps using resistance decade box (Resistance Decade Box, TENMA).

Power from the MFC was measured to see the power and voltage variation at steady state vs. at various electrical load levels. The electrical load was varied from 50 kΩ to 200 Ω in steps and resulting current was measured by using NI USB-6009 (National Instruments™). Electric current and power were calculated as described in section 3.2.3.1 and power was normalised to the empty anodic chamber volume of 9.6 mL.

4.2.3 Identification of the MFC process

4.2.3.1 Preparation of PRBS data for analysis

The data collected from the perturbation experiments (*input* i.e. electrical load and *output*, i.e. potential drop across the load) were visually inspected off-line for the outliers and trends before proceeding for the identification of the process. The data sets associated with PRBS loading of 150 Ω – 200 Ω, 650 Ω – 700 Ω and 855 Ω – 900 Ω contained 0.07% (of the sampled data) outliers. They were considered to have come from the disturbances to the

electrical connections and were removed and replaced with the mean value of the immediate neighbouring sampled values. In the PRBS data, some trends were observable which was attributed to the addition of substrate in the anode chamber and/or substrate depletion after long period of operation of the MFC during application of PRBS. So, the trends and offsets were removed using a *DETREND* function available in MATLAB® (The MathWorks, Inc., Cambridge, UK) to remove any linear trends in the PRBS *output* data and signal offsets by subtracting the sample means for signals.

The PRBS data were normalised by subtracting the mean of the data and dividing by its standard deviation as described by Premier et al. (1999) and then imported into a System Identification Toolbox™ (The MathWorks, Inc.) environment in MATLAB® for identification. The data was then split into two equal parts to provide separate data for parameter estimation (Estimation Data) and model validation (Validation Data). Additionally, the data for PRBS loading of 804 Ω – 851 Ω was split in four equal parts and each of those parts were considered for the identification separately.

Also, an output data corresponding to PRBS loading of 804 Ω – 851 Ω (in its normalised form) was filtered using a 5th order Butterworth filter as used by Premier et al. (1999) to appreciate the dynamics of the MFC but it was not used in the identification process.

4.2.3.2 Models and their parameter estimation

The step responses from the MFC seemed to the suggest the process models to be likely of the first-order type and therefore, the process models of the general transfer function form as shown in Eq. 4.1 were considered.

$$\frac{V_o}{R_i} = \frac{k}{1+T_p \cdot s} \qquad \textit{Eq. 4.1}$$

Where; V_o is voltage drop (*output,* in volts) across the load connected to MFC, R_i is load (*input,* in Ω) connected to the MFC and *s* is the Laplace variable. *k* is steady-state gain (mV Ω^{-1}) and T_p (s) is the time constant which were determined at several operating points as per the PRBS data.

Also, models of the general form as described by Premier et al. (1999) for Single Input Single Output (SISO) AutoRegressive with eXtra inputs (ARX) were considered for the PRBS data for loading of 200.6 Ω – 250.4 Ω onwards.

To estimate the parameters of the process models (as in Eq. 4.1), an iterative estimation algorithm with minimising prediction-error method (Ljung, 1999) as implemented in the System Identification Toolbox™, MATLAB® was employed and similarly, a least squares estimation method (Ljung, 1999) was employed for the ARX models.

For the data collected from step input experiments, 1st order system dynamics with time constants τ, steady-state gains K and no time delay in the response were considered. The responses (*output,* in volts) from MFC were simulated by using the parameters estimated from the step responses as in Eq. 4.2.

$$V_o(t) = R_i \cdot K \cdot \left[1 - \exp\left(-\frac{t}{\tau}\right)\right] \qquad \textit{Eq. 4.2}$$

Where; $V_o(t)$ is voltage (*output*, in volts) at time t (in sec), R_i is the electrical load (*input*, in Ω), K is steady-state gain (V Ω^{-1}) and τ is the time constant (in sec).

4.2.3.3 Model validation

Model validation was considered through the analysis of residuals as described by Ljung (2012).

Also, from validation data sets, the time-series normalised output was simulated and predicted using the identified process models and ARX models, respectively. The data were plotted along with the validation data sets to see if the model output matches the measured output. The best fit (in %) of model response to the actual response data in validation data set was determined using Eq. 4.3 (Ljung, 2012) and is presented in Table 4.1 for all identified models.

$$Best\ fit\ (\%) = \left(1 - \frac{|v - \hat{v}|}{|v - \bar{v}|}\right) \times 100 \qquad \textit{Eq. 4.3}$$

Here, v is measured output, $\hat{v}$ is the model output and $\bar{v}$ is the mean of measured output.

4.3 Results and discussion

4.3.1 Piecewise linearised MFC models

4.3.1.1 MFC performance and step responses

Power generation from the MFC was measured to determine the operation range, i.e. voltage generation and associated power levels resulting from variations in electrical loading while keeping other operational parameters virtually constant, such as substrate concentration

(40 mM sodium acetate), pH (7.0) and temperature (30 ± 2 °C) and is presented in Figure 4.2. Logarithmic scale (Log_{10}) is applied to the electrical load data to reduce the spread of the

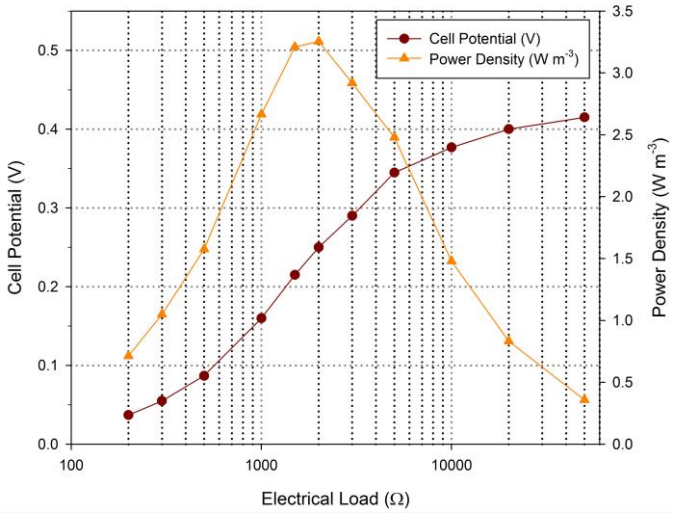

Figure 4.2: Power density and cell potential as function of electrical load for MFC used in the study. The abscissa is represented in Log_{10} scale.

voltage and power data on the plot. The peak power of 3.26 W m^{-3} was produced at 2 kΩ and the potential drop across the connected load varied from 0.415 V to 0.037 V when the electrical load was varied from 50 kΩ to 200 Ω.

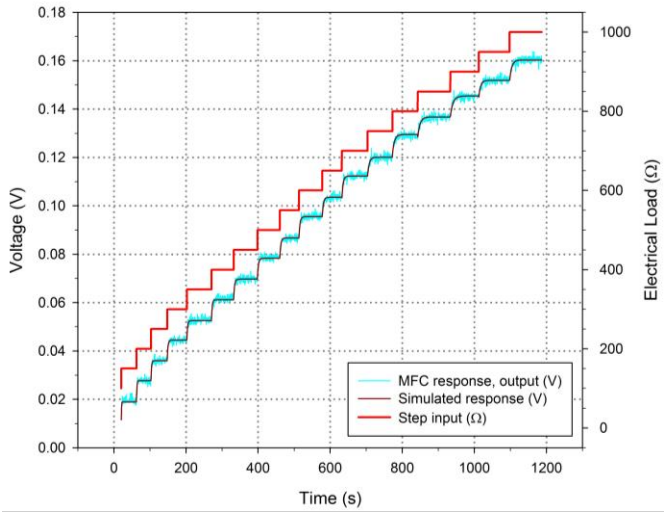

Figure 4.3: MFC responses and simulated MFC responses (assuming 1st order process) to step inputs (Ω). The parameters for simulated MFC responses are determined from the corresponding MFC step responses.

Responses (in terms of voltage) from the MFC are shown in Figure 4.3, when they were subjected to the step inputs in the range of 100 Ω to 1 kΩ. The MFC was given step inputs of 50 Ω amplitude within the range 100 Ω to 1 kΩ to assess the transient behaviour of the MFC output (in terms of voltage) at various operating level and to visually inspect to determine the

order of the model to apply in the identification process. The estimated parameters (assuming linear 1st order dynamics), time constants, τ and steady-state gains, K determined from the step response data are presented in Figure 4.4. As evident from Figure 4.4, the time constants increased from 0.5 s to 7.3 s as the load was increased and also the steady-state gains varied from 0.12 and 0.20 mV Ω^{-1} over the same range of electrical load.

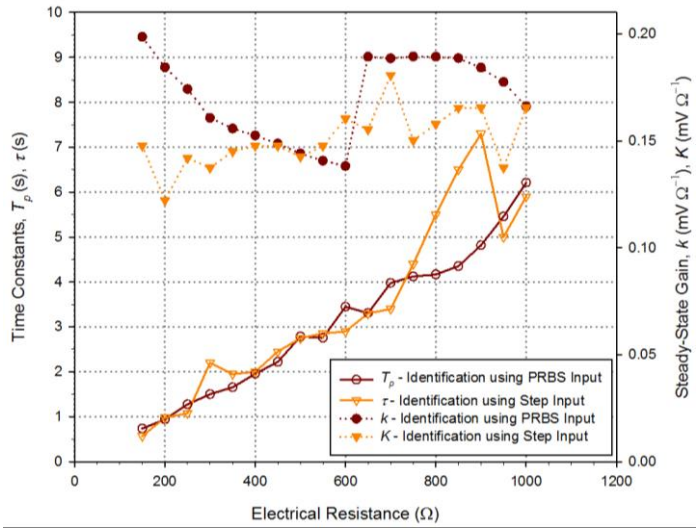

Figure 4.4: Assuming 1st order-type responses from the MFC, time constants (T_p, τ) and steady state gains (k, K) determined from system identification using PRBS input and step input at various loads between 150 Ω and 1 kΩ.

4.3.1.2 Process models

As informed by the step responses shown in Figure 4.3, process models as per Eq. 4.1 were employed to estimate the parameters by statistical approach (identification process as described in section 4.2.3.2). The so obtained estimated time constant (T_p) and steady-state gains (k) are presented in Figure 4.4. When loading was varied from relatively low loading (of 100 Ω – 150 Ω) to relatively higher loading (of 950 Ω – 1 kΩ) it is clear that the time constants gradually increased from 0.7 s – 6.2 s and the steady-state gains (k) varied from 0.14 mV Ω^{-1} and 0.20 mV Ω^{-1}. Time constants and steady state gains for the higher loading steps (1.7 kΩ – 2 kΩ and 4.4 kΩ – 5 kΩ) were 4.9 s and 12.3 s and; 0.175 mV Ω^{-1} and 0.091 mV Ω^{-1}, respectively (not shown in Figure 4.4).

Responses from MFCs were almost instantaneous at the application of step load changes (in both, step and PRBS inputs), i.e. no significant delays in the responses were detected. The variation in steady-state gains (k, K) was found to be within 0.08 mV Ω^{-1} (between 0.12 and 0.20 mV Ω^{-1}) which suggests that there was only about 4 mV variation for a

50 Ω step change, throughout the range 100 Ω – 1 kΩ. Also, lower steady-state gain (0.091 mV Ω^{-1}) for the PRBS loading of 4.4 kΩ to 5 kΩ was much lower than that of the gains at higher current regions, i.e. lower external loadings and for that reason, PRBS loading was not carried out at higher loading than 5 kΩ. This is evident from the voltage curve where the increase in voltage is almost linearly proportional to the increase in the loading in the range of 200 Ω to 2 kΩ (voltage plot in Figure 4.2) but the voltage curve in the higher loading is relatively flat and starts to deviate and saturate at higher loadings. At higher loadings, when the load is very high compared to the internal resistance of MFC, the MFC voltage approaches the open circuit potential of MFC (Zhang and Liu, 2010).

Gradual but substantial increase in the time constant (from 0.5 s to 7.3 s) over the range of applied electrical loads (150 Ω to 1 kΩ) shows that the speed of response which defines the system dynamics, slowed and became more dominant as the system approached maximum power point (Figure 4.2 and Figure 4.4). This confirms that the MFC system is nonlinear and such nonlinearity (change in model parameters with the change in operational point) would need to be considered when designing a controller, because the controller designed for small time constant (at high current region) would not be adequate for relatively large time constant near the maximum power point. However, series of linear models (1st order process models and also ARX models presented in section 4.3.1.3) identified by piece-wise linearization of the MFC system in this study over the range of operational loading, can be employed in the controller design to remedy such nonlinearity in the MFC system.

A good agreement is found in electrical loading range of 100 Ω to 800 Ω when comparing time constants obtained from step response analyses and identification of process models. However, some divergence is observed in the region of 800 Ω to 950 Ω which could be due to the prolonged perturbation from the applied PRBS loading that may have affected the electrogenic biofilm to be more responsive system, i.e. relatively smaller time constants than resulted from exciting MFC with single steps.

4.3.1.3 ARX models

The parameters for the ARX models as per the general form of transfer function shown (in *z* – domain) in Eq. 4.1 are shown in Table 4.1.

$$\frac{V_o}{R_i} = \frac{K \cdot (z - z_1)(z^2 - z_b \cdot z + z_c)}{(z - p_1)(z - p_2)(z^2 - p_b \cdot z + p_c)} \qquad \textit{Eq. 4.1}$$

Here, K is steady-state gain, z_1 is zero, p_1 and p_2 are poles, z_b, z_c, p_b, p_c are coefficients of quadratic form of zero and pole terms.

Table 4.1: Parameters of 4th order ARX model transfer function and model fits (%) for ARX and process models from validation.

PRBS Loading	K (× 10^{-4})	z_1	z_b	z_c	p_1	p_2	p_b	p_c	Model fit (ARX) %	Model fit (Process†) %
101.2 Ω – 150.4 Ω	-	-	-	-	-	-	-	-	-	44.08
151.5 Ω– 200.5 Ω	-	-	-	-	-	-	-	-	-	41.57
200.6 Ω – 250.4 Ω	1.67	-0.38	0.02	0.12	0.70	-0.51	-0.12	0.25	77.54	76.76
250.8 Ω – 301.6 Ω	1.54	-0.51	0.12	0.17	0.73	-0.47	-0.19	0.28	77.23	76.30
302 Ω – 351.5 Ω	1.50	-0.04	-0.26	0.15	0.77	-0.55	-0.10	0.33	73.38	73.38
352.2 Ω – 400.7 Ω	1.47	0.39	-0.68	0.49	0.82	-0.43	-0.20	0.24	75.13	74.80
402.6 Ω – 450.5 Ω	1.44	-0.15	-0.18	0.14	0.81	-0.55	-0.11	0.32	71.89	71.31
452.7 Ω – 500.3 Ω	1.39	0.12	-0.52	0.29	0.83	-0.54	-0.10	0.33	67.76	66.69
503.1 Ω – 550.3 Ω	1.37	0.19	-0.57	0.27	0.84	-0.51	-0.13	0.32	64.22	63.75
553.2 Ω – 600.2 Ω	1.35	0.13	-0.59	0.27	0.84	-0.52	-0.18	0.32	64.24	62.54
602.5 Ω – 650.1 Ω	1.83	-0.43	0.01 ×10^{-3}	0.10	0.86	-0.47	-0.20	0.37	64.59	64.01
652.7 Ω – 701.3 Ω	1.84	-0.60	0.24	0.14	0.86	-0.59	-0.06	0.33	71.40	70.68
704 Ω – 751.3 Ω	1.85	-0.07	-0.54	0.19	0.87	-0.60	-0.09	0.38	71.16	70.80
754.7 Ω – 802 Ω	1.85	-0.27	-0.24	0.17	0.88	-0.51	-0.20	0.38	69.89	70.06
804 Ω – 851 Ω	1.85	0.18	-0.60	0.36	0.89	-0.58	-0.11	0.34	67.52	66.51
804 Ω – 851 Ω (part 1 of 4)	1.85	0.39	-1.43	0.81	0.91	-0.66	-0.01	0.32	65.70	64.79
804 Ω – 851 Ω (part 2 of 4)	1.85	0.31	-0.56	0.40	0.88	-0.60	-0.16	0.34	66.61	64.79
804 Ω – 851 Ω (part 3 of 4)	1.85	-0.52	0.36	0.34	0.87	-0.61	-0.07	0.40	67.59	67.81
804 Ω – 851 Ω (part 4 of 4)	1.85	-0.44	0.24	0.34	0.87	-0.52	-0.21	0.34	66.73	63.05
855 Ω – 901 Ω	1.80	-0.57	0.04	0.19	0.89	-0.55	-0.23	0.37	62.19	61.81
904 Ω – 951 Ω	1.74	-0.42	-0.16	0.41	0.87	-0.59	-0.12	0.38	57.14	58.18
954 Ω – 1 kΩ	1.62	-0.44	-0.02	0.33	0.89	-0.60	-0.12	0.40	53.06	52.84
1.7 kΩ – 2 kΩ	1.73	0.83	-0.66	0.38	0.91	-0.59	-0.04	0.34	53.10	30.11
4.4 kΩ – 5 kΩ	0.90	-0.63	0.42	0.12	0.81	-0.62	-0.07	0.36	30.99	21.48

The black box ARX models of the MFCs do not represent the underlying processes but, can be utilised in the design of control strategies/controllers. Linear controller can be sufficient to be operated in a narrow operating range but when the whole operating range is considered, the identified models at different operating levels can be utilised in appropriate control

† Parameters for process models are presented in Figure 4.4 for PRBS loading of up to 1 kΩ. Time constant, T_p and steady-state, k gain are 4.9 s (12.3 s) and 0.175 mV Ω^{-1} (0.091 mV Ω^{-1}) for PRBS loading of 1.7 kΩ – 2 kΩ (4.4 kΩ – 5 kΩ).

parameterisation for use in adaptive control e.g. gain scheduling (Rugh and Shamma, 2000), enabling optimal MFC control throughout the operating range.

4.3.2 Validation of the process and ARX models

The trueness of process and ARX models identified and presented in section 4.3.1 was validated through the analyses of residuals and best fit (%) of simulated output to the PRBS inputs as described in section 4.2.3.3.

The difference between 'predicted output' and 'measured output' from validation data sets, i.e. residuals (errors) were analysed using auto and cross-correlation techniques to investigate their confidence limits (95%).

There should not be correlation on residuals if the residuals do not have relative temporal delay and the autocorrelation function within 95% confidence intervals means that the model and residuals are un-correlated and therefore, it grants the validity to the model as shown in Figure 4.5a. Similarly, cross-correlation was performed between residuals and the normalised inputs for all the models identified in section 4.3.1.2 and 4.3.1.3. If the cross-correlation function falls within the 95% confidence interval levels, the residuals are deemed to be un-correlated to the input.

For PRBS loading of up to 200.5 Ω, the autocorrelations of residuals from process models were found to be within 95 % confidence interval and an example for 151.5 Ω – 200.5 Ω is shown in Figure 4.5a. This means that the process models for the PRBS loading of up to 200.5 Ω described dynamics of the MFC to a relatively high level (95%) of confidence. For the PRBS loading of 200.6 Ω – 250.4 Ω and higher, the autocorrelation function did not meet the criteria of 95% confidence level, as illustrated in Figure 4.5b for the PRBS loading of 804 Ω – 851 Ω. This indicates that the dynamics presented by the validation data sets were not fully described by the 1st order process models. Selecting a higher order (up to 3rd) models did not improve the autocorrelations (data not shown). Therefore for this reason, an alternative to process models, linear ARX model of 4th order was considered which improved the autocorrelation function as shown in Figure 4.5b.

Cross-correlation function for the PRBS loading of 151.5 Ω – 200.5 Ω (Figure 4.5a) was within the confidence interval (95%) except for the limited range of lag (sample) 1 to -4. For PRBS loading higher than 200.5 Ω, cross-correlation function falls outside of the confidence intervals for both, process and ARX models and it can be seen in Figure 4.5b for the PRBS loading of 804 Ω – 851 Ω. Figure 4.6 shows a portion of 804 Ω – 851 Ω along with the filtered output. The filtered signal clearly shows oscillations in the output from the MFC. 1st order

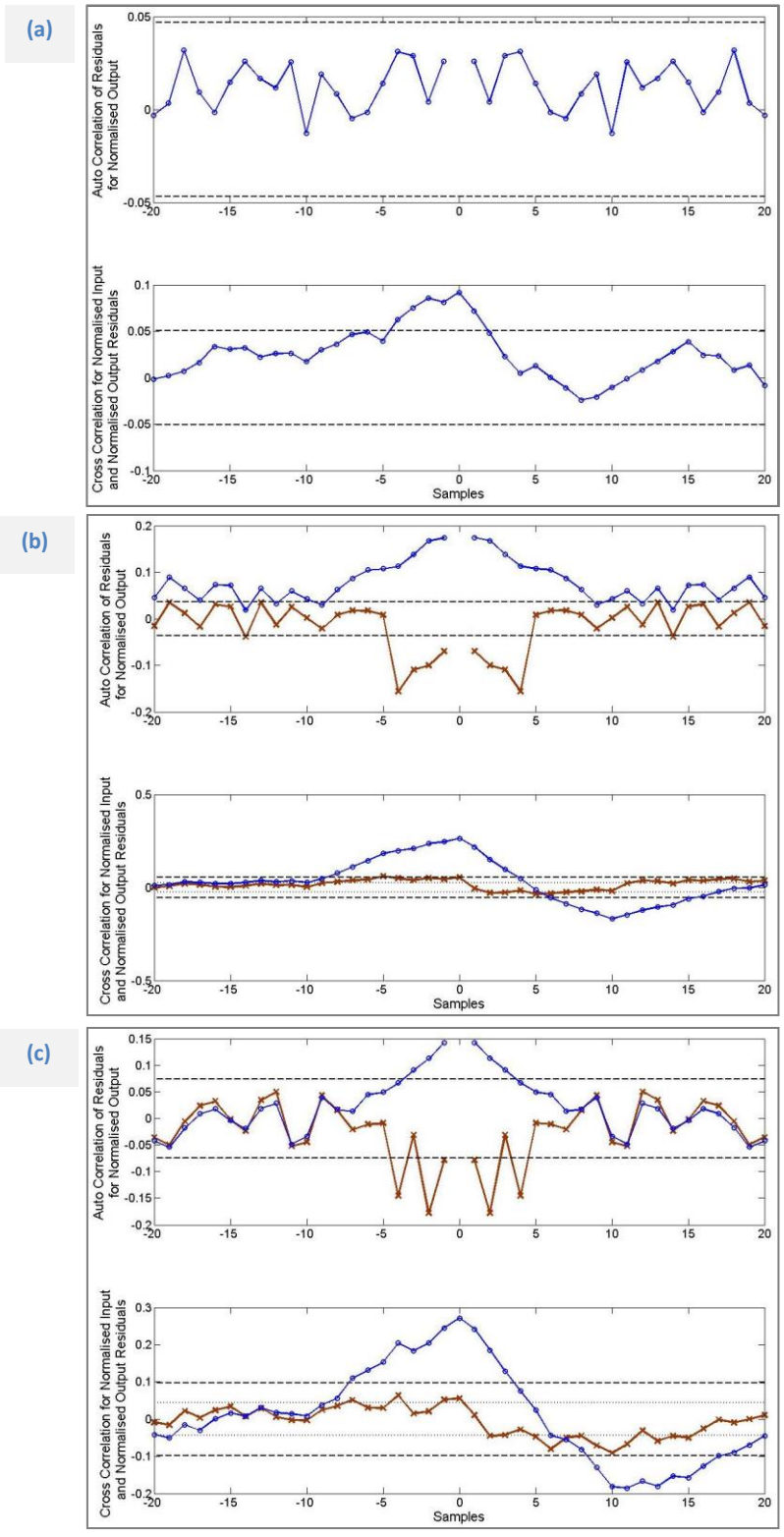

Figure 4.5: Autocorrelations and cross-correlations on system identification validation data for PRBS loading of (a) 151.5 Ω – 200.5 Ω; (b) 804 Ω – 851 Ω; and (c) 804 Ω – 851 Ω (1/4th portion of PRBS data). Curves on the graph are ..... (ARX) 95% Confidence Interval +, ... (ARX) 95% Confidence Interval –, – – – (Process) 95% Confidence Interval +, – – – (Process) 95% Confidence Interval –, —○— Process Model and —×— ARX Model.

dynamics do not represent these dynamics and so it appears in the cross-correlations. Moreover, Figure 4.7 shows a portion from the PRBS loading of 804 Ω – 851 Ω with simulated output using 1st order process model and ARX model (all in their normalised form). The best fit for process model and ARX model were 66.51% and 67.52%, respectively. Visually inspecting the simulated data in Figure 4.7, it seems that the actual response deviated noticeably and randomly from the estimated model response as steady-state approached. These deviations could perhaps have an impact on autocorrelations and were not explained by the model.

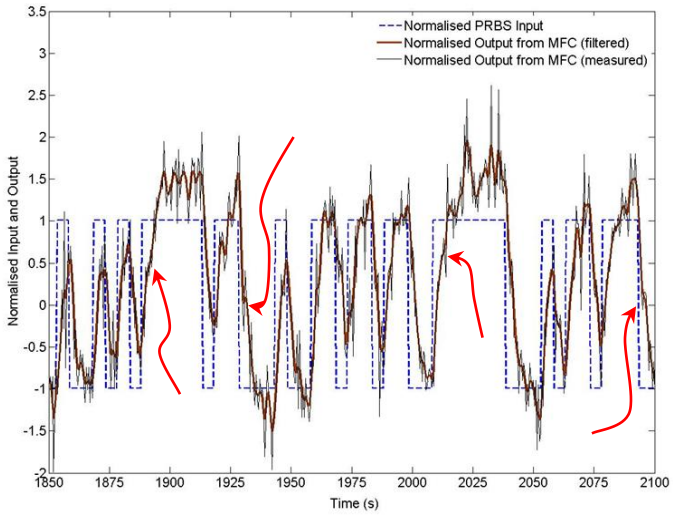

Figure 4.6: A portion of normalised PRBS Input (Ω) to the MFC and subsequent normalised output (V) when the MFC was subjected to PRBS loading of 804 Ω – 851 Ω. The arrows show behaviour similar to the ones observed from the MFCs in studies by Cheng et al. (2008) and Kim et al. (2011a).

When the same PRBS loading data (804 Ω – 851 Ω) was split into four equal parts and each part were subjected to the identification procedure to find process and ARX models, autocorrelation and cross-correlation functions improved and were reasonably within 95% confidence intervals as shown in Figure 4.5c for one of the split part of the PRBS loading of 804 Ω – 851 Ω. Time constants and steady-state gains obtained for the process models from four of these split data sets varied from 4.8 s to 5.1 s and; from 0.187 mV Ω^{-1} to 0.189 mV Ω^{-1}, respectively and they are similar to the ones obtained from the identification from original data set. Visually inspecting the simulated output data (as shown the exemplar in Figure 4.7) and data fit collectively in Table 4.1 suggests that the models were able to represent the measured data.

It is clear that the dynamic response from the MFC became slower as it was subjected to higher loadings. However, this was not compensated through the sampling times for the measurements of voltage response and as a result; the fluctuations in the voltage (noise) became significant in the correlation analyses. To improve the validation of models by residual

analyses technique, a more appropriate slower sampling time with slower dynamics (at higher loadings) shown by MFC should be considered.

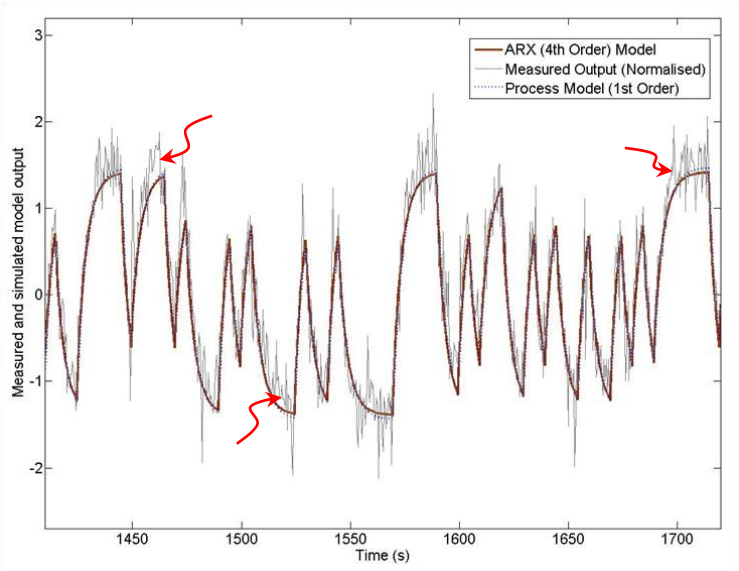

Figure 4.7: Measured (validation data) output and simulated model output for the PRBS loading of 804 Ω – 851 Ω with ARX model of 4th order and process model of 1st order. The arrows indicate random deviation of MFC output from anticipated rise and fall curves.

4.3.3 Plausible model order

To visually assess and appreciate the transient behaviour of the MFC, a portion of filtered output data (as described in section 4.2.3.1) is shown in Figure 4.6 along with the typical application of PRBS signal input that was applied for the loading of 804 Ω – 851 Ω in their normalised form. The arrows in Figure 4.6 indicate behaviour exhibited by the MFC that might be considered to be represented by an approximate 1st order dynamic caused by dominant 1st order pole along with a pair of complex poles (producing oscillatory response) and a zero; when superimposed to a characteristic exponential rise of 1st order system perturbed with a unit step input. If the noise and complex poles (perhaps appeared as an artefact of the filter and noise) are ignored, this behaviour from the MFC seems coherent with studies by Cheng et al. (2008) who observed similar response to the step change in electrical load from 1 Ω to open circuit and suggested that the anodic biofilm have affinity to an electrode potential (-420 mV vs. Ag/AgCl, Saturated KCl, for an acetate consuming MFC) representing saturation of anode respiring bacteria and; by Kim et al. (2011a) who observed similar response from their MFCs in response to step changes in organic loading rate.

As presented in section 4.3.2, the PRBS based process identification assuming 1st order response from MFC at lower loading was shown to be reasonable through the simulation and

autocorrelation functions. However, when loading was increased, the oscillations in the output gradually increased and became more pronounced and significant (as shown in Figure 4.6) as the maximum power point was approached. This suggests that the order of the model representing MFC response may be altering and increase toward the peak power regime even though the responses tend to 1st order. Process models with higher order (2nd and 3rd) of the process models were also considered but they were found to be less able to represent the data and their best fit results were less than 40%. Logan and Regan (2006) confirmed that the anode respiring bacteria in anodic biofilm in MFCs are frequently dominated by *Geobacter* spp. and studies by Richter et al. (2009) showed that cytochromes such as OmcS and OmcZ form support attachment and facilitate electron transport (through redox reactions between cytochromes) from bacteria to anode electrode. MFCs with *Geobacter sulfurreducens* biofilm, electrons liberated from oxidation of acetate is suggested to be transported through the transport chain comprising of internal cytochromes and a matrix of dermal cytochromes within the biofilm and biofilm-electrode interface by Bonanni et al. (2012) and; suggested that the electron transport is limited by the microbial uptake of acetate and transporting the liberated electrons to the cytochromes rather than the cytochromal transport chain (approx. 11 times faster than the acetate uptake by the bacteria). MFC responses are dependent on operating variables such as pH, temperature, substrate concentration and also on processes like electrode kinetics, proton transport through the ion exchange membrane, substrate oxidation and electron transport chain, electrical current, oxygen diffusion to cathode electrode and their interactions among. The possible non-minimum phase effect like response from the MFC presented and ascribed to cytochromal behaviour by Bonanni et al. (2012), is an indicative of a nonlinear behaviour and it is possible that an interplay between the faster and slower dynamic systems could have appeared as an oscillatory higher order dynamics in the identification process.

When piece-wise linearised, the Haldane-like kinetics or other nonlinearities could also lead to oscillatory or higher order behaviours. The MFC system was better represented by a 4th order transfer function at its operational points nearer to the higher power conditions. In general, the responses from MFCs are predictable (Figure 4.3 and Figure 4.7) and the model order reduction should be considered to avoid unnecessary complexity in the control design. As shown in Figure 4.8 for the simulated step response using 1st order process model and ARX model for the PRBS loading of 352.2 Ω – 400.7 Ω, 1st order representation seems comparatively suitable over the higher order (4th) ARX model which could lend only a little

advantage if utilised. Again, the best fit % (shown in Table 4.1) for the ARX and process models confirm the suitability of 1st order process models.

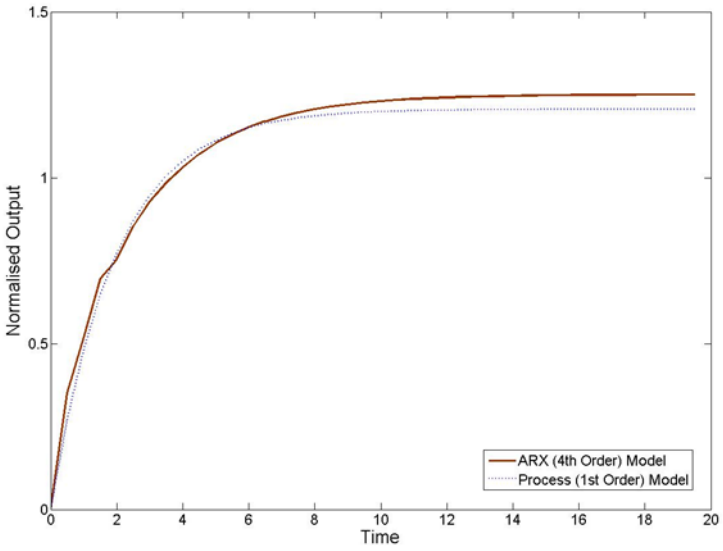

Figure 4.8: Simulated normalised output to a unit step input using models obtained from system identification of PRBS loading of 352.2 Ω – 400.7 Ω.

So, this study demonstrates that a BES representative, MFC could be piecewise linearised about a range of operating regime by applying small perturbation theory using system identification approach and they were found reasonably represented by 1st order linear differential equation/process model (transfer function). These models for the appropriate loading (electrical) range and voltage (or power) output could be scheduled and utilised for control design; providing that the intrinsic parameters such as anodic biofilm, materials, solution conductivity, etc. do not change significantly with time. Alternatively, well established recursive identification algorithms could be employed to track changes in parameters in real-time while implementing the control strategy. The controller strategies in this way could be beneficial in the stack operation of MFCs and improve the system performance.

5. Investigation into MFC stack connectivity to circumvent the voltage reversal and improve stack performance

5.1 Introduction

MFCs typically generate working voltages of *circa* 0.5 V (Oh et al., 2009) and practical applications in powering electronics would require stacking of MFCs to boost the available voltage. Connecting the MFCs in series can cause voltage reversal and also undermine the performance of MFC(s) (Aelterman et al., 2006, Oh et al., 2009, Oh and Logan, 2007). Kim et al. (2011b) demonstrated that the bank of capacitors can be charged in parallel to the MFCs and then discharged in series across the load which would avoid voltage reversal while providing higher voltages through the charged capacitors. This approach relies on usage of relays to configure the capacitors in parallel or series connections which can consume a lot of power for switching the solid state relays compared to the power generated by the MFCs. Also, the impedance from continuously running MFCs may change due to the operational parameters such as pH, substrate concentration, conductivity of anolyte (also catholyte if liquid cathode is used), temperature and loading rates and therefore it will be desired to match its impedance in real-time for maximum power transfer. Blockages may also develop in the flow pathways of continuously fed MFCs which could render the MFCs receiving unbalanced organic substrate and due to which voltage reversal may occur if they are electrically connected in series. So, in this chapter, the connectivity of MFCs for the stack operation is studied which could avoid the reversal of voltage during the stack operation while extracting the maximum available power.

5.2 Methodology

5.2.1 MFC construction, operation and power measurements

Three MFCs of tubular design (Figure 5.1a) *viz.* t-MFC1, t-MFC2 and t-MFC3, utilising annular anodes were constructed with approx. 220 mL anodic volume and enriched as described by Kim et al. (2009) and it was well fed with various effluent such as sucrose, real wastewater and acetate for more than a year prior to their utilisation in this study. The MFC reactor was well fed (in batch mode) with 40 mM sodium acetate with media as described in section 3.2.1 for at least 1 month prior to the experimentation. During the experimentation, reactors were operated at an elevated temperature of 30 ± 2 °C in the temperature controlled chamber.

To determine the power levels from t-MFCs, polarisation curves were determined for t-MFCs by connecting them to an electrical load of 5 kΩ through resistance decade box (Resistance Decade Box, 1% tolerance, TENMA) and stepwise reducing (when steady-state is achieved) the load up to 5 Ω while measuring the voltage using a PC equipped with LabVIEW™ and NI USB-6218 (National Instruments™). Current and power was calculated as described in section 3.2.3.1. Power was normalised to the empty bed volume of the anode.

5.2.2 MFC stack connectivity strategies

Three different MFC stack connectivity strategies were investigated as shown in Figure 5.1b-d and the associated case studies (CS-1, CS-2 and CS-3) are elaborated below.

CS-1: While investigating CS-1, the t-MFCs were connected in conventional series connection where anodes of one t-MFC was connected to the cathode of neighbouring t-MFC and the stack of t-MFCs so obtained was connected to a static load of 150 Ω (Figure 5.1b). Stack load of 150 Ω was chosen to match the overall impedance of the MFC stack based on maximum power point load determined from measured polarisation of individual t-MFCs.

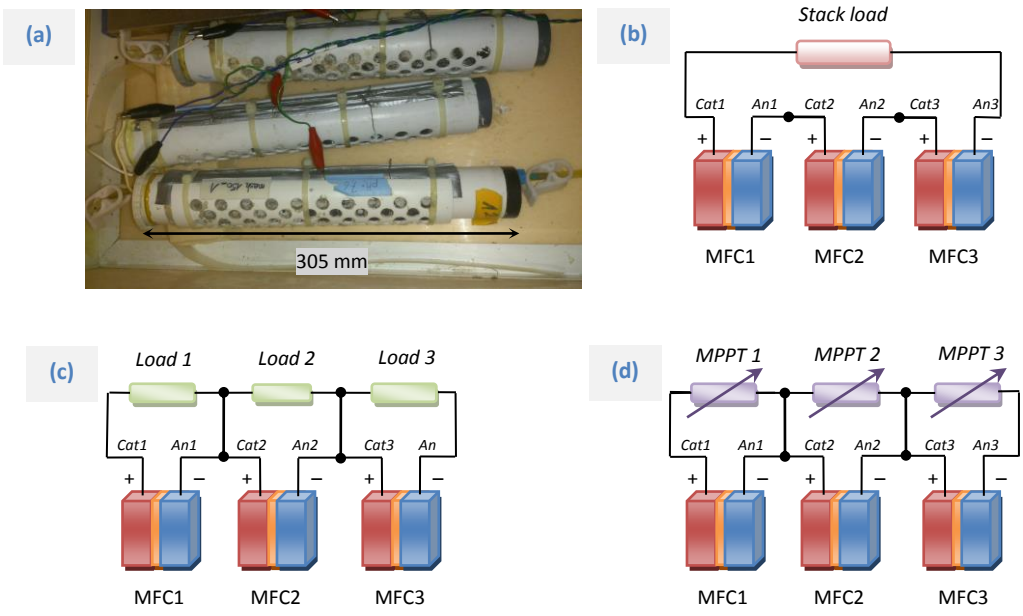

Figure 5.1: (a) Photo showing three tubular MFCs that were used in this study. Schematics showing (b) MFCs connected in series across an overall load of 150 Ω (unless otherwise specified) to match the collective internal resistance of the MFC stack, CS-1. (c) MFCs connected to the loads individually, matching their individual internal resistances, CS-2; and (d) connected to MPPTs individually which are then connected in series, CS-3.

CS-2: t-MFC stack was connected to a stack of the constant electrical loads of 50 Ω ('snap shot' maximum power point load) which created bridging between the junction of neighbouring MFCs to the junction of their loads as shown in Figure 5.1c. The voltage drop across the loads and stack voltages were sampled at sampling rate of 2 samples per minute using a PC equipped with LabVIEW™ and NI USB-6218 (National Instruments™).

CS-3: In this case study as shown in Figure 5.1d, the stack of the electrical loads as in CS-2 was replaced by a stack of the digital potentiometers (Intersil® X9C102, Farnell UK Ltd., Leeds). Each potentiometers were controlled by an independent MPPT (as described in section 3.2.2) controllers but an additional logic statement was introduced where the controller would increase the electrical loading (in steps) *if* (conditional statement) the voltage from individual MFC that the potentiometer is connected to, would fall below 0.1 V. Here, NI USB-6218 (National Instruments™) was used for voltage measurements and load actuations (following MPPT) and; sampling of voltage and actuation of load was carried out at intervals of 150 s.

During each sets of case studies, t-MFC1, t-MFC2 and t-MFC3 were fed (in batch mode) with sodium acetate as substrate with concentration of 2.0 mM, 0.5 mM and 2.0 mM, respectively to stimulate the substrate imbalance which is likely to occur in the treatment of wastewater stream using continuous hydraulically series stack of MFCs. Substrate was provided with media as described in section 3.2.1.

5.2.3 Effect of prolonged voltage reversal on anodic biofilm

***Control*:** To look at variations in voltage generation from t-MFCs due to different substrate concentrations, t-MFC1, t-MFC2 and t-MFC3 were fed (in batch) with 0.5 mM, 0.5 mM and 2.0 mM sodium acetate, respectively and each of the t-MFCs were connected to static loads of 70 Ω independently. Static load of 70 Ω was chosen due to a shift (from 50 Ω to 70 Ω) in maximum power point load was observed before performing this experiment. The substrate was allowed to deplete and subsequent power production from t-MFCs was considered as a *control* for the experimentations performed for stack connectivity strategies.

To investigate the effect of voltage reversal on the anodic biofilm in t-MFC, they were fed (in batch) sodium acetate with same concentrations as in the *control* experiment and connected in series (electrically) as in CS-1 to a stack load of 210 Ω to match the overall internal impedance of the t-MFC stack. The stack operation was allowed to continue even after the voltage reversal, for 9 days. Liquid (anolyte) and anodic biofilm samples were taken from the t-MFC anodes when they were fed and when the substrate depletion was apparent from

the voltage measurements. 1 cm² sections of carbon veil anode was cut aseptically, to collect the biofilm sample for its ecology analysis.

5.3 Results and discussion

5.3.1 Power curves and rationale for selecting the values of static loads

As was the case in the experiment presented in Chapter 3, the maximum power point load (determined while the MFC was well fed and operating at 30 °C and atmospheric pressure) was adopted for the static loading of t-MFCs (for both independent and stack operation) in the study presented in this chapter. When considering the deployment of an MFC array for the wastewater treatment, varying the electrical load 'manually' to match maximum power from MFCs would be impractical and the MFCs, if operated under static load, would be operated by matching the peak power production conditions, as determined periodically. Variation in operational conditions such as pH, substrate concentration, flow rate and temperature, may change the internal resistance of MFCs and so also the external matched load for maximum power transference. It is therefore unlikely that the instantaneous loading conditions will be persistently ideal in such a loading regime. Therefore, operating MFCs under MPPT loading is likely to be beneficial. This instigation considers the situation where an MFC in a stack is receiving unequal substrate concentration compared to the other MFCs in the stack; while connected to a load that match the maximum power point under conditions that may no longer exist, i.e. well-fed condition. The maximum power point load described here, occurs at an ohmic load and associated current which coincide with the peak

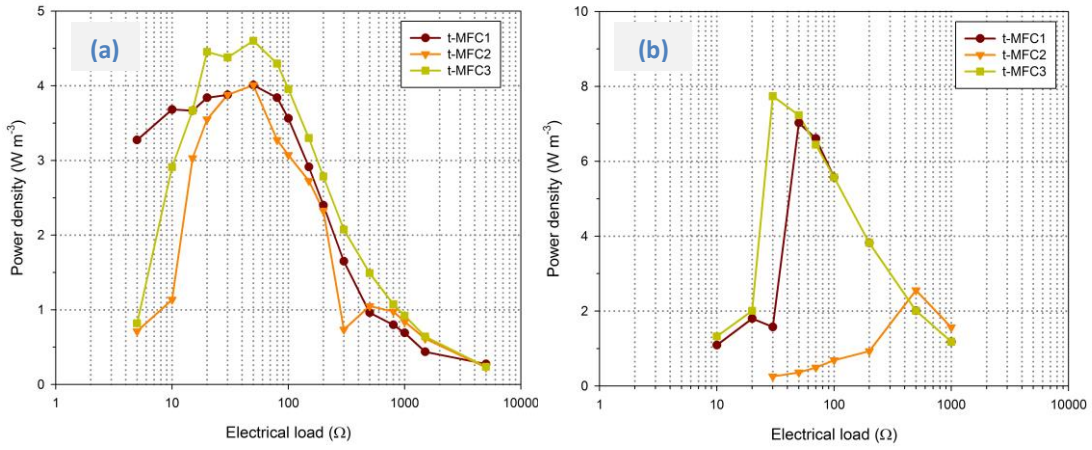

Figure 5.2: Power (normalised to the anode volume) from t-MFCs against the load, measured before beginning the sets of experiments (a) CS-1, CS-2 and CS-3 and (b) prolonged voltage reversal.

of the power curve (power vs. current or load). The load is therefore not determined very finely and changing the load slightly higher or lower may result in only small variation in the power, depending on the gradients that exist in the power curve over the current range.

Figure 5.2 shows measured power from t-MFCs prior to the reported set of experiments as in CS-1, CS-2 and CS-3; and also prior to the start of the investigation into prolonged voltage reversal as considered in section 5.2.2 and 5.2.3.

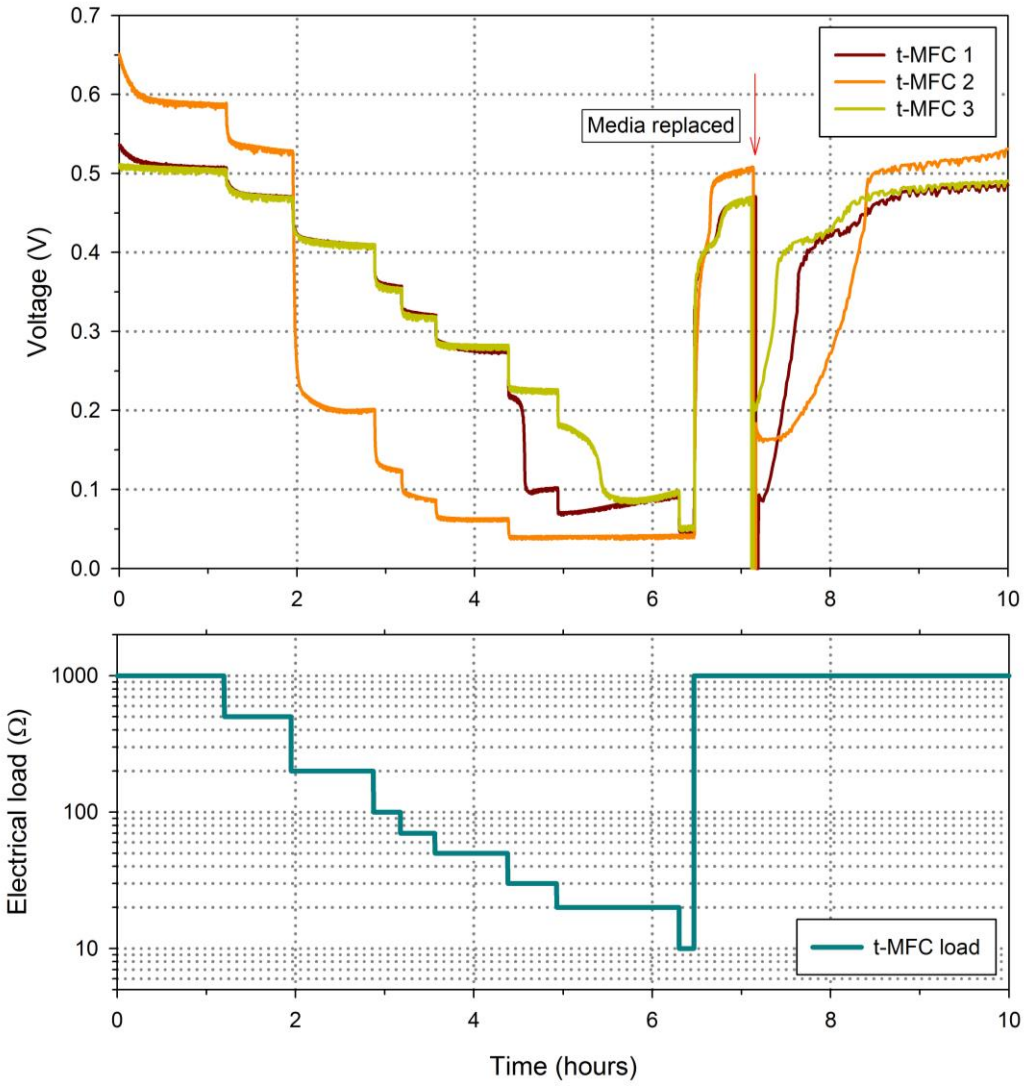

Figure 5.3: Voltage drop across the load connected to the t-MFCs when the loads were stepwise lowered as shown in electrical load plot for measurement of power before prolonged voltage reversal experiment. For t-MFC2, the load was not decreased beyond 30 Ω. The media in t-MFCs were replaced at approx. 7.2 hours as shown by the red arrow. Only 1 set of load values are shown in electrical load plot as they were identical (with 1% tolerance).

It can be seen from Figure 5.2a, that the power from t-MFC1, t-MFC2 and t-MFC3 peaked 4.0, 4.0 and 4.6 W m^{-3}, respectively (with respect to anode chamber volume), when connected to a 50 Ω load. When investigating cases CS-1 and CS-2, the same load value was used to maintain the maximum power loading for all t-MFCs. CS-1, CS-2 and CS-3 experiments were performed before investigating the prolonged effect of voltage reversal on the biofilm.

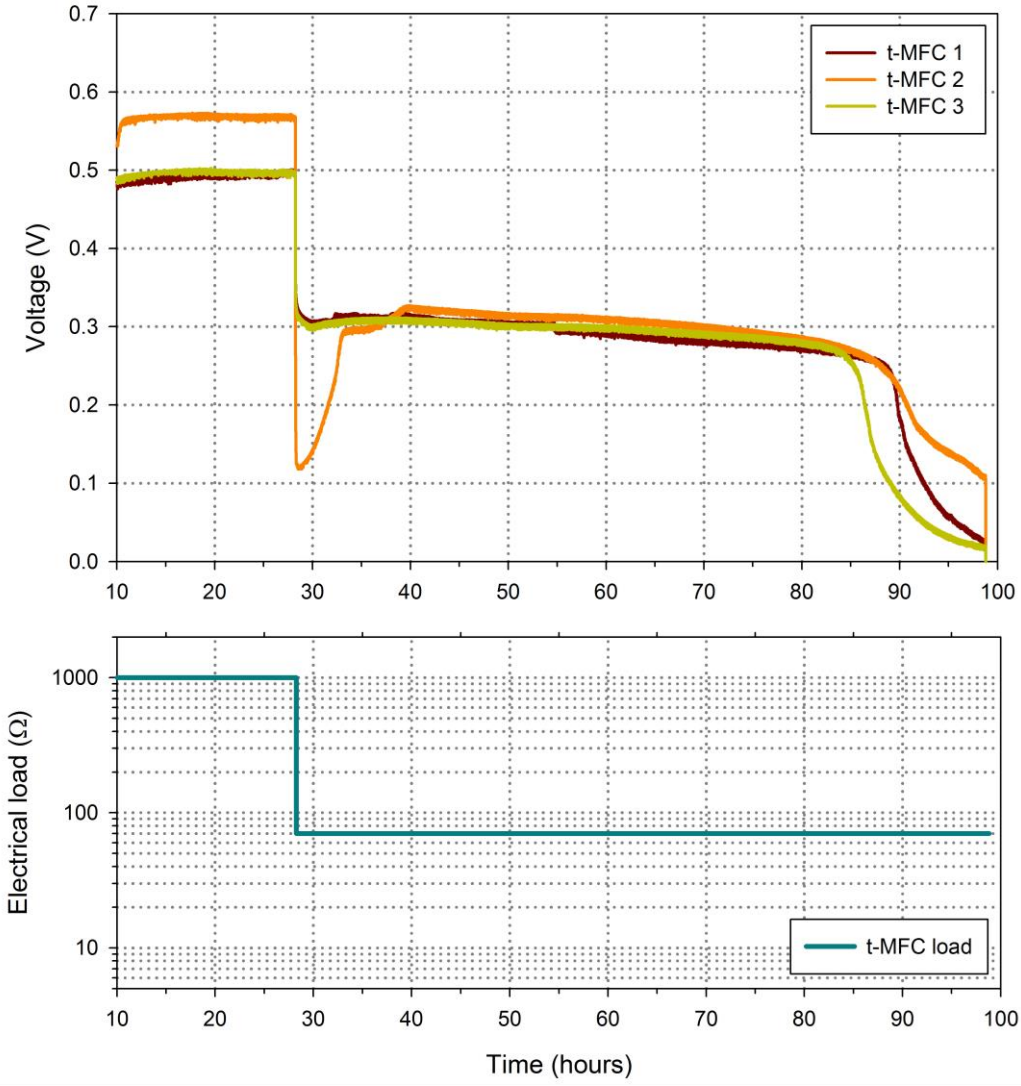

Figure 5.4: Voltage drop across the loads that were connected to t-MFCs after the power measurement (before the prolonged voltage reversal experiment). The plots show time span of hour 10 to hour 100, i.e. continued from Figure 5.3.

When the power curve was measured again at the start of the prolonged voltage reversal experiment, it was found that the power curves from all t-MFCs (Figure 5.2b) differed from that previously determined. The change could be due to the perturbations to which the MFCs were subjected in the previous set of experiments (CS-1, CS-2 and CS-3), which were highly transient. The t-MFCs were provided with fresh media (40 mM substrate) and each was

connected to a load of 1 kΩ for about 21 hours and then to 70 Ω, as shown in Figure 5.3 (up to hour 10) and Figure 5.4 (from hour 10 to hour 100).

It appears that the voltage generation from t-MFC2 was severely affected in the loading region between 200 Ω and 30 Ω, but not at higher loading than 500 Ω. When the load was switched from 1 kΩ to 70 Ω, t-MFC2 recovered voltage generation in 13 hours (between hour 27 and 40 as shown in Figure 5.4) and it matched with t-MFC1 and t-MFC2. MFCs used in this study are identical to the ones used in their study by Kim et al. (2009) and they produced peak power at loading of 70 ± 5 Ω which is evident from their power curve data in (Kim et al., 2009). Also, power from MFCs would typically peak at the voltage of 0.3 ± 0.05 V and any variation in impedance would result in a change in the current as demonstrated by Degrenne et al. (2011). For these reasons, a static load of 70 Ω was selected for the experiments to investigate the effect of prolonged voltage reversal as in section 5.2.3, which is different from the maximum loading determined from the power curve in Figure 5.2b. However it represents near maximum power from t-MFCs, as supported by the temporal voltage measurement after the recovery of t-MFC2 (hour 40 to hour 60 in Figure 5.4).

5.3.2 Voltage reversal in t-MFC stack

Figure 5.5 shows the temporal voltage drop across the electrical loads of 70 Ω that were connected to t-MFCs when the t-MFC1, t-MFC2 and t-MFC3 were fed with 0.5, 0.5 and

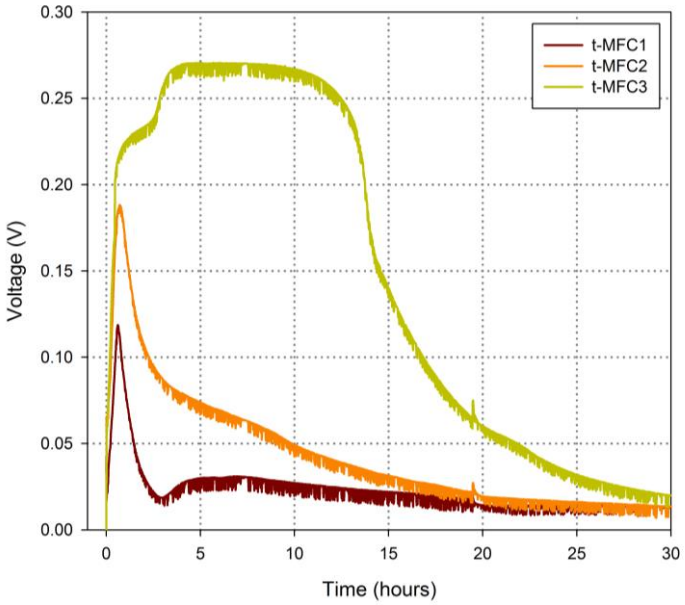

Figure 5.5: Voltage drop across 70 Ω loads that were connected to t-MFCs which were electrically independent, as a control with t-MFC1, t-MFC2 and t-MFC3 fed with 0.5 mM, 0.5 mM and 2.0 mM Sodium acetate respectively.

2.0 mM of sodium acetate, respectively. Voltage from t-MFCs rapidly increased when the substrate was added but due to limited substrate availability in t-MFC1 and t-MFC2, the voltage started decaying while the voltage from t-MFC3 continued to reach a plateau (steady-state level of voltage) and decayed when the substrate depletion was apparent. This demonstrates that the difference in substrate concentration (0.5 mM vs. 2.0 mM) is sufficiently high enough to induce substrate imbalance and the subsequent voltage generation which is believed to be one of the primary cause of occurrence of voltage reversal in MFCs (Oh and Logan, 2007).

According to CS-1, when t-MFC1, t-MFC2 and t-MFC3 were fed with substrate concentration of 2.0, 0.5 and 2.0 mM, respectively and connected electrically in series; t-MFC3 showed stable voltage generation within 5 hours but t-MFC2 and t-MFC1 showed voltage reversed out of which t-MFC1 seemed to be recovering after 12 hours and that could be attributed to the slower start-up of t-MFC1 (Figure 5.6a). t-MFC2 being unable to generate voltage when fed with lower substrate concentration, was severely affected and the cell voltage reached -0.7 V by the hour 26 and overall stack voltage drop across the 150 Ω remained below 0.1 V throughout the 26 hour period.

Similarly, when t-MFC1 and t-MFC2 were fed with lower concentration of sodium acetate (0.5 mM) compared to t-MFC3 (2.0 mM) during the prolonged voltage reversal experiment, the overall stack voltage across the 210 Ω load was also below 0.12 V throughout the period of 9 days except for a spike that appeared at 100 hours (lasted only 1 sample duration). The t-MFC stack was left in the reversed voltage condition for sufficient time (9 days) to allow the biofilm to express any changes, if happens, due to the voltage reversal. The trajectory of temporal voltage development from t-MFC1 could be observed and seen to correlate (reflect) with that of the collective voltage response from t-MFC2 and t-MFC3 (Figure 5.6b). This voltage reversal phenomenon exhibited by t-MFCs electrically connected in series in the stack is in agreement with the studies by others (Aelterman et al., 2006, Oh and Logan, 2007) and it forms a significant barrier in the stack operation of MFCs.

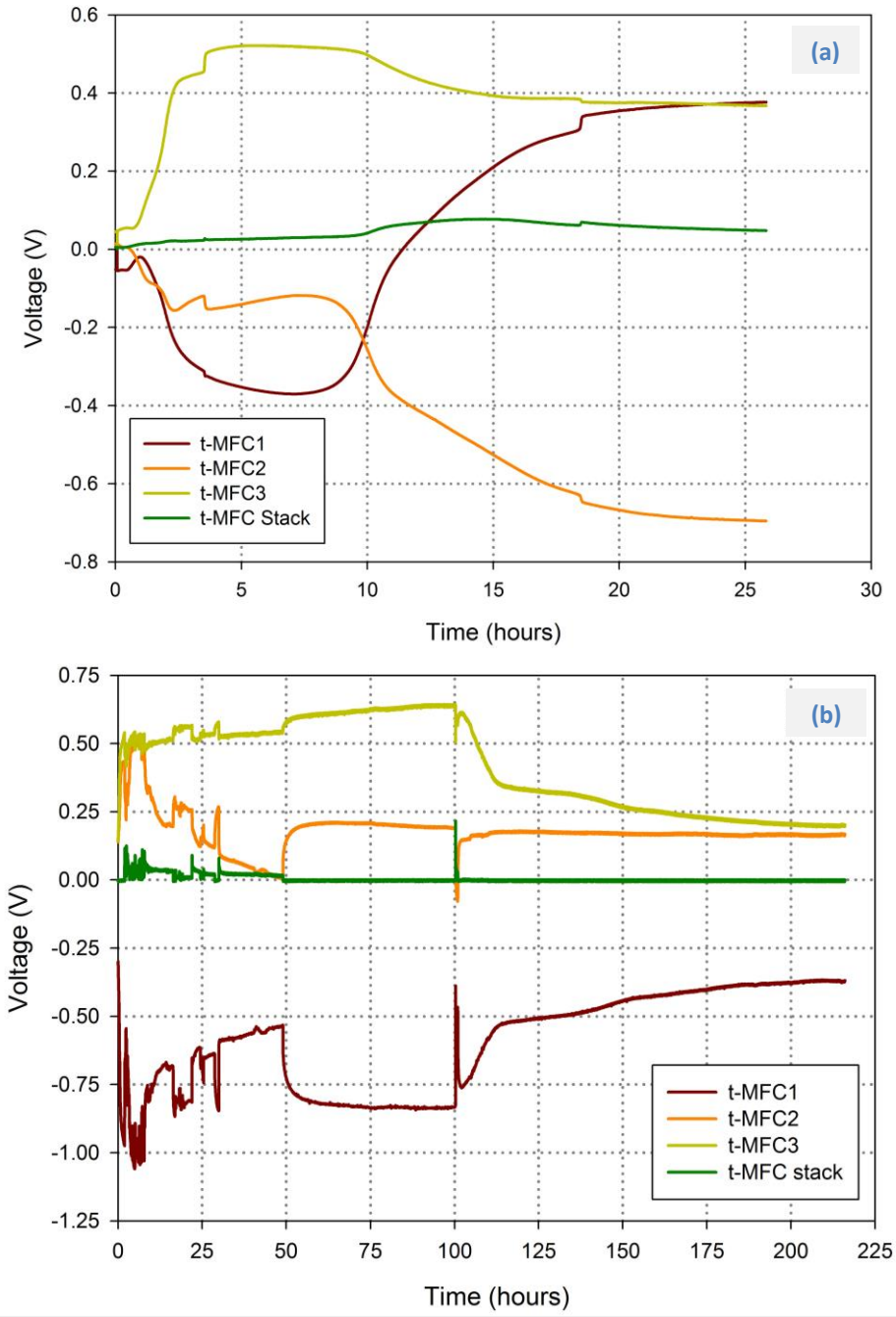

Figure 5.6: Voltages across t-MFCs and voltage drop across an the stack load (static) of (a) 150 Ω as in CS-1 with t-MFC1, t-MFC2 and t-MFC3 fed with 2.0, 0.5 and 2.0 mM of sodium acetate, respectively and (b) 210 Ω for prolonged voltage reversal experiment with t-MFC1, t-MFC2 and t-MFC3 fed with 0.5, 0.5 and 2.0 mM of sodium acetate, respectively; when connected in series.

5.3.2.1 The MFC polarity reversal

The cell reversal in MFCs was first reported by Aelterman et al. (2006) and investigated further to find causes for the occurrence of voltage reversal by Oh and Logan (2007) but did not provide the mechanism of voltage reversal in the MFC stack. Greenman et al. (2011) have attempted to describe the voltage reversal phenomenon by using hydraulics as an analogy but here, the voltage reversal (MFC polarity reversal) can be considered in the context of the t-MFCs and the case studies applied to them.

In Figure 5.1, the electrical connections to anodes and cathodes of t-MFC1, t-MFC2 and t-MFC3 are identified as An1, An2, An3 and Cath1, Cath2, Cath3, respectively. In CS-1 as shown in Figure 5.1b, when the t-MFC2 was fed with lower substrate concentration (0.5 mM) compared to other t-MFCs (2.0 mM), t-MFC2 will generate comparatively lower voltage as evident from Figure 5.5 which is the consequence of lower current being generated by An2. Since An2 is connected to Cat3, An2 will assume the voltage of Cat3. Due to lower current generation by An2, the proton generation will also be lower and therefore, cationic current flow from An2 to Cat2 in t-MFC2 will also be lower compared to cationic current in t-MFC1 and t-MFC3. So, Cat2 will be limited in its electronic current sinking capability and it will assume the potential of An1 to which it is connected. This will cause An2 being more positive than that of Cat2 and hence, the resultant will be reversal of voltages across An2 and Cat2.

In case of limited (or minimal) current generation by t-MFC2, the t-MFC2 will become a parasitic load for the stack, unable to transport the cations from its anode to cathode when required. So, the stack load will be lowered as a consequence and it is evident in Figure 5.6. Moreover, when electrical load of 70 Ω is applied to the t-MFC, it produces voltage across the load no more than 0.3 V (Figure 5.5) and voltage level of more than 0.4 V is produced when an electrical load of 1 kΩ or more is applied (Figure 5.3). Voltage level from t-MFC3 approaching 0.5 and 0.6 on occasionally with an overall stack current of < 0.6 mA, even when stack load of 150 Ω (Figure 5.6a) and 210 Ω (Figure 5.6b) is connected to the stack, implies that a higher than 150 Ω and 210 Ω load must be present in the circuit which is likely to be caused by t-MFC2 becoming a parasitic load.

This mechanism of voltage reversal is also applicable when no current is generated by the MFC as evidenced by the study of Oh and Logan (2007) who observed voltage reversal even when an abiotic (anode not populated by electrogens, i.e. a sterile MFC generating OCV of 0.0 V) was connected to the fully operational MFC.

5.3.3 Circumvention of voltage reversal

As per CS-2, when electrical load was distributed among the t-MFCs (Figure 5.1c) and t-MFC2 was provided with lower substrate concentration (0.5 mM) than that of t-MFC1 and t-MFC3, no voltage reversal was exhibited by any of the t-MFCs (Figure 5.7). Notably, t-MFC2

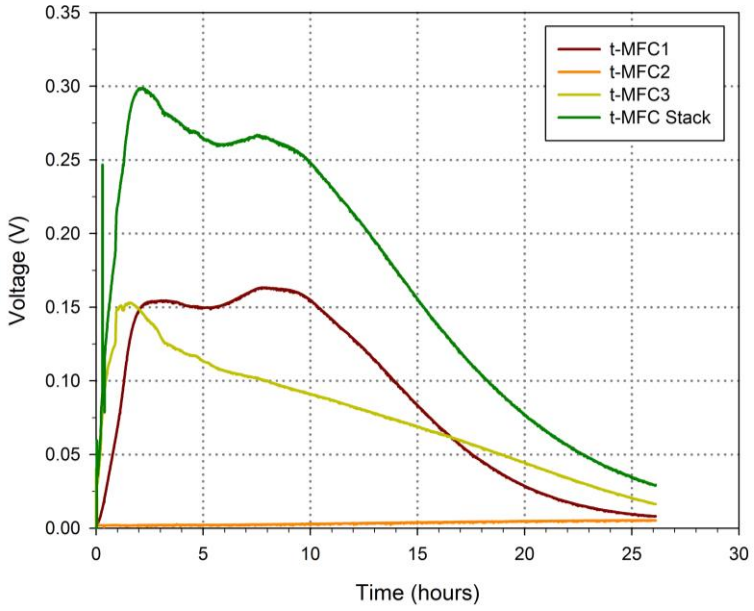

Figure 5.7: Voltage drop across static loads connected across t-MFCs and overall stack voltage as in CS-2.

was not able to start and the voltage across the stack was within 0.25 – 0.30 V for 8 hours after the start of current generation from t-MFCs and then started decaying which is apparent due to the substrate depletion.

In CS-3 shown in Figure 5.1d, when static loads as in CS-2 were replaced with the variable loads through MPPT controllers, again none of the t-MFCs exhibited voltage reversal. At the beginning of CS-3, the starting point of MPPT loads were selected to be 500 Ω. The MPPT controller was able to track the MPP from measures of voltage drop across each individual MPPT loads which is evident in Figure 5.8 whereby, the load value of 100 Ω – 140 Ω is applied between hour 12 till hour 27. All t-MFCs were able start within 2 hours of addition of substrates in their anodes and generated individual voltages between 0.3 V – 0.4 V during the period of hour 1 – 3, with an overall stack voltage of 1.1 V as evident from Figure 5.8. When the voltage level from t-MFCs started dropping below 0.1 V due to substrate depletion, the MPPT loads were increased gradually reaching maximum load values and can be seen from the load plot in Figure 5.8 (MPPT load on t-MFC3 started increasing after hour 27 but can be seen only up to hour 30 on the load plot).

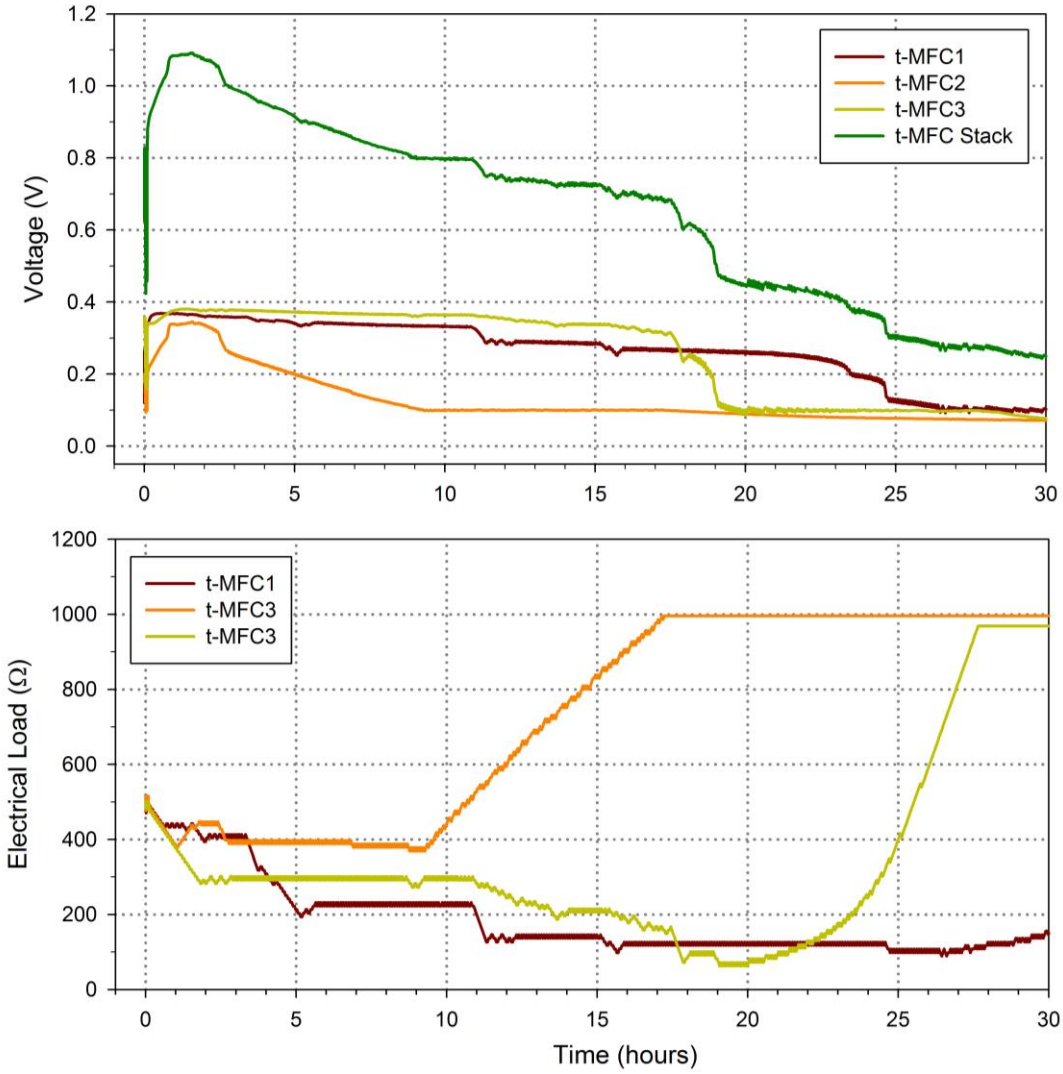

Figure 5.8: Voltage across MPPT loads connected to t-MFCs and the overall stack voltage as in CS-3.

In CS-2 and CS-3, the individual MFCs along with their individual loads are connected in series, creating bridging throughout the whole stack between the junction of anodes and cathodes and the junction of loads; of the neighbouring cells (Figure 5.1c-d). So, in the substrate limited conditions, when An2 stops generating electrons, the electrons required at the cathode of t-MFC3 can be sunk via the external load of t-MFC3 (generated by An3) and/or t-MFC2 (generated by An1). Similarly, when the cationic current is limited as a consequence of substrate limitation or lack of enough cations at the cathode of t-MFC2, the electrons generated by An1 can reach cathodes of t-MFC1 and t-MFC3 via external loads. In this way, the underperforming cells can be bypassed. This can be evidenced by Figure 5.7 and Figure 5.8 whereby, lower performance of t-MFC2 did not cause deterioration in t-MFC1 and t-MFC3's performances. Also, when t-MFC2 was operated at electrical load of 50 Ω (static), it was unable

to start (Figure 5.7) throughout the whole period of operation in CS-2. This suggests that the variable loads that are controlled by MPPT algorithm along with the hybrid connectivity of the MFC stack as demonstrated in this study could avoid the voltage reversal through bypassing the underperforming MFCs with minimal decline in the stack performance.

The experiments presented here were duplicated but only one set of results are presented for the clarity. However, similar trends were observable and same conclusions can be drawn from the duplicated results as presented in Ref. (Boghani et al., 2014).

When the strategies of MFC stack connectivity was applied on significantly different MFC in terms of the architecture, its anodic volume capacity (6.25 mL) and the type of substrate (human urine) as shown in the study by Boghani et al. (2014), similar trends were observable. Despite the differences in the MFCs (t-MFCs vs. small scale MFCs in their study), the strategy (CS-3) presented here was effective in circumventing the voltage reversal while operating MFCs at their peak power levels. This suggests that the strategy is transferable to significantly different types of MFCs.

5.3.4 Effect of voltage reversal on microbial ecology in the anode

It is known that the reversal of voltage in proton exchange membrane fuel cell (PEMFC) can cause damage to the catalyst and the electrodes (Liang et al., 2009, Taniguchi et al., 2004). Also, Oh et al. (2009) demonstrated that the voltage level of lower than 3 V was tolerable by the bacteria, but voltages of 3 V or higher can adversely affect the electrogens; inactivating the anode in MFC mainly due to high voltages rather than the oxygen generation from electrolysis of water in the anode. In their study (Oh et al., 2009), the application of voltage was for relatively short duration (1 hour) of time compared to the reversed condition studied by others (Aelterman et al., 2006, Boghani et al., 2014, Oh and Logan, 2007). In this study, performance of MFC (t-MFC2) after the voltage reversal was seen to have adversely affected. Therefore, to see if the affected performance of t-MFC2 due to voltage reversal from relatively lower level of voltage (0.7 V) was expressed by the electrogenic community at the anode, molecular analysis[‡] was performed as published in the paper by Boghani et al. (2014). It showed that the biofilm from anodes of all t-MFCs were 90 % similar before the prolonged voltage reversal experiment but after the voltage reversal (9 days of prolonged voltage reversal), the biofilm from anode of t-MFC2 was only 83.3 % similar to that of the other anodes

[‡] Molecular analysis was carried out by Dr. Iain Michie at the laboratory of Sustainable Environment Research Centre (SERC) of University of South Wales and the detailed methodology is presented in BOGHANI, H. C., PAPAHARALABOS, G., MICHIE, I., FRADLER, K. R., DINSDALE, R. M., GUWY, A. J., IEROPOULOS, I., GREENMAN, J. & PREMIER, G. C. 2014. Controlling for peak power extraction from microbial fuel cells can increase stack voltage and avoid cell reversal. *Journal of Power Sources,* 269**,** 363-369.

(Boghani et al., 2014). Lyon et al. (2010) demonstrated that the application of different level of electrical loads can be reflected on microbial ecology but the power performance was not affected. Here, in this study, it is possible that the prolonged voltage reversal may have been reflected in change in anodic microbial community but the performance was able to recover meaning that the electrogenic biofilm may not have permanently damaged due to the voltage reversal.

It is possible to avoid voltage reversal during the stack operation of MFCs by connecting them in hybrid connectivity as presented in this study and extract the maximum power available from the MFC stack using MPPT strategies as presented by the study in this chapter. MPPTs could be implemented through low power digital electronics. This will be useful in the energy recovery from wastewaters via stack operation of an array of MFC at large scale. However, usability of stack voltages generated while using the strategy (CS-3) presented here, should to be explored further to assess whether it would be possible to use the overall stack voltage for loading rather than utilising the current through distributed loading across the stack.

6. Optimisation of the helical anode for improvement in power production

6.1 Introduction

Anode is the electron generator of MFC where electrogens generate electrons from the degradation of wastewater. An increase in the number of such active electrogens per unit volume, or area would imply an increase in the production of electrons and therefore, the power. An helical anode could offer greater projected surface area than an anode in an annular flow path. For example, the projected surface area of the helical electrode presented in this study is approximately 3 times that of the projected surface area provided by an electrode of 15 mm diameter with an equivalent axial length, analogous to that presented in Ref. (Kim et al., 2011a).

The helical path forces simultaneous rotation and precession creating shear and mixing in the fluid. This could be beneficial for bioelectrochemical systems where the fluid needs to promote mass transfer throughout the anode compartment to avoid localised pH decrease near the vicinity of the biofilm and to maintain the pH level close to 7 (with appropriate buffering considered) to avoid inhibition of the electrogens. When helical fluid channels are considered, the fluid flow and associated mixing is affected by several geometrical factors such as the size and shape of helical channel, pitch, diameter of the helical path, topology and surface behaviour.

This chapter reports the analyses conducted on a helical anodic chamber electrode configuration in MFCs and investigates the possibilities of enhancements in power performance from MFCs through the induced mixing of the anolyte in the anode chamber. An optimal configuration is sought for a proposed helical geometry and the effect of placing flow disruptors in the fluid path to enhance passive mixing of the fluid is investigated. Modeling of the fluid flow and the mass transport of diluted species caused thereby uses the modeling and simulation platform COMSOL Multiphysics®. An experimental study is also performed on the proposed designs of the helical anode for validation and further investigation of the power enhancement. As a result, an optimised helical anode design is recommended that could perform as well as the best performing anode studied experimentally at a lower input energy expense (in terms of fluid pumping).

6.2 Materials and methods

6.2.1 Multiphysics modeling

6.2.1.1 Model set-up

The following were modelled in COMSOL Multiphysics® to study the fluid dynamics and the mixing caused by the fluid flow in anode when a given anode geometry is considered. Three simulation studies were performed viz. SIM-1, SIM-2 and SIM-3, progressively investigating the mixing induced by helical and interrupted flow channels:

1. **SIM-1:** An helical fluid channel with 20 mm width, 9 mm inner diameter, 46 mm outer diameter and pitch of 25 mm. Fluid flow and mass transport of diluted chemical species was considered in this geometry to show concentration distribution and mixing of the fluid when flowing in helical path (Figure 6.1a).
2. **SIM-2:** A multiple straight fluid channels of width 20 mm with shared porous walls of 5 mm thickness was considered out of which, a small section of one fluid channel of length 50 mm with symmetrically cut porous anode (2.5 mm) on both side of the fluid channel with (a) no obstructions to the fluid in straight fluid channel (SFC); (b) 1.5 mm × 1.5 mm cross-section pillars placed at 5 mm intervals in straight fluid channel (P-SFC) and (c) converging plates (1.5 mm × 5 mm cross section at 30° to longitudinal direction of the tube) placed at 7 mm intervals in straight fluid channel (CP-SFC) were considered for the models (Figure 6.1b-d). Fluid flow and transport of chemical species was modelled along with complete degradation of acetate in the porous channels.
3. **SIM-3:** An helical geometry with 5 mm wide anode and 20 mm wide fluid channel was considered out of which a ¼-turn helical fluid channel with symmetrically cut porous anode (2.5 mm wide) on both sides of fluid channel which contained; (a) no obstructions helical fluid channel (HFC); (b) pillars (28 pillars per revolution, each with 1.5 mm cross-section) in helical fluid channel (P-HFC) and; (c) converging plates (16 sets of plates per revolution, each set containing 1.5 mm wide plates, forward and backward helical with pitch of 25 mm per revolution) in helical fluid channel (CP-HFC) as shown in Figure 6.1e-g.

The following equations were used in all of the above mentioned simulations (SIM-1, SIM-2 and SIM-3) to simulate the fluid flow and the associated mass transport. Additionally, in porous medium, degradation of acetate into protons was considered.

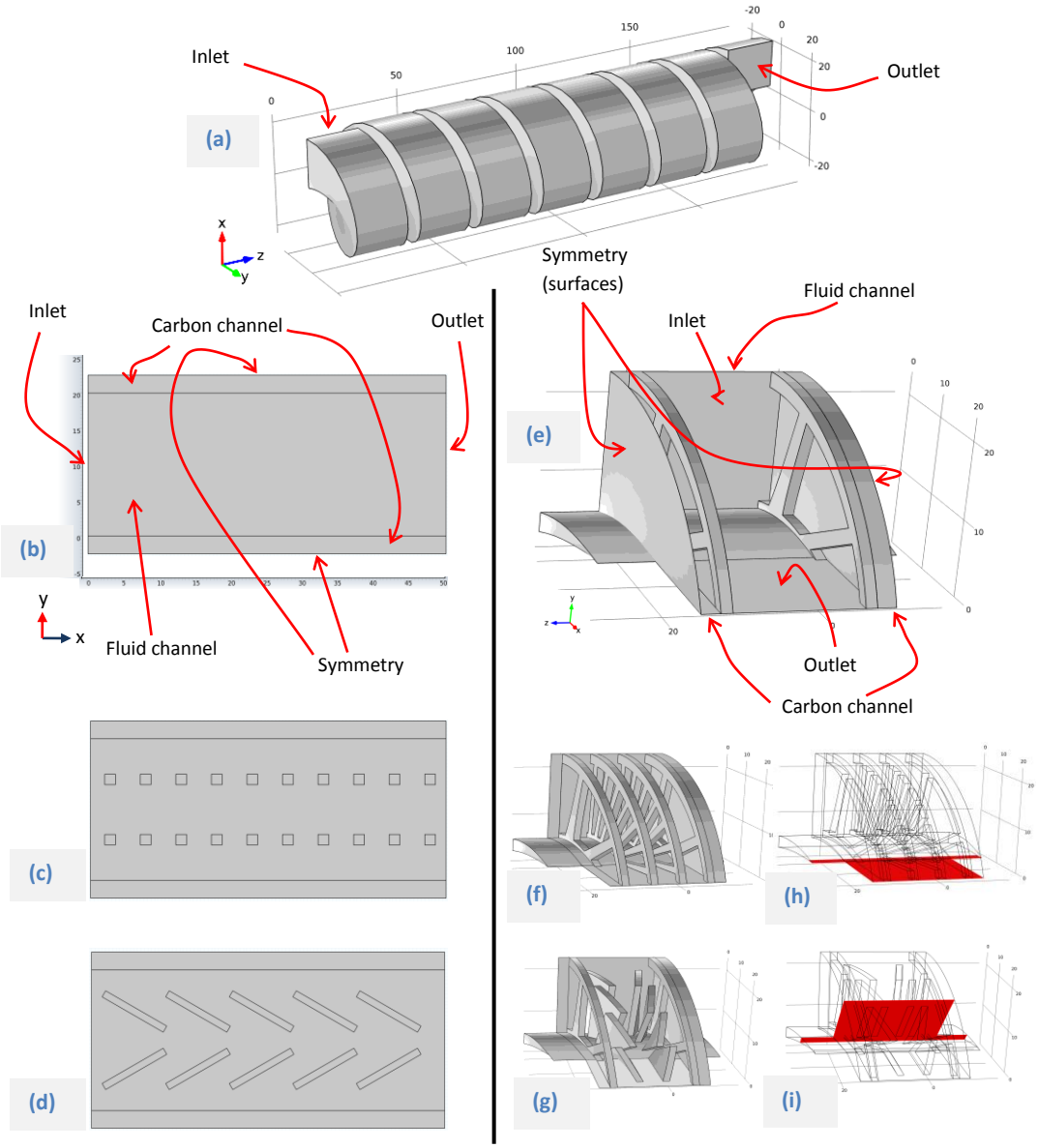

Figure 6.1: Typical boundary conditions and the geometries used in the CFD and mass transport simulations for (a) helical fluid channel; small section of 50 mm long pipe section with porous carbon wall and (b) straight fluid channel (SFC), (c) pillars in straight fluid channel (P-SFC), (d) converging plates in straight fluid channel (CP-SFC); and for helical carbon electrodes with (e) helical fluid channel (HFC), (f) pillars in helical fluid channel (P-HFC) and (g) converging plates in helical fluid channel (CP-HFC). A cut-plane on xz plane is shown in (h) and a cut-plane 45° inclined to yz and xz and passing through z axis shown in (i) used to plot the results in 2D. Numbers shown on the grid are in mm.

⇒ Fluid flow in free and porous medium (Stokes-Brinkmann equations)

$$\frac{\rho}{\varepsilon_p}\left(\mathbf{u}\cdot\nabla\frac{\mathbf{u}}{\varepsilon_p}\right)=\nabla\cdot\left[-p\mathbf{I}+\frac{\mu}{\varepsilon_p}(\nabla\mathbf{u}+(\nabla\mathbf{u})^T)-\frac{2\mu}{3\varepsilon_p}(\nabla\cdot\mathbf{u})\mathbf{I}\right]-\frac{\mu}{K_{br}}\mathbf{u} \qquad \textit{Eq. 6.1}$$

$$\rho\nabla\cdot\mathbf{u}=0 \qquad \textit{Eq. 6.2}$$

⇒ Mass transport of diluted chemical species (Fick's law for diffusive term)

$$\nabla \cdot \left(-D_j \nabla c_j\right) + \mathbf{u} \cdot \nabla c_j = R_j \qquad \textit{Eq. 6.3}$$

$$\mathbf{N}_j = -D_j \nabla c_j + \mathbf{u} c_j \qquad \textit{Eq. 6.4}$$

Where; the nomenclatures used in Eq. 6.1 to 6.4 are as presented in Table 6.1. For the fluid flow in free medium (fluid channel), the terms $\frac{2\mu}{3\varepsilon_p}(\nabla \cdot \mathbf{u})\mathbf{I}$ and $\frac{\mu}{K_{br}}\mathbf{u}$ from eq. 6.1 were not included and ε_p was set to 1; which formed Navier-Stokes equations for incompressible flow. Fluid flow and mass transport physics were coupled using the velocity field, $\mathbf{u}$. Pressure (p) and velocity ($\mathbf{u}$) continuity was assumed for the fluid flow at the interface of porous and free medium (Le Bars and Worster, 2006). Concentration of reactants and products in the mass transport of diluted species were considered in mass transfer physics using monod-type kinetics as used in the study by Kim et al. (2010):

$$R_{ac}^{e} = \frac{R_{ac,max}^{e} \cdot c_{ac}}{K_{ac}^{e} + c_{ac}} \qquad \textit{Eq. 6.5}$$

Where; according to the oxidation reaction of acetate (Du et al., 2007, Clauwaert et al., 2007),

$$CH_3COO^- + H_2O \rightarrow 2CO_2 + 7H^+ + 8e^- \qquad \textit{Eq. 6.6}$$

7 moles of protons (H^+) was assumed to be produced from complete oxidation of 1 mole of acetate (CH_3COO^-).

To quantify the mixing effect resulting from all designs presented in SIM-1 and SIM-2, the ratio of variance of concentration (acetate) at outlet to the inlet, known as mixing ratio (Hobbs and Muzzio, 1997) was evaluated as:

$$S_{outlet} = \frac{\sum_{i=1}^{n}\left(c_{ac_i} - c_{ac_{mean}}\right)^2 \; at \; outlet}{\sum_{i=1}^{n}\left(c_{ac_i} - c_{ac_{mean}}\right)^2 \; at \; inlet} \qquad \textit{Eq. 6.7}$$

Table 6.1: Nomenclature of the symbols in Eq. 6.1 – Eq. 6.7

Symbols	Description	Value	Unit
$\boldsymbol{\rho}$	Density of the fluid	992.62 (water at STP)	kg m^{-3}
$\mathbf{u}$	Velocity vector	Derived	m s^{-1}
$\boldsymbol{\nabla}$	Vector differential operator, $\frac{\partial}{\partial x}\hat{x} + \frac{\partial}{\partial y}\hat{y} + \frac{\partial}{\partial z}\hat{z}$ in three-	-	-

Symbols	Description	Value	Unit
	dimensional Cartesian coordinate system.		
$\boldsymbol{p}$	Pressure	Derived	Pa
$\mathbf{I}$	Identity matrix	-	-
$\boldsymbol{\mu}$	Dynamic viscosity	1.0093×10^{-3} (water at STP)	kg m^{-1} s^{-1}
$\boldsymbol{T}$	Transpose	-	-
$\boldsymbol{\varepsilon_{\mathrm{p}}}$	Porosity, the ratio of void volume to the total volume	0.72 assumed based on porous carbon (Kim et al., 2012)	Dimensionless
$\boldsymbol{K_{\mathrm{br}}}$	Permeability of the porous medium, carbon	1×10^{-12} (Gostick et al., 2006)	m^2
$\boldsymbol{j}$	Chemical species, acetate (ac) or proton (H^+)	-	-
$\boldsymbol{D_j}$	Diffusion coefficient for the species *j*	$D_{ac} = 1.09 \times 10^{-9}$ (Kato Marcus et al., 2007) $D_{H^+} = 9.03 \times 10^{-9}$ (Boero et al., 2005)	m^2 s^{-1}
$\boldsymbol{c_j}$	Concentration of the species *j*	Derived based on boundary conditions and reaction rates	mol m^{-3}
$\boldsymbol{R_j}$	Reaction rate expression for the chemical species *j*	In porous carbon channel; $\boldsymbol{R_{H^+}} = 7 \cdot \frac{R^e_{ac,max} \cdot c_{ac}}{K^e_{ac} + c_{ac}}$ And $\boldsymbol{R_{ac}} = -1 \cdot \frac{R^e_{ac,max} \cdot c_{ac}}{K^e_{ac} + c_{ac}}$	mol m^{-3} s^{-1}
$\mathbf{N}_j$	Concentration flux into or out of the surrounding environment	Derived	mol m^{-2} s^{-1}
$\boldsymbol{R^e_{ac,max}}$	Volumetric consumption rate of	1.65×10^{-5} (Kim et	mol m^{-3} s^{-1}

Symbols	Description	Value	Unit
	acetate by electrogens	al., 2011a)	
K_{ac}^{e}	Half-saturation constant of acetate degradation into electrons	0.27 (Kim et al., 2011a)	mol m^{-3}
c_{ac}	Concentration of acetate	At inlet; $c_{ac} = 40$ when, **SIM-1:** $0 < z \leq 10$ **SIM-2:** $0 < y \leq 20$ **SIM-3:** $0 < z \leq -20$ and $c_{ac} = 0$ when, **SIM-1:** $10 < z \leq 20$ **SIM-2:** $-2.5 < y \leq 0$; $20 < y \leq 22.5$ **SIM-3:** $2.5 < z \leq 0$; $-20 < z \leq -22.5$	mol m^{-3}
c_{H^+}	Concentration of H^+	Derived	mol m^{-3}
S_{outlet}	Mixing ratio	Derived	Dimensionless

6.2.1.2 Assumptions and considerations

Some assumptions were made in establishing the simulation of the models for SIM-1, SIM-2 and SIM-3 which are as below:

⇒ To show the mixing effect caused by the helical path, only the helical fluid channel was considered and no carbon channel or pillared former was considered in SIM-1; and therefore no acetate degradation was considered. Only the mass transport of acetate due to convection and diffusion was considered.

⇒ As per SIM-2, multiple straight fluid channels were assumed to be parallel to each other as if the helical anode was stretched open from its longitudinal direction into a flat electrode. Only a small section (of 50 mm long) from one of these parallel fluid channels sharing a porous wall was considered in simplified 2-dimensional (2D) simulations. The symmetry was assumed through the middle of the electrodes (Figure 6.1b). Porous electrodes shown in Figure 6.1b-d on each side of the fluid channel are already halves (symmetrical).

- ⇒ Helical fluid channel was simplified into ¼-turn geometry with helical fluid channel in the middle and symmetrical porous helical anode on both sides of the fluid channel. The symmetry was assumed to be at the surfaces of porous carbon electrode as shown in the Figure 6.1e. Porous electrodes shown in Figure 6.1e-g on each side of the fluid channel are already halves (symmetrical).
- ⇒ Incompressible fluid flow and mass transport were the only physics considered in anode. 'Migration of charged chemical species in electric field' was not considered in the mass transport physics as the convective and diffusive flux is believed to be dominant compared to the migration flux of ions due to the electric field provided by *circa* 0.3 V across the anode and cathode when considering maximum power production by MFCs (Degrenne et al., 2011). Inclusion of the 'migration of charged chemical species in electric field' could increase the unnecessary complexity and the model could become computationally expensive and exclusion of this physics would not affect the comparative study presented here and the conclusions drawn.
- ⇒ Fluid flow was believed to be laminar as Reynolds number was calculated to be 88.6 considering an equivalent hydraulic diameter of 18.9 mm of helical fluid channel and flow rate of 5×10^{-7} m^3 s^{-1} (30 mL min^{-1}).
- ⇒ Porosity of carbon was considered to be 0.72 (Kim et al., 2012) and uniform throughout. Carbon cloth is a woven fabric containing micro-sized fibres. When they are densely packed, they can be considered similar to carbon fibre paper in terms of its density and that could be assumed to have porosity of 0.78 as reported in the literature (Huang et al., 2011). However, this difference in porosity value had minimal effect on the fluid flow and mass transport of diluted species and conclusions drawn for the comparative study was not affected.
- ⇒ Electrogens were considered to be homogeneously present throughout porous carbon anode and no non-electrogenic activity was considered.
- ⇒ Isotropic properties of water were considered for the fluid flow in all of the simulations and it was assumed that the addition of substrate and phosphate based chemicals for buffering, would not have appreciable change in the density and dynamic viscosity.
- ⇒ All chemical species in simulations were considered to be diluted as they (solute) were present in far lower quantity than of the solvent, such that 40 mol m^{-3} of acetate in water is 2.36 g of acetate in 1000 g of water, resulting in 0.236% solute compared to the solvent (water).

⇒ At the inlet, the boundary conditions were set to provide an evenly distributed inflow of water across the flow channel, at a flow rate of 1 mL min^{-1} (1.67×10^{-8} m^3 s^{-1}), 3 mL min^{-1} (5.00×10^{-8} m^3 s^{-1}) and 8 mL min^{-1} (1.33×10^{-7} m^3 s^{-1}) and concentration of acetate as shown in Table 6.1 and; at the outlet, boundary conditions were set to exit at pressure of 0 Pa. Outflow of the chemical species were considered to be dominated by convection due to the fluid flow and the concentration gradient at the outlet surface, in the direction of the flow would be very small and therefore; the diffusive component at the outlet was ignored, i.e. $-\boldsymbol{n} \cdot D_i \nabla c_i = 0$; where, $\boldsymbol{n}$ stands for normal vector.

⇒ A 2D plane parallel to *xz*-plane was considered as shown in Figure 6.1h, to plot the H^+ concentration and H^+ concentration flux at the outlet of helical anode geometry, and; a plane at an intermediate location (45° inclined to *yz* and *xz* and passing through *z* axis) as shown in Figure 6.1i was considered to plot the pressure generated by fluid flow; to compare between the three designs of the helical fluid channel.

⇒ H^+ present in the water cannot exist as an ion and it forms an ionic bond with either a positively charged ion or with water (H_2O) molecule. The modeling results showing the concentration of H^+ is notional here and is presented for the comparative study of the anode designs.

6.2.1.3 Model computation

Fluid flow and mass transport of diluted species was solved in all models using finite element method (FEM) with linear discretisation. Triangular and tetrahedral type elements were used to mesh the geometry in SIM-2 and; SIM-1 and SIM-3, respectively. The mesh element sizes were 0.184 mm, 0.1 mm, 0.0938 mm minimum element size and 1.7 mm, 0.7mm, 0.868 mm maximum element size for SIM-1, SIM-2 and SIM-3, respectively.

An iterative solver of Generalised minimal residual method (GMRES) was employed for fluid flow and also for the mass transport of diluted species. The model was solved for fluid flow first and the solution was stored. Fluid velocity was then used to solve for the mass transport physics.

6.2.2 Experimental study

6.2.2.1 Anode designs and fabrication

An helical anode former was designed with helical channels of width 5 mm for carbon cloth as an electrode and 20 mm wide for the fluid channel, with inner diameter of 9 mm and

outer diameter of 46 mm and helical pitch of 25 mm per revolution with total of 7.22 revolution. The helical strands were 1.5 mm wide and were supported by spokes at 45° apart to support carbon electrode and also provide structural rigidity and sturdiness (Figure 6.2a). The former was closed with an orifice plate at the end, to provide structural rigidity and also to maintain virtually distinct fluid compartments when multiple anodes would need to be connected hydraulically in series. At the front of the anode former, a small cylindrical chamber was placed to locate the soldered joint of the current collector and it was drilled with 3 circularly equispaced holes (M3 × 0.75) for screws that would slide into the mating slots on orifice plate at the end of the former of subsequent anodes, when multiple modules connected together.

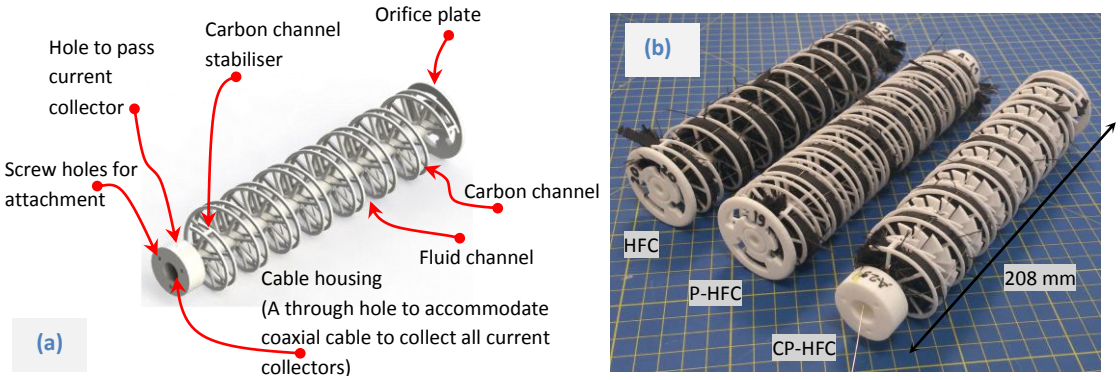

Figure 6.2: (a) CAD image illustrating a typical anode former with all functionalities highlighted and (b) Complete anodes with carbon cloth electrode and current collectors.

3-dimensional (3D) geometries of three different types of helical anode formers were created on SolidWorks® 2012 with difference in helical cannels, (a) helical fluid channel only, HFC, (b) pillared helical fluid channel, P-HFC and (c) converging plates in helical fluid channel, CP-HFC as previously mentioned in section 6.2.1. Pillars and converging plates are conceptualised to behave like static mixer and mix the fluid passively. In particular, the converging plates are designed to provide high shear rate near the carbon electrode wall, remove the substrate by creating pressure drop near the carbon channel wall and replenish with substrate rich fluid. These designs were produced by rapid prototyping using Dimension 3D 1200es printer (Dimension Inc., MN, USA) with the finished material to be acrylonitrile butadiene styrene (ABS) plastic.

Carbon cloth (CCP40, Fuel Cell Earth Inc., USA) was used for the anode electrode material as the resistance of a thin strip of 10 mm width; 0.3 mm thickness and 400 mm long carbon cloth and carbon veil (PRF Composites) was measured 2.7 Ω and 352.7 Ω and; 1.5 Ω

and 15.1 Ω when consolidated together on helical anode former (end to end), respectively. Carbon cloth was cut into 4-6 mm wide strips using scalpel and graduated rubber mat. They were laid on top of each other in the carbon channel of helical former. They were laid only in one direction to avoid any bulging that would be caused if laid in opposite direction. They were pressed gently during the process, to pack as many as carbon cloth strips as possible. The anode formers were weighed without and with carbon, to determine the amount of carbon loaded onto the anode. Six tinned-copper wires were passed, circularly equispaced, through the helical channels longitudinally on top of the stack of carbon cloth (Figure 6.2b). The tinned copper wire acted as the current collector and also restricted and consolidated carbon cloth strips in the helical channel. End to end resistance of completed helical channel of carbon cloth was measured to be 1.5 Ω and from current collector to the farthest carbon cloth strip, i.e. inner most layer was 0.9 Ω - 1.1 Ω.

6.2.2.2 Membrane electrode assembly (MEA)

Cation exchange membrane, CEM (CMI-7000S, Membrane International Inc., NJ, USA) was used mainly for the purpose of exchange of H^+ from anode to cathode during bioelectrochemical reactions but it also functioned as a containment of anolyte/wastewater. So, it was crucial to completely seal the anode chamber that does not allow fluid leakages towards the cathode, which would cause a parasitic current otherwise and lower the performance of MFC (Rismani-Yazdi et al., 2008). CEM was cut to size 230 mm × 170 mm, scored on its joining edges (membrane to membrane and membrane to the end caps) up to 10 mm from the edge of the CEM in diamond fashion using the utility knife to roughen the surface (Figure 6.3a). An adhesive (GLU & FIX leather adhesive, Bostik Limited, UK) was applied on joining surfaces and then CEM was rolled onto a 230 mm long mesh tube (RN 2530, Industrial Netting, MN, USA). This mesh tube was made from polypropylene and has open area of 41%. A firm pressure was applied by supporting the joint from outside with a lengthwise split identical mesh tube and cable ties. A 50 mm waste access plug (OsmaWeld, City Plumbing Supplies Ltd., UK) was used and joined at both ends of the tube to form a sealed compartment. Holes were drilled on the end caps to accommodate anode cable, fluid lines via barbed adapter (WZ-30704-02, Cole-Parmer, UK) and reference electrodes via 12 mm cable gland (1174601, Farnell, UK). This assembly was left to dry for at least 48 hours before handling and outer mesh tube was removed to put cathode in place.

The cathode was prepared as described by Cheng et al. (2006) on 210 mm × 160 mm plain carbon cloth (CCP40, Fuel Cell Earth LLC, MA, USA). On the air facing side, a

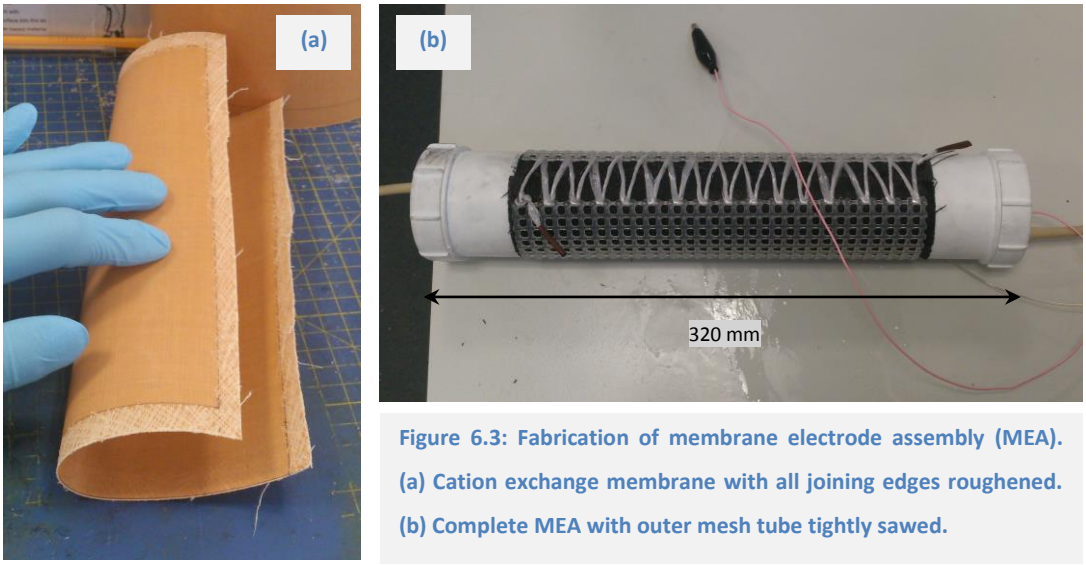

Figure 6.3: Fabrication of membrane electrode assembly (MEA). (a) Cation exchange membrane with all joining edges roughened. (b) Complete MEA with outer mesh tube tightly sawed.

paste made up of carbon black (Vulcan XC-72) and Polytetrafluoroethylene, PTFE (30% weight dispersion in water, SIGMA-ALDRICH®, UK) with 10 µL of PTFE per mg of carbon black was applied with 2.5 mg of carbon black per cm^2 of carbon cloth. The cloth was allowed to dry by natural convection in air for at least 2 hours and then heated at 370 °C in a pre-heated furnace for 30 minutes. The cloth was allowed to cool and then 60% PTFE was applied evenly on the carbon black layer with a varnish brush. After allowing it to dry (about 15 minutes), the cloth was again heated at 370 °C for 15 minutes. This resulted in a shiny black surface with plastic-like feel. This layer acts as diffusion layer, which allows the diffusion of oxygen into catalytic sites. The diffusion layer also prevents the catalyst from coming through the cloth. Handling is also made easier, particularly to connect the cathode terminal wire. On the membrane facing side, platinum catalyst with 0.5 mg cm^{-2} loading was applied. This was allowed to dry for at least 24 hours before the usage.

A thin layer of hydrogel (ECG Gel, CAMCARE, Cambridgeshire, UK) was evenly distributed on the CEM surface and the cathode was placed with catalyst layer facing the CEM as per the method developed by Kim et al. (2009). The split mesh tube was then put on top and sewn as shown in Figure 6.3b to maintain close contact of cathode to the CEM. A current collector was not used for the cathode; rather a crocodile clip connected directly to the cathode cloth. The resistance measured between the farthest end of the cathode (Two diagonal ends in a rectangle cathode cloth) was less than 3 Ω.

6.2.2.3 MFC start-up and operation

The anodes were inserted into the tubes formed by MEAs as shown in Figure 6.4 and the volume generated by the end caps were removed by placing polyfoam cores with a 10 mm hole drilled (for fluid to pass through) in it. The resulting volumes of MFCs with HFC, P-HFC and CP-HFC anodes were 350 mL, 355 mL and 310 mL, respectively, based on measured empty bed volume. A rubber stopper was inserted into the cable gland, in the absence of the reference electrode, which was only placed at the time of measurements requiring three-electrode system. All the MFCs were inoculated at the same time with 500 µm sieved activate sludge (Cog Moors Sewage Treatment Works, Cardiff, UK) in media as described in section 3.2.1 containing 40 mM sodium acetate solution at a ratio of 1:5. All MFCs were run independently, both hydraulically and electrically. However, the media was re-circulated through a common reservoir at flow a rate of 3 mL min^{-1} approx. during start-up and until the experimentation commenced. Maximum power point tracking (MPPT) loads as described before (Boghani et al., 2013) and in section 3.2.2 were connected to each MFCs. For each MPPT loads, 3 digital potentiometers (X9C102, Farnell, UK) were connected in parallel resulting typical load values of 17.8 Ω minimum, 484 Ω maximum and 4.75 Ω per step. The loads applied by MPPT were in the range of 17.8 Ω – 40 Ω during the start-up. The MFCs were run under well fed condition for up to 129 days before commencing further experimentation.

To investigate the effects of static mixers (pillars and converging plates) in helical fluid channels, the MFCs were run hydraulically independently with separate reservoirs of media as shown in Figure 6.4. The flow rate of the feed containing sodium acetate was varied from 1 mL min^{-1} to 9 mL min^{-1} while keeping organic loading rate (OLR) constant of 33.98 g L^{-1} day^{-1}. Feed was supplied by 2.97 inside diameter Marprene tubing (978.0279.000 and 902.0032.016, Watson-Marlow Pumps Group, UK) on a peristaltic pump (505u, Watson-Marlow Pumps Group) for each MFC fluid feed line (channel 1: HFC anode, channel 2: P-HFC anode and channel 3: CP-HFC anode). The feeding system was calibrated prior to the experimentation, and capacities are presented in Table 6.2.

Table 6.2: Flow rates available from each fluid lines connected to the MFC reactors.

Pump drive revolutions per min (RPM)	Flow rate in channel 1 (mL min^{-1})	Flow rate in channel 2 (mL min^{-1})	Flow rate in channel 2 (mL min^{-1})
8.25	1.20	1.02	1.17
23	3.51	2.97	3.38

Pump drive revolutions per min (RPM)	Flow rate in channel 1 (mL min^{-1})	Flow rate in channel 2 (mL min^{-1})	Flow rate in channel 2 (mL min^{-1})
48[§]	8.93	9.28	7.52

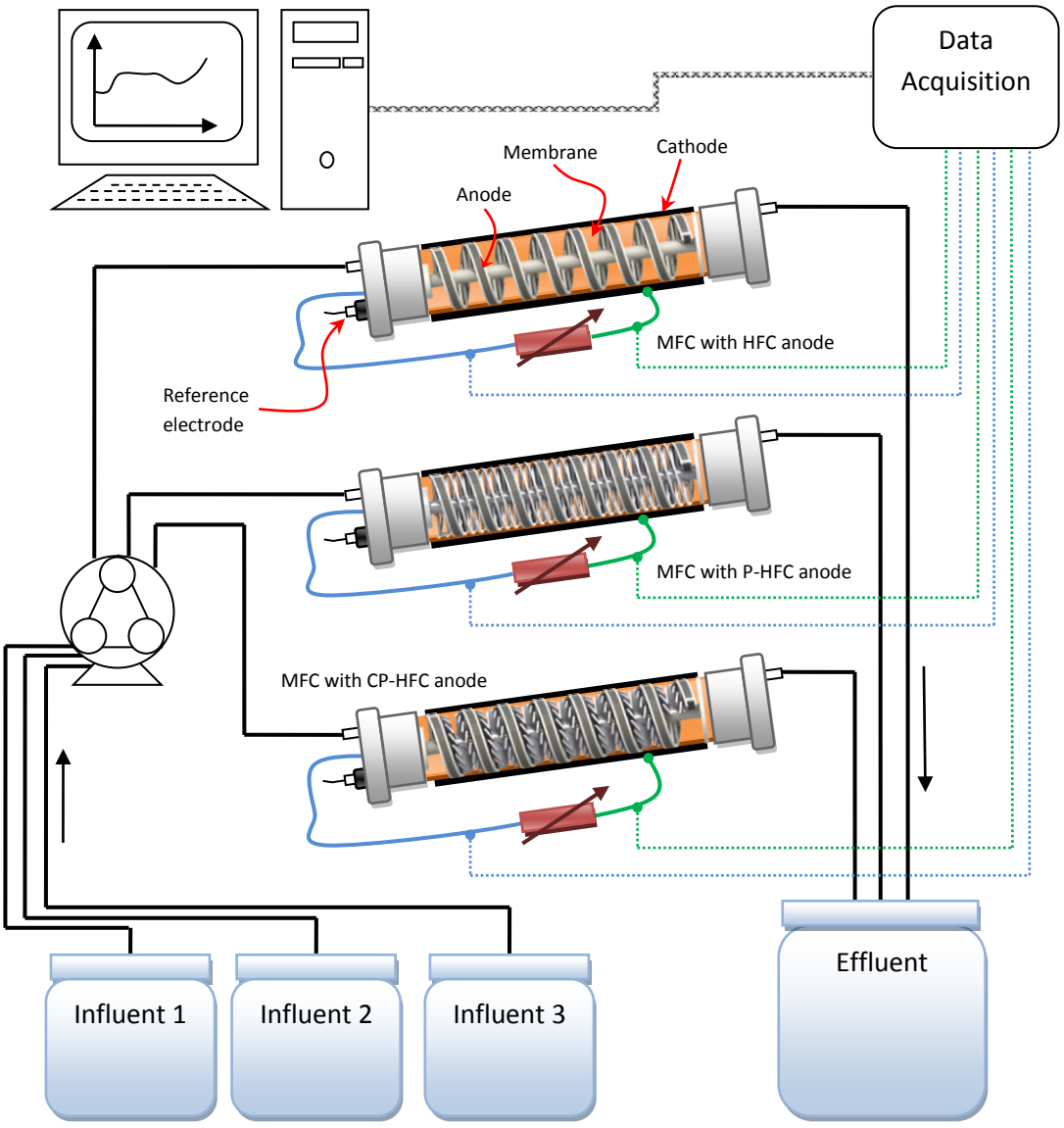

Figure 6.4: Experimental setup to investigate power performance from HFC, P-HFC and CP-HFC when flow rate is varied. Please note that the MFCs are shown in cross-section to show the helical configurations that were studied.

[§] Please note that this value presented was from recalibration due to the clogging up of fluid lines caused during the experimentation.

6.2.2.4 Electrochemical analyses

Prior to carrying out electrochemical measurements (at least 6 hours), media in influent reservoirs and all MFCs were discarded and replenished with freshly prepared media and appropriate buffer, nutrients and substrate to allow the MFCs to reach steady state condition. To measure power generated by each MFCs, the load connected across anodes and cathodes of each MFCs were raised and held for about 6 hours at *circa* 1.1 kΩ and then stepped down to 4.9 Ω in 10 steps, with each step lasting one hour (Table 6.3). Voltage drop (V) across each load (R) was measured via a PC equipped with LabVIEW™ (National Instruments, Newbury, UK) and current (I) and power (P) were calculated using $I = V/R$ and $P = V^2/R$. These measurements were triplicated with each set of measurement performed on a separate day and hence with MFC fed with fresh media.

Table 6.3: Load values that were used in the measurements of power from MFCs.

Load on MFC with HFC anode (Ω)	Load on MFC with P-HFC anode (Ω)	Load on MFC with CP-HFC anode (Ω)
786	1107	1097
504.1	550	549
294.7	314.3	315.3
161.1	165.7	168.3
80	88.1	86.8
30.7	32.7	32.3
10.7	11.3	11.3
8.3	7.7	7.7
7.1	6.3	6.4
5.7	4.9	4.9

As a control, the MEAs (containing the cathodes) of each MFCs were swapped with their corresponding anodes and power was measured. This was repeated for all the combinations of anodes and cathodes. For example, the HFC anode was put into the MEA of MFC containing P-HFC anode and then into the MEA of MFC containing CP-HFC anode and; power was measured on each occasion. This process was repeated for the P-HFC anode as well as CP-HFC anode; consecutively between days 53 – 56 of operation, from inoculation.

Potentiodynamic polarisation measurements were carried out on MFC with HFC anode, single module reactor and also when placed in 5-module long reactor (presented in

Chapter 7), to compare the presented prototype of the scalable MFC against a previously reported monolith carbon electrode material and MEA (Kim et al., 2012, Kim et al., 2009). These measurements were performed using a three electrode system (cathode, anode and a reference electrode) where potential (E) of anode was scanned from 0 V to -0.7 V (at scan rate of 10 mV s^{-1}) against Ag/AgCl reference electrode (saturated KCl, BASi) while measuring current (I) across the anode and cathode, using a Solartron 1287A (AMETEK® Inc., Cambridge, UK). Power was calculated by $P = -(E \times I)$. The negative sign was introduced here since anode potential considered here was measured as negative whereas, the power produced by the MFC will be positive (cathode vs. anode). Here, potentiodynamic polarisation measurements were performed at room temperature of 22 °C, with feed at a flow rate of 3 mL min^{-1} and substrate (acetate) concentration of 40 mM.

6.3 Results and discussion

6.3.1 Power performance characteristics against flow rate

From each set of measurements of the power, the maximum power was noted against the associated flow rate and is represented in Figure 6.5. Error bars represent the error based on triplicate measurements of power. Power was not normalised to volumetric power as the empty bed volume of MFC with CP-HFC anode was 11% and 13% lower (310 mL) than that of MFC with HFC anode (350 mL) and MFC with P-HFC anode (355 mL), respectively, due to the extra components in the helical fluid channel, which could affect the normalised power obtained from MFC with CP-HFC anode, significantly. Considering that the helical carbon channels were identical and the amount of carbon loaded on HFC, P-HFC and CP-HFC anodes were 17.181 g, 15.693 g and 16.197 g, i.e. within 5% of the average of them, power obtained should be comparable when not normalised to the anodic volume. Also, during the experimentations, media was discarded from influent reservoirs as well as MFCs, which may have some electrogens in suspension form and/or mediators that are produced from electrogens and so, power obtained from the MFCs studied here can be considered to have come from the well attached anodic biofilm on the carbon electrode.

Average power (maximum power point, MPP) from MFC with HFC anode was 1.38 mW at flow rate of 1.2 mL min^{-1} increasing to 1.98 and further to 5.97 mW (17.23 W m^{-3}) at 3.5 and 8.9 mL min^{-1}. So, MFC with HFC anode produced approximately 76.9% lower power production at lowest flow rate compared to its power production at highest flow rate studied here (Figure 6.5). In case of MFC with P-HFC anode, the measured average power at MPP was 2.46, 3.40

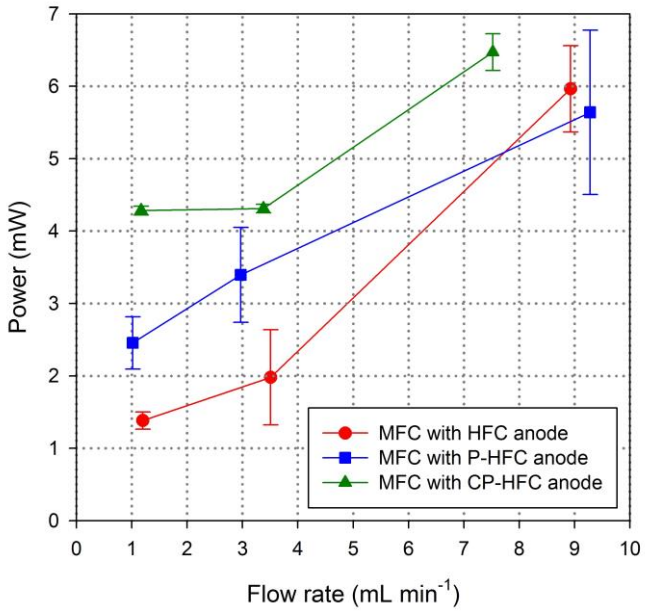

Figure 6.5: Maximum power obtained from MFCs employing three different helical fluid channel configurations, HFC, P-HFC and CP-HFC when flow rate is varied, keeping organic loading rate constant. Error bars represent variation in maximum power based on triplicate measurements.

and 5.64 mW (19.18 W m^{-3}) at 1.02, 2.97 and 9.28 mL min^{-1}, respectively, which represents an almost linear increase in power with increase in flow rate. However, MFC with P-HFC anode seemed to have produced 56.4% less power at the lowest flow rate compared the highest. Power measured from MFC with CP-HFC anode was 4.29, 4.31 and 6.47 mW (22.06 W m^{-3}) at 1.17, 3.38 and 7.52 mL min^{-1}, respectively. It shows only 33.7% less power was produced at lowest flow rate compared the highest flow rate considered. Here, a minimal increase in power was seen between 1.17 and 3.38 mL min^{-1}. Since multiple channel peristaltic pump was used to pump feed into all three MFCs, it was difficult to control and operate all MFCs at same flow rate (with tight tolerance) due to variations in the conditions of the tubing, adapters and fluid path. However, considering linear 3-point interpolation for MFC with CP-HFC anode; hypothetically 7.24 mW may have resulted at a flow rate of 9 mL min^{-1}, to compare with MFC with HFC anode and MFC with P-HFC anode. In this case too, it shows that the MFC with CP-HFC anode would have produced 40.8% less power at the lowest flow rate compared to at 9 mL min^{-1}.

The difference in power due to different HFC designs was significant only at the lowest and intermediate flow rates studied, when average values of measured power are considered. At the lowest flow rate *circa* 1 mL min^{-1}, an increase of 78.3% and 210.9% in power and at circa 3 mL min^{-1}, increase of 71% and 117.6% in power when pillars (in MFC with P-HFC) and converging plates (in MFC with CP-HFC anode) were introduced in helical fluid channels. This

shows importance of mixing in anode chamber of MFCs where product needs to be removed from deep within the electrogenic biofilm matrix and replenish with substrate for conversion into electrical energy.

Power measured from MFC with HFC anode, MFC with P-HFC anode and MFC with CP-HFC anode while swapping their anodes with their respective MEAs are presented in Figure 6.6a-c, respectively, against current produced. The trend in increase in power (and associated current) is evident as seen from the Figure 6.6a-c even though MEA was different in each power measurement for each anode perhaps due to early stage of enrichment (day 53 – 56 since inoculation). All three MEAs were identical in their designs, all cathodes were fabricated in the same batch and also all anodes had identical amount of carbon in them. This suggests that the difference in performance from the three different designs in this study was dominated by the difference in HFC designs.

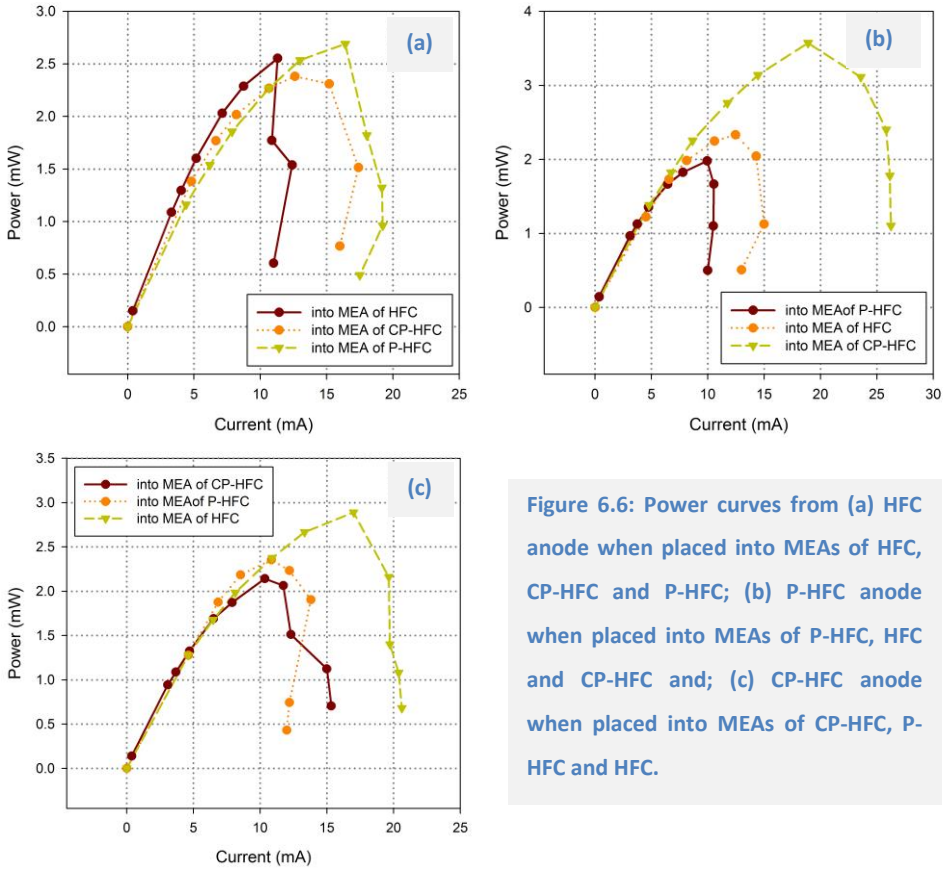

Figure 6.6: Power curves from (a) HFC anode when placed into MEAs of HFC, CP-HFC and P-HFC; (b) P-HFC anode when placed into MEAs of P-HFC, HFC and CP-HFC and; (c) CP-HFC anode when placed into MEAs of CP-HFC, P-HFC and HFC.

6.3.2 Mixing of anolyte

6.3.2.1 Fluid mixing due to helical path

Figure 6.7 shows concentration profile in helical fluid path when a known concentration of solute (40 mol m^{-3} in this case) enters at half the sectional area of the inlet, with nil concentration at the other half of the same inlet, with flow rate of 3 mL min^{-1} (Figure 6.7a-c), flow rate of 1 mL min^{-1} (Figure 6.7d) and 8 mL min^{-1} (Figure 6.7e) as per SIM-1. Colours on the surfaces of HFC indicate the value of concentration locally. Streamlines in Figure 6.7a shows a typical fluid particle velocity profile in an HFC and the colour of streamline indicates the magnitude of fluid velocity at its location.

Examining the fluid velocity in HFC, it is apparent that the fluid particle flows radially inward and outward of the central core as it flows in HFC. Also, the colour of the same streamline shows that it slows as it flows near the wall and speeds up when it flows away from the wall as might be expected. It also shows that the velocity is higher near the inner cylindrical wall of the HFC. An HFC is a circular path that has depth on an axis around which the circular path flows. This means that the increase in the fluid particle velocity near its inner most cylindrical wall is due to the conservation of angular momentum where the particles angular velocity must increase with decrease in the radius from its axis of rotation. All of these interplay in fluid causes torsion in the fluid path that twists as it goes forward in HFC. Looking at the concentration profile in Figure 6.7b and c, it confirms that the fluid with different concentration flows inwards and outwards and twisting along its forward path. Also, cross sectional plot of concentration profile in Figure 6.7c shows when fluid is flowing in the right handed helical fluid channel, the fluid twists in clockwise direction (from reader's point of view in Figure 6.7) with some distortion. Here, it can be seen that diffusion and convection both are playing their roles in mixing when fluid is flowing at lower flow rates at 3 mL min^{-1} (Figure 6.7c) and 1 mL min^{-1} (Figure 6.7d) but when flowing at flow rate of 8 mL min^{-1} (Figure 6.7e) convection seem to be playing dominant role and the fluid seems relatively mixed at about half-way through the HFC and almost completely mixed when it reaches the end of the HFC. However, it seems that the concentration of acetate is not evenly distributed throughout the HFC and the walls do not receive mixed fluid homogeneously throughout.

In MFCs, when an electrode is placed on the side of the HFC, the fluid needs to be completely mixed since the bioelectrochemical reactions are taking place in the helical electrode. Inhomogeneous distribution of concentration on the helical electrode surface could cause concentration gradient and the flow of product and/or reactants could happen within

the electrode. Ideally, for optimal function of the MFC, the products should be taken away from the anode electrode directing towards the cathode and replenish with the substrate to the anode.

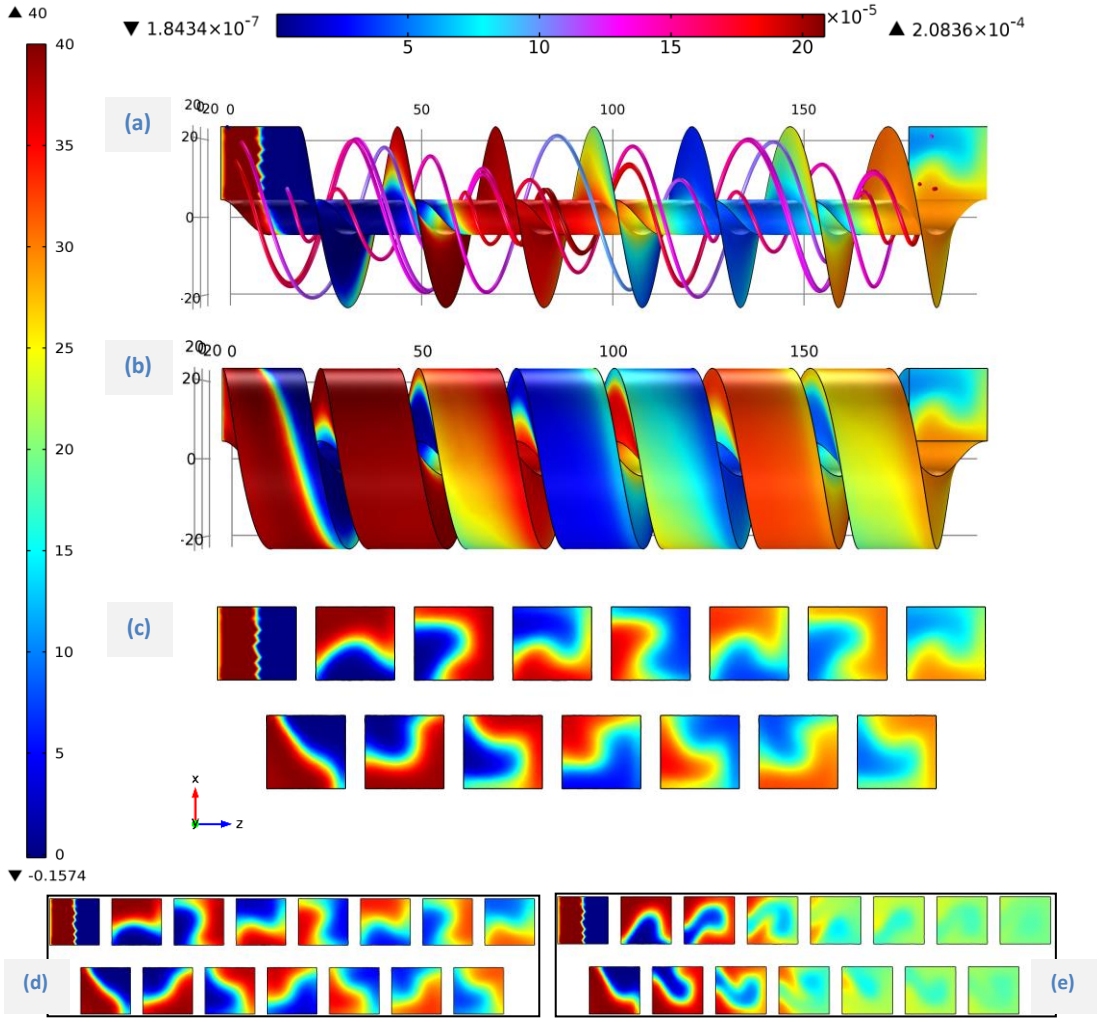

Figure 6.7: Surface plot showing acetate concentration (mol min^{-1}) on (a) helical side wall (with some walls hidden) and streamlines showing fluid flow, (b) walls in helical channel and (c) a plane cut parallel to *xz* plane when flow rate is 3 mL min^{-1} (5.00 × 10^{-8} m^3 s^{-1}), (d) 1 mL min^{-1} (1.67 × 10^{-8} m^3 s^{-1}) and (e) 8 mL min^{-1} (1.33 × 10^{-7} m^3 s^{-1}). Concentration velocity values are shown in the legend vertically placed to the left and horizontally placed on top of all the plots, respectively.

Here, it should be noted that the HFC considered in SIM-1, only shows the fluid flow in HFC with solid walls as an indicative study to show the mixing of fluid in HFC and to appreciate the HFC in its ability to cause passive mixing. However, porous walls in HFC could affect the mixing as the fluid may not flow strictly in a helical direction and diffusive flux will be dominant in the porous media compared to the free flow and the porous material may retain fluid with higher concentration of solute as a result. So, it will be important to cause higher convection

(toward the helical channel) near the surface of porous electrode to drive product out of the electrode by convection.

6.3.2.2 Mixing of anolyte in straight and helical fluid channels with porous walls

Figure 6.8 shows the mixing ratio for SFC and HFC designs as per SIM-2 and SIM-3, respectively. A mixing ratio of 0 indicates perfect mixing and 1, indicates no mixing. The mixing ratios for SFC designs show a decrease in mixing when flow rate is increased from 1 mL min^{-1} to 10 mL min^{-1} and no further decrease in mixing when flow rate continues to increase up to 30 mL min^{-1}. This is in contrast to the mixing effect seen in Figure 6.7c, d and e where mixing was improved with increase in fluid flow. Decrease in mixing in SFCs could be due the porous anodes where convection in porous media is limited and mixing is limited mostly through the diffusion. When flow rate is increased, much of the flow goes straight through the fluid channel and concentration flux out of the porous anode is difficult in the opposite direction of positive pressure applied by the fluid onto the porous anode. Introducing the pillars in SFC, i.e. P-SFC, the mixing seemed to have improved and with converging plates in CP-SFC, a further increase in mixing was observed. However, when HFCs are considered, the mixing ratio indicates that introducing P-HFC and CP-HFC, mixing was not improved. Moreover, HFC

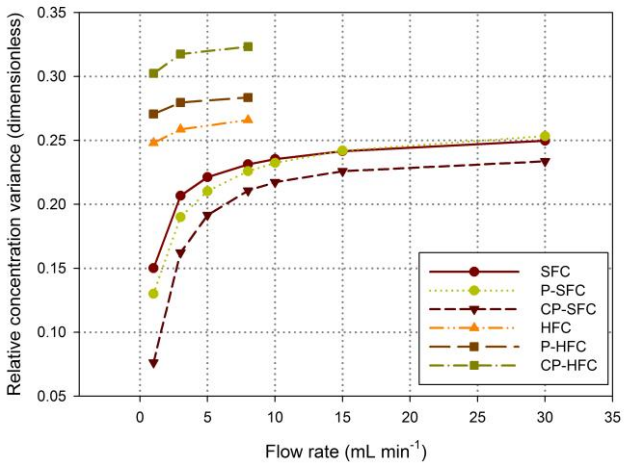

Figure 6.8: Mixing ratio (ratio of concentration variance of a chemical species at outlet to inlet) obtained at different flow rates for straight fluid channel configurations and helical fluid channel configurations.

variants do not seem to have significant effect in the mixing ratio compared to the SFC variants, when the flow rate is varied.

Figure 6.9 shows concentration of H^+ (in colour), generated at porous electrode in sections from different designs of straight multiple fluid channels as per SIM-2 and Figure 6.10 for H^+ concentration at the outlet of different HFC designs as per SIM-3. The arrows indicate

overall H^+ concentration flux due to diffusion and convection. The arrow sizes are scaled in accordance with the maximum value of flux in the same plot.

As shown in Figure 6.9A1, B1 and C1, the H^+ seem to be swept away by the convective flux from the porous electrodes towards the outlet, with maximum concentrations of 1.35, 1.38 and 1.53 mol m^{-3} towards the porous electrode at the outlet of SFC, P-SFC and CP-SFC. Distinct bands of concentration of H^+ in the fluid channel and porous electrode in Figure 6.9A1, B1 and C1 shows that the H^+ would have leached into the fluid channel where they are transported by the convection flux caused by fluid flow which is indicated by the distorted

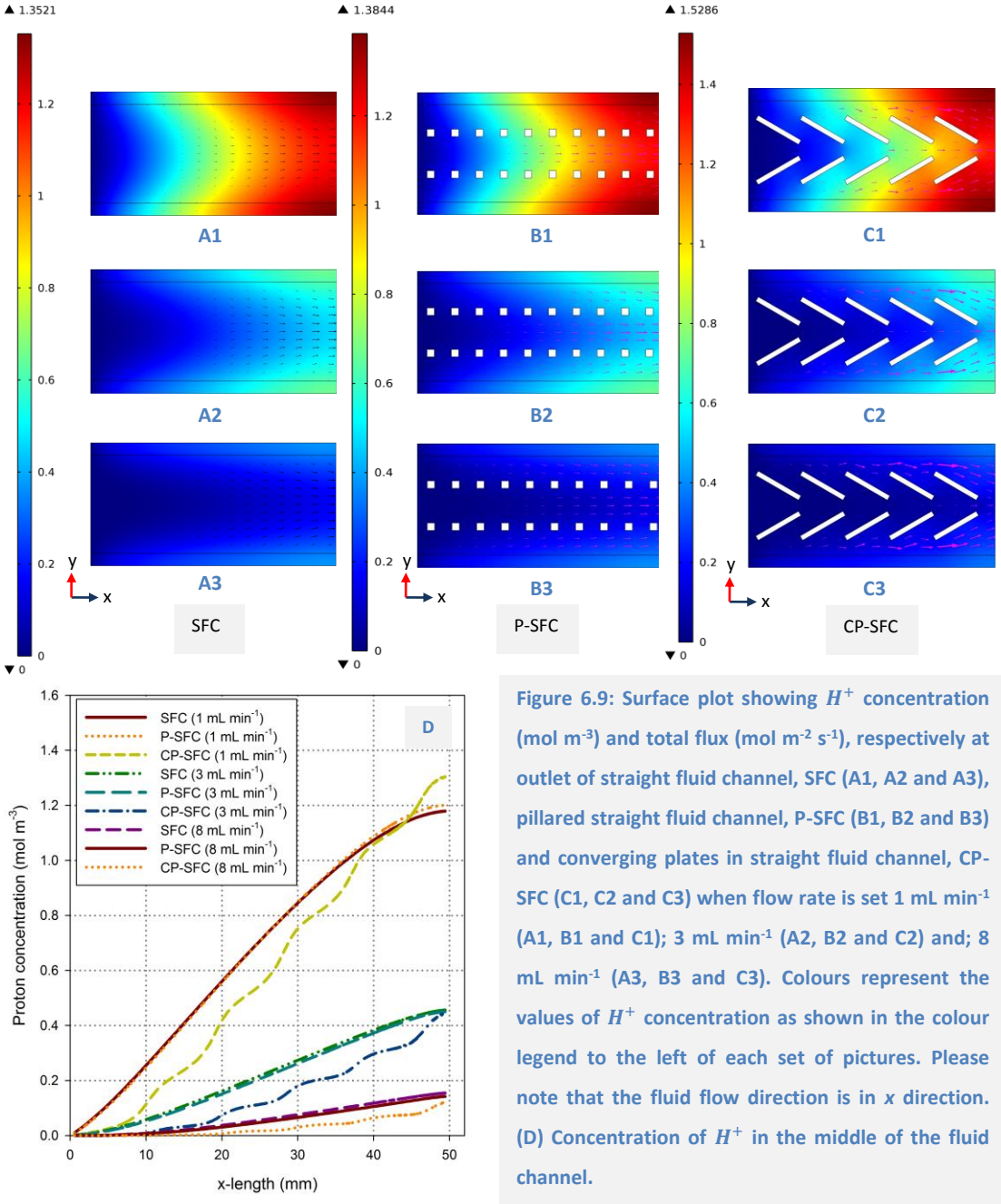

Figure 6.9: Surface plot showing H^+ concentration (mol m^{-3}) and total flux (mol m^{-2} s^{-1}), respectively at outlet of straight fluid channel, SFC (A1, A2 and A3), pillared straight fluid channel, P-SFC (B1, B2 and B3) and converging plates in straight fluid channel, CP-SFC (C1, C2 and C3) when flow rate is set 1 mL min^{-1} (A1, B1 and C1); 3 mL min^{-1} (A2, B2 and C2) and; 8 mL min^{-1} (A3, B3 and C3). Colours represent the values of H^+ concentration as shown in the colour legend to the left of each set of pictures. Please note that the fluid flow direction is in *x* direction. (D) Concentration of H^+ in the middle of the fluid channel.

shape of concentration bands in the fluid channel. Introducing the pillars in fluid channel (P-SFC) does not seem to have significant effect on the removal of H^+ from porous electrode compared to the SFC. Whereas, introducing converging plates in the fluid channel (CP-SFC) seems to transport more H^+, compared to the SFC and P-SFC. Also, the shape of concentration bands implies that the H^+ are driven out of the porous electrode due to the high velocity caused near the electrode surface (looking at the flux arrows) and are channelled towards the middle of the fluid channel where convection flux with high fluid velocity takes H^+ away with it (Figure 6.9C1).

Figure 6.9D shows H^+ concentration measured on a line that passes through the middle of the fluid channel and it is clearly seen that the H^+ transport in CP-SFC is higher than that of SFC and P-SFC. Between the SFC length of 40 mm – 50 mm in CP-SFC when flow rate is 1 mL min^{-1}, the H^+ concentration is higher than that of the SFC and P-SFC, which could be due to the inclined planes where the velocity of the fluid particle is slowed down at the back of the plate (the face of the plate opposite to the flow direction). However, at higher flow rates, H^+ concentration in the middle of the channel was lower for the CP-SFC than for the SFC and P-SFC (Figure 6.9D). A similar trend was found when the H^+ concentration was plotted at the middle of the porous electrode (i.e. where symmetry is assumed in SIM-2). This shows that introducing converging plates in the SFC could be beneficial as it helps drawing the product away from the reaction site.

Figure 6.10 shows similar trends in HFCs with different design configurations to that of SFCs when H^+ concentration is plotted on the outlet of HFCs. Here, the forward fluid direction is into the plane towards –*z*. Figure 6.10C1, C2 and C3 indicates that the H^+ is driven out of the porous anode towards the fluid channel due to the converging plates and distorted concentration profile is evident. Whereas in HFC and P-HFC, H^+ concentration in fluid channel seems lower than that of the CP-HFC and also arrows indicate that the flux is toward the porous anode (right side anode in HFCs and P-HFCs in Figure 6.10) rather than toward the channel which would not be desired as it does not form positive concentration gradient that can draw the H^+ out of the electrode.

The lower mixing in CP-HFCs compared to P-HFC and HFC in Figure 6.8 could be due to this distinct concentration profiles obtained at the outlet due to converging plates. The lowest concentration of less than 0.05 mol m^{-3} is seen in the centre of the fluid channel and towards the top and; concentration between 0.1 and 0.2 mol m^{-3} is seen in the fluid channel between the plates and anodes (Figure 6.10C1). This could have affected the mean and the variance

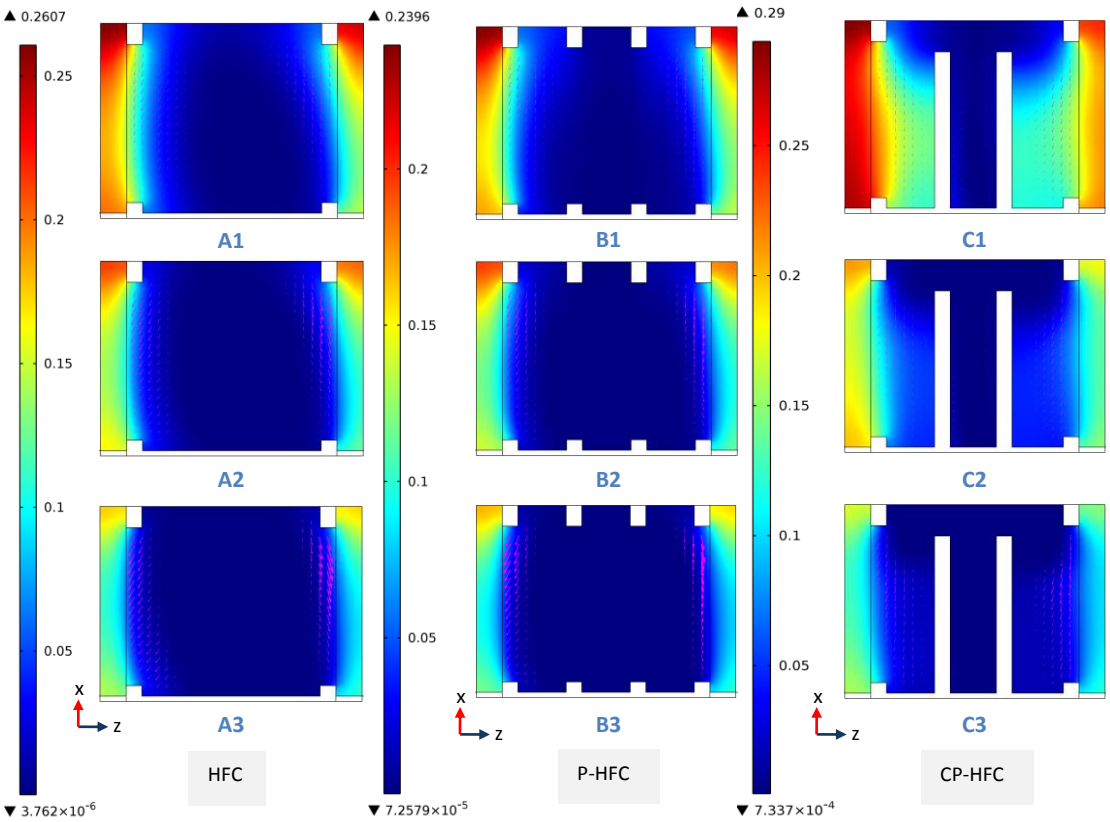

Figure 6.10: Surface plots and arrow plots showing H^+ concentration (mol m^{-3}) and total H^+ concentration flux (mol m^{-2} s^{-1}), respectively at outlet of HFC (A1, A2 and A3), P-HFC (B1, B2 and B3) and CP-HFC (C1, C2 and C3) when flow rate is set 1 mL min^{-1} (A1, B1 and C1); 3 mL min^{-1} (A2, B2 and C2) and; 8 mL min^{-1} (A3, B3 and C3). Colours represent the values of H^+ concentration as shown in the colour legend to the left of each set of pictures and the size of arrow is scaled to represent the magnitude of total flux relative to the maximum flux in each plot. Please note that the flow direction is in –*z* direction.

which is used to calculate the mixing ratio. Though the value of mixing ratio advises on the degree of mixing in the fluid, it does not represent the only factor which affects the performance of a bioelectrochemical reactor such as an MFC. Experimental results suggest that the inclusion of pillars and converging plates increased the power performance of MFC. However, looking at the concentration profile plots as discussed above for HFC, P-HFC and CP-HFC (Figure 6.10), it is evident that the product removal is more in CP-HFC design than compared to the HFC and P-HFC. It is possible that the removal of product, i.e. H^+ from the anode could drive the degradation bioelectrochemical reaction forward to degrade more acetate into H^+ and generate electrons and was probably the reason for the better performance of CP-HFC anode design compared to HFC and P-HFC anodes. It also implies that the product inhibition in the CP-HFC anode, i.e. localised pH decrease could have been mitigated by removing the products, in this case H^+ and this could have optimised the localised pH in the vicinity of the biofilm and ultimately improving the performance.

6.3.2.3 Comparison of HFC anode designs with the aid of fluid velocity and pressure

In Figure 6.11, streamlines show the velocity in 3D and surface plots show concentration of H^+ on the surfaces of porous anodes and helical fluid channel. Some surfaces of the fluid channel and anodes are hidden so that the streamlines in fluid channel are visible. Increase in fluid velocity is observed with respect to increase in the flow rate and the velocity in HFC and P-HFC is uniformly distributed throughout but for the CP-HFC, the fluid increase of the fluid velocity is observed predominantly in the converged part of the plates in CP-HFC. Also, when flow rate of 8 mL min^{-1} is considered, the maximum velocity in P-HFC and CP-HFC seems to be 1.32 and 1.99 times higher than that of HFC. The streamlines indicate that the fluid is flowing straight through the HFC whereas in P-HFC obstructions posed by the pillars create turbulence in the fluid flow, splitting and merging of the fluid may happen and as a result, the fluid will have more tendencies to mix passively as it flows along its path, compared to only HFC. Streamlines in CP-HFC however, indicate that the plates are directing the fluid to

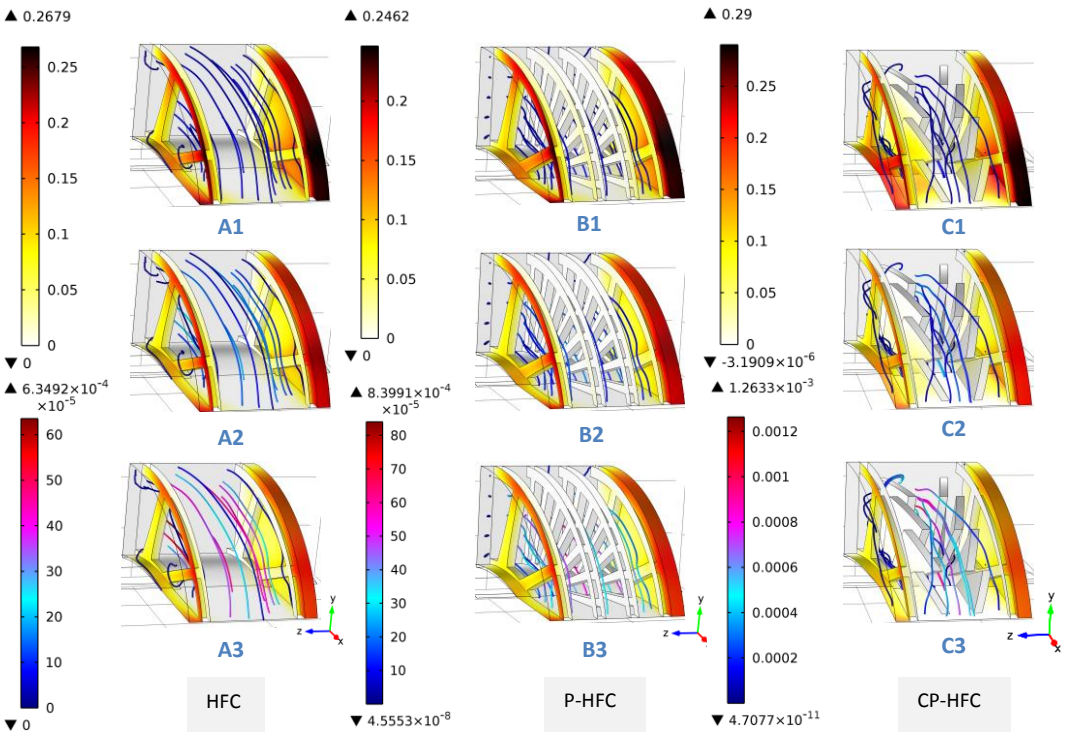

Figure 6.11: Surface plots showing H^+ concentration (mol m^{-3}) on the surfaces and streamline plots showing fluid velocity (m s^{-1}) shown in figures for HFC (A1, A2 and A3), P-HFC (B1, B2 and B3) and CP-HFC (C1, C2 and C3) when flow rate is set 1 mL min^{-1} (A1, B1 and C1); 3 mL min^{-1} (A2, B2 and C2) and; 8 mL min^{-1} (A3, B3 and C3). Colours represent the values of H^+ concentration as shown in the colour legend to the top left and of fluid velocity on the bottom left of each set of plots. Please note that some surfaces are hidden so that streamlines in 3D can be visible.

converge and diverge, split and merge due to which the fluid will be rigorously mixed as it flows along its path. Moreover, this also creates differential pressure between the boundary of the anode and the vicinity of fluid channel, due to which it helps to draw the H^+ out and replenish the substrate in the anode. Also the streamlines indicate that the overall tendency for it to flow is radially toward the membrane which directs the H^+ rich fluid toward the membrane. Also, from concentration plots it is evident that the H^+ concentration is higher at outer surface of the anodes in all designs compared to the inner part of the anodes suggesting that the helical flow would be beneficial in transporting product (here H^+) toward the membrane and cathode.

Observing the streamlines close to the fluid channel and anode interface, it is evident that the fluid velocity is higher in P-HFC compared to the HFC and CP-HFC which could be causing higher shear at the anode surface in P-HFC compared to the HFC and CP-HFC and it is evident when the maximum shear rate on the anode surface is plotted against the flow rate is in Figure 6.12. Maximum shear rate on P-HFC is higher compared to CP-HFC and in CP-HFC compared to HFC. It has been shown previously (Kim et al., 2012, Michie et al., 2014, Pham et al., 2008) that higher shear rate causes improvement in performance which is probably the

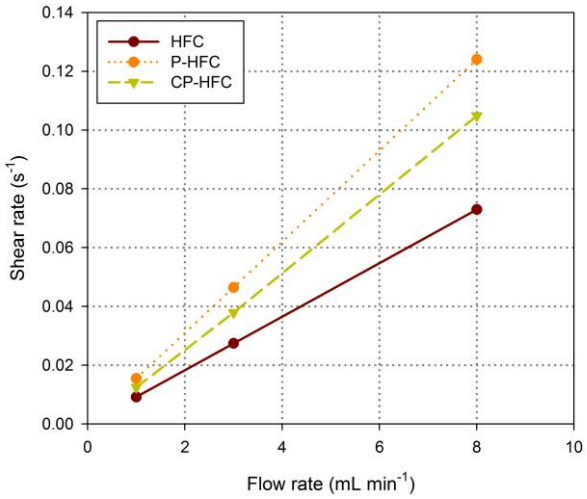

Figure 6.12: Maximum shear rate obtained on forward facing helical anode surface area at different flow rates for helical fluid channel configurations.

reason for higher performance from P-HFC compared to HFC in Figure 6.5. However, in CP-HFC a combined effect of high shear rate at the anode surface and removal of H^+ could be the reason for higher performance from CP-HFC compared to both, HFC and P-HFC.

Figure 6.13 shows pressure applied to the fluid over the fluid channel to cause flow, as observed on a plane half-way through the fluid channel (plane cut at 45° to *yz* and *xz* and passing through *z* axis). It is evident that the average of maximum pressure values from P-HFC and CP-HFC is approximately 4.5 and 6.2 times higher than that of the HFC, respectively, considering all flow rates studied in Figure 6.13. This means that at a given flow rate, 4.5 and 6.2 times the energy input would be required in P-HFC and CP-HFC than that of HFC,

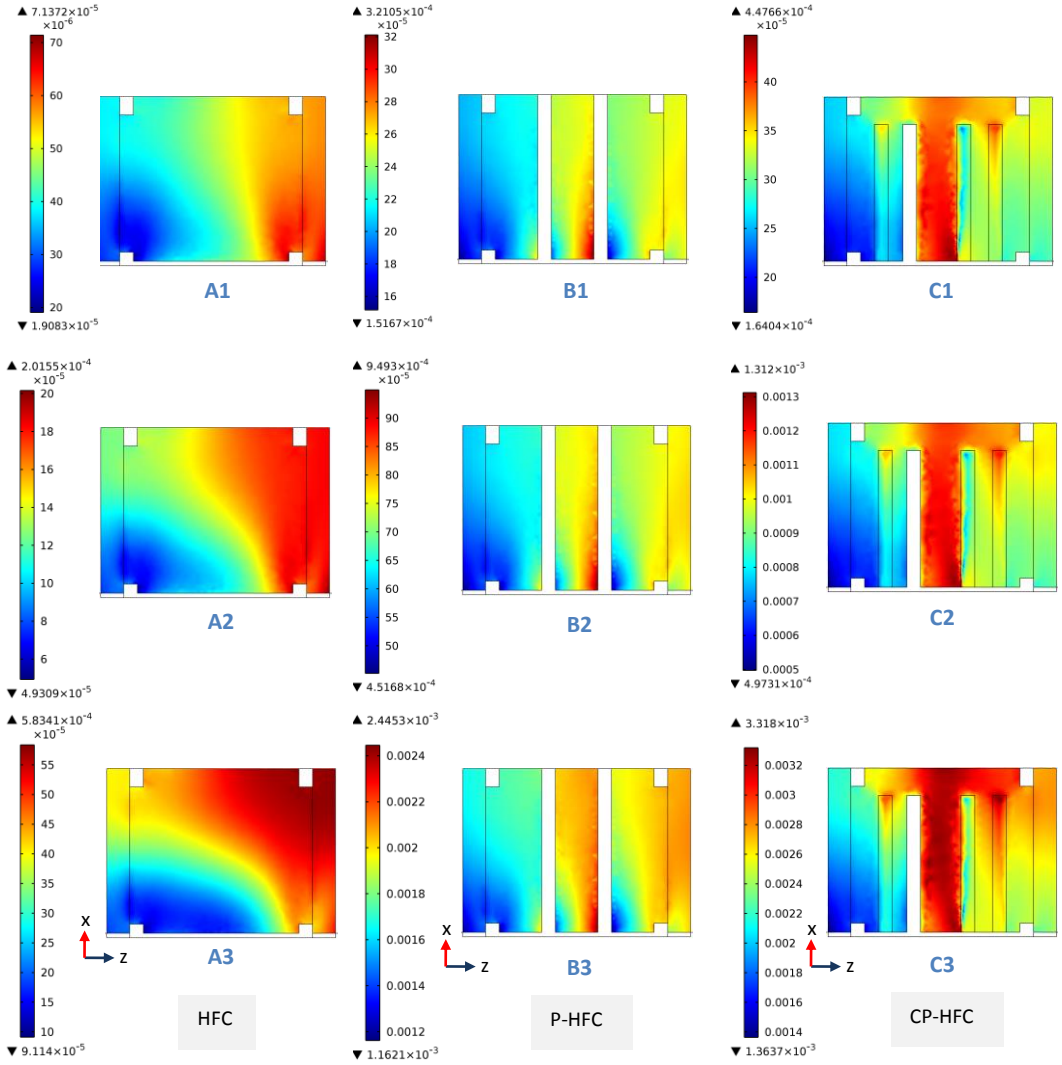

Figure 6.13: Surface plot showing pressure (Pa) on plane (45° inclined to *yz* and *xz* and passing through *z* axis) for HFC (A1, A2 and A3), P-HFC (B1, B2 and B3) and CP-HFC (C1, C2 and C3) when flow rate is set 1 mL min^{-1} (A1, B1 and C1); 3 mL min^{-1} (A2, B2 and C2) and; 8 mL min^{-1} (A3, B3 and C3). Colours represent the values of pressure (Pa) as shown in the colour legend to the left of each pictures. Please note that the flow direction is in –*z* direction.

respectively, in terms of fluid pumping. So, this means that the increase in performance of MFC may be at the expense of extra energy input (depending on externalities) which would be required to cause mixing and cause an effective turn-over of substrate.

The pressure profiles in HFC indicate that the pressure is applied almost in longitudinal direction at lower flow rates changing to almost the radial direction towards the centre of HFC at highest flow rate. This means that in HFC at lower flow rates, the tendency of fluid flow will be toward plug flow, which could prove inhibitory to the biofilm in anodes. Biofilm in this case receive H^+ rich fluid causing pH to drop locally. When observing pressure profiles in P-HFC pressure seems higher near the root of the pillars compared to both sides of the pillars which could cause fluid to flow in both directions of the pillars and fluid will have tendency to flow forward and around the pillars while moving in forward helical direction. Pressure profile in the middle of the CP-HFC seems higher throughout compared to the outside of the converging plates. Here, in Figure 6.13C1, C2 and C3, one set of leading edge (starting of the plates) and one set of tail end (ending of the plates) of the plates are observed. Naturally, the highest pressure (in red) seems to be occurring from the tail end of the converging plates. This means that the fluid has a tendency to flow forward in converging plates causing regions of lower pressure near the anode surface and inducing flow out of the porous anode, directed radially outwards toward the membrane and cathode.

All, increase in power performance in MFCs at low levels of energy input is sought in order to increase overall efficiency. The tension between improved performance derived from the mixing induced by higher flow rates and the energy required to drive the flow, must be reconciled for optimum efficiency.

6.3.2.4 Recommended configuration for HFC design

To compensate for the requirement of higher input energy required to the CP-HFC anodes, an alternative but similar anode fluid channel design as shown in Figure 6.14 is recommended. Here one of the converging plates is removed from each set to give alternate converging plates in helical fluid channel (ACP-HFC). The H^+ concentration plot in Figure 6.14A1-A3 shows that the H^+ removal from anode in ACP-HFC is as effective as in CP-HFC (Figure 6.10C1-C3). Furthermore, the pressure values in Figure 6.14B1-B3 for ACP-HFC is similar to P-HFC in Figure 6.13B1-B3, which means lower energy input is required compared to CP-HFC, ACP-HFC and the arrangement may be expected to provide similar performance to CP-HFC. Again, the streamlines of the velocity plots in Figure 6.14C1-C3 indicates that the plates cause the fluid to flow alternate towards and away of the anodes in the fluid channel, which could drive H^+ from the anode and the substrate to the biofilm. Surface plots of H^+show that H^+ have carried radial component of motion outwards toward the membrane and cathode.

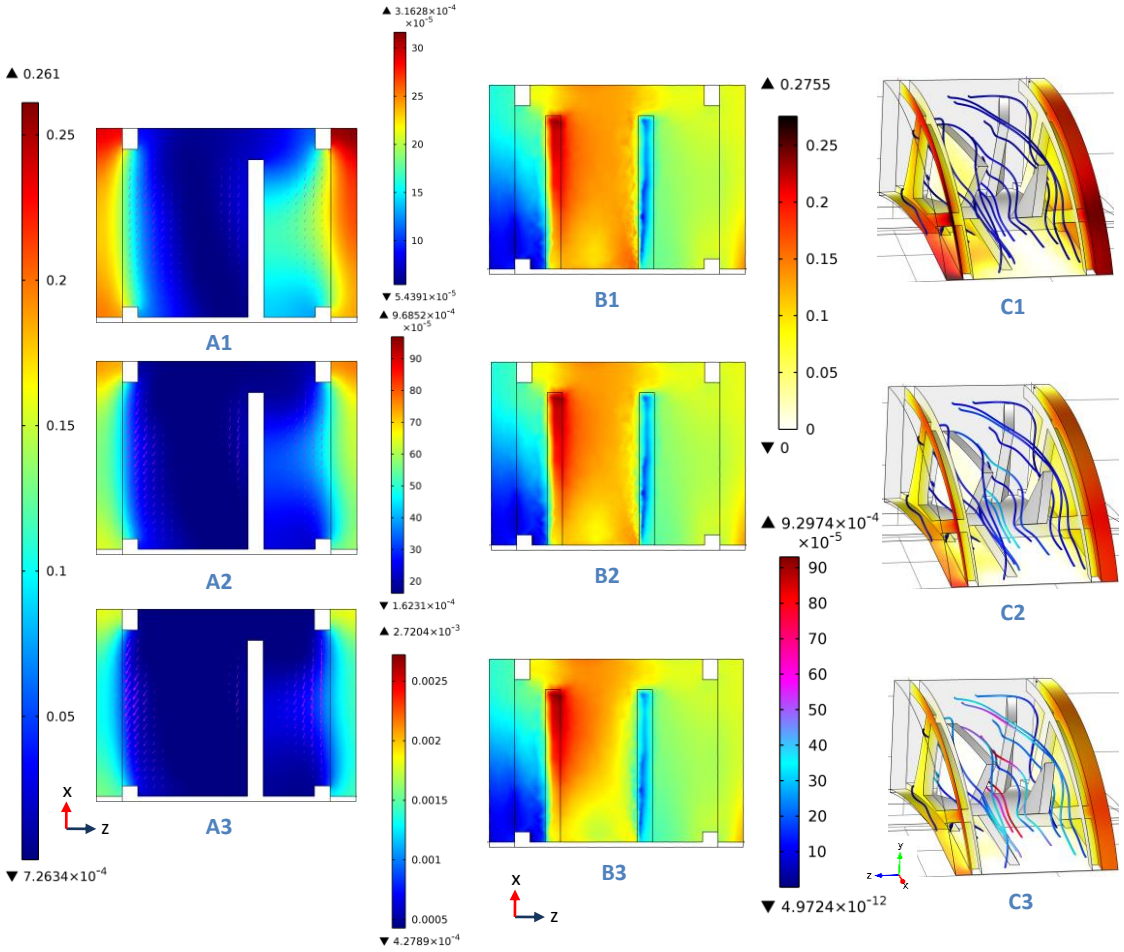

Figure 6.14: Surface plots and arrow plots showing H^+ concentration (mol m^{-3}) and total H^+ concentration flux (mol m^{-2} s^{-1}), respectively at outlet (A1, A2 and A3), pressure (Pa) at plane cut 45° inclined to *yz* and *xz* and passing through *z* axis (B1, B2 and B3) and; H^+ concentration (mol m^{-3}) and fluid flow in alternate converging plates in helical fluid channel (ACP-HFC), (C1, C2 and C3) when flow rate is set to 1 mL min^{-1} (A1, B1 and C1); 3 mL min^{-1} (A2, B2 and C2) and; 8 mL min^{-1} (A3, B3 and C3). Colours in each plot represent the values as shown in legends placed at left of each set of plots. Please note that some surfaces are hidden in 3a, 3b and 3c to so that streamlines in 3D can be visible.

A mixing ratio of approximately 0.3 and maximum shear rate of 0.02, 0.06 and 0.18 s^{-1} at flow rate of 1, 3 and 8 mL min^{-1}, respectively (Figure 6.15) for ACP-HFC, indicates that they are comparable to the mixing ratio (Figure 6.8) and maximum shear rate (Figure 6.12) obtained for the anode designs studied here. Therefore, removing alternative plates from the converging plates in CP-HFCs could produce comparable power output to CP-HFC, but at lower energy input with obvious benefits in terms of efficiency. However, this inference from modeling would need to be verified, experimentally.

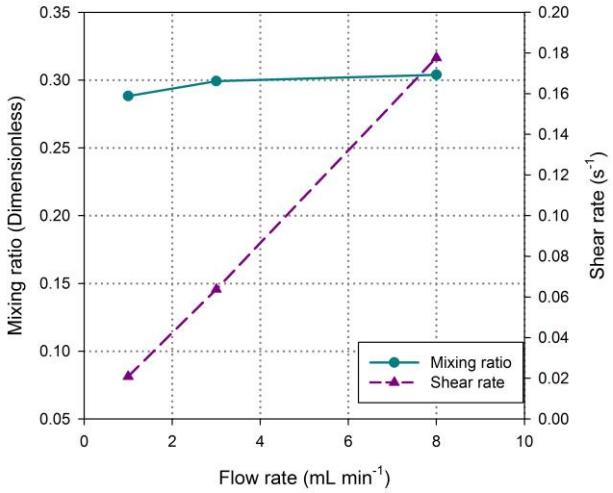

Figure 6.15: Mixing ratio and maximum shear rate (s^{-1}) at forward facing helical anode surface area against flow rates for alternate converging plates in helical fluid channel (ACP-HFC) configuration.

6.3.3 Comparison between scalable MFC prototype and a micro-porous monolithic conductive carbon (MMCC) anode MFC

The helical electrode (HFC) presented here differs in its design to the helical electrode studied before (Kim et al., 2012) in terms of its diameter (46 mm compared to 36 mm), width of the electrode channel (5 mm compared to 13 mm), width of fluid channel (20 mm compared to 5.4 mm), electrode material (conductive carbon cloth compared to micro-porous monolith conductive carbon, MMCC for anodes). The MMCC offers large surface area to volume and is also highly conductive as per the study shown by Kim et al. (2012). The helical anodes (along with the MEA) developed here is aimed towards scaling-up of the MFC process for the treatment of wastewater. Therefore, it would be desired to compare the performance of the helical electrode presented here to the high performance helical anodes studied previously to see its suitability in terms of power performance.

It is evident that the MFC with HFC anode produced 8.5 mW (35 mA) and 16.8 mW (67 mA) when placed in MEA tube for one anode and MEA for five anodes, respectively; (Figure 6.16) compared to 5.4 mW (73 mA) produced from the MMCC anode when placed in an MEA for one anode as reported previously by Kim et al. (2012). The span of power curve is broader for MMCC anode and current production at maximum power is higher compared to the HFC anode which could be due to a combined effect from the higher capacitive carbon compared to the carbon cloth used in HFC anode and also perhaps availability of more surface area in the MMCC electrode compared to the carbon cloth anodes in HFC anode. However, the maximum power production from HFC anode appears to be higher than that of the MMCC anode.

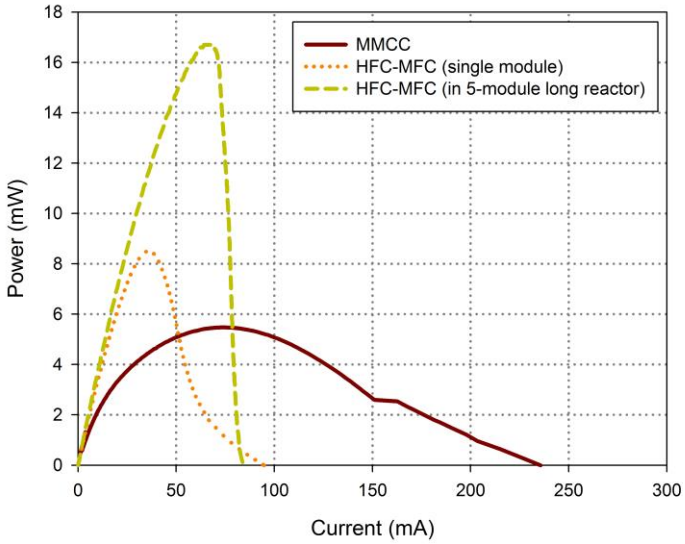

Figure 6.16: Potentiodynamic polarisation curves for micro-porous monolith conductive carbon (MMCC) anode, HFC when placed in single module reactor MFC and HFC when placed in 5-module long reactor.

Previous work on helical anode (Kim et al., 2012) has shown that the pillars can be causing mixing effect and it was qualitatively shown and argued. In this chapter, it has been shown that the enhancement in performance can indeed be achieved by introducing static mixers (pillars and converging plates) in the fluid channels of the anode. The use of static mixers may be transferrable to different anode design and can be verified using similar techniques to the shown in this chapter. The multiphysics modeling approach also enhanced the understanding of the helical anodes and facilitated the anode design for improvement in the performance of MFCs. The optimisation in the anode, being an element (component) of the system, can elevate the performance of the overall system and in this case, it can enhance the power of up-scaled MFC.

7. Modularised Up-scaling of MFCs for their use in wastewater treatment

7.1 Introduction

The optimal axial length of the helical anode design has not been considered to-date and has been determined in part by the physical dimensions (typically 254 mm × 254 mm × 305 mm) of the workbench of the available rapid prototyping machines (1200es, Dimension Inc., MN, USA) and the required anodic volume, typically about 250 – 300 mL. It has been shown previously that in a stack of tubular MFCs, increasing the anode length (by connecting adjacent MFC modules in parallel electrically) can cause losses in power as the successive MFCs may produce low power because of the substrate concentration gradient where subsequent modules receive effluent from preceding MFC with lower substrate concentration because of limited longitudinal mixing and substrate depletion (Kim et al., 2011a). Loss in power was also observed in a similar stack of MFCs, attributed to electrical cross-conduction effects in MFCs connected hydraulically in series (Zhuang et al., 2012b).

This chapter considers the optimal length of the MFC module employing helical anodes and the MEA developed in Chapter 6. This should ideally provide the same power as to the aggregated power from its smaller axial lengths MFC modules. This would be helpful in manufacturing, where the manufacturing process can be interrupted less frequently with longer MFC modules compared to shorter modules. Assembly would be simplified by fewer parts per unit volume. Furthermore, this chapter will argue that MFC technology can be up-scaled by modularising, without incurring unacceptable losses in power and therefore demonstrate that the approach would be plausible for applications in wastewater treatment, where it could recover energy in terms of electricity while treating the wastewater.

7.2 Materials and methods

7.2.1 MFC assembly

A CEM tube was fabricated using the techniques and materials presented in section 6.2.2.2 but with tube length of 1.05 m (Figure 7.1) and the membrane overlapping by 15 mm (such that flat membrane sheet is turned into the tube). Two of HFC anodes, two P-HFC anodes and one CP-HFC anodes were manufactured by rapid prototyping (Digits2Widgets, London, UK) with nylon material, fabricated as described in section 6.2.2.1 and were laid in line in the order

just given, informed by the results in Chapter 6 to compensate for the decrease in performance towards the end of the tube. The weight of carbon assembled into the formers to produce the anode electrodes were 13.60, 13.75, 15.83, 17.71 and 18.88 grams for respectively named MFC-1, MFC-2, MFC-3, MFC-4 and MFC-5. A multi-core cable (1190213, Farnell, Leeds, UK) was passed through the centre of the anodes and each wire was stripped and soldered in turn to a current collector, and accommodated in the cable housing provided on the anode former (Figure 6.2a for anode former). Also, at the end of the last module, a heat-shrink tube (2192425, Farnell, Leeds, UK) was used to seal the open ended cable insulation (both ends), in combination with silicon sealant inside the heat shrink. This assembly was pushed into the hole provided for the cable to a make seal and also to ensure no leakage occurred through the cable. This was then passed through the cable gland provided on the cap and secured. Cathodes, (200 mm × 160 mm) were placed onto the CEM tube with hydrogel applied between the CEM and electrode as described in section 6.2.2.2. A 10 mm interval was left in between the cathode electrodes to interrupt electrical continuity. The measured resistances between the adjacent cathodes were greater than 3 MΩ. Connections to the cathodes were made using crocodile clips. Empty bed volume was 1.42 L.

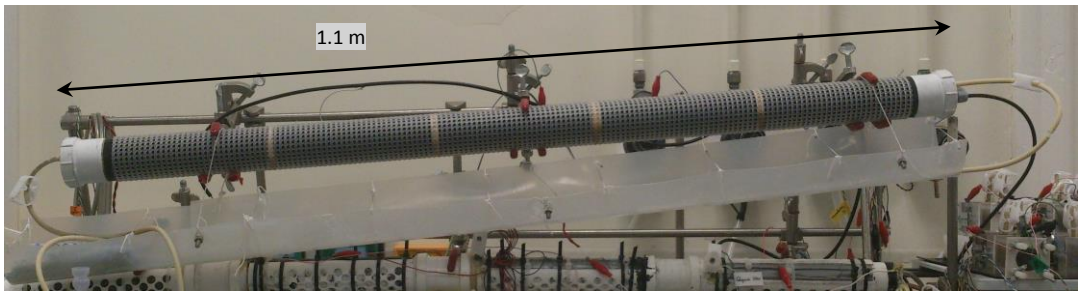

Figure 7.1: A multi-module MFC tube accommodating five MFCs, sharing the CEM and anolyte.

7.2.2 MFC operation

The extended tube containing MFC modules was inoculated as described in section 6.2.2.3 with all anodes and cathodes connected electrically independent, forming 5 different MFCs in a single continuous tube (multi-module tube MFC). Static loads of 10 Ω were connected across each MFC during the start-up. The media containing inoculum was re-circulated through a 2 L bottle at approximately 3 mL min^{-1}. The pump was stopped on day 10.9 to put all the MFCs into batch mode in order to investigate the effect of recirculation; and was turned on again on day 11.9. The media was discarded and replaced with fresh media after 13 days, when voltages across the MFCs (after the MFCs had started-up) were observed to be falling due to substrate depletion.

Once the MFC power was reasonably stabilised after 40 days, MFC length (MFC configuration) was increased stepwise by connecting the subsequent MFC electrically in parallel, so that 0.21 m (Only 1 MFC; O1-MFC), 0.42 m (MFC 1 and 2 in parallel; 2P-MFC), 0.63 m (MFC 1, 2 and 3 in parallel; 3P-MFC) and 0.84 m (MFC 1, 2, 3 and 4 in parallel; 4P-MFC) were the resulting configurations. Power curve measurements and cyclic voltammetry were conducted for each set of MFC configurations. The measurements were performed in duplicate. Additionally, coulombic efficiency was determined for the whole multi-module MFC reactor.

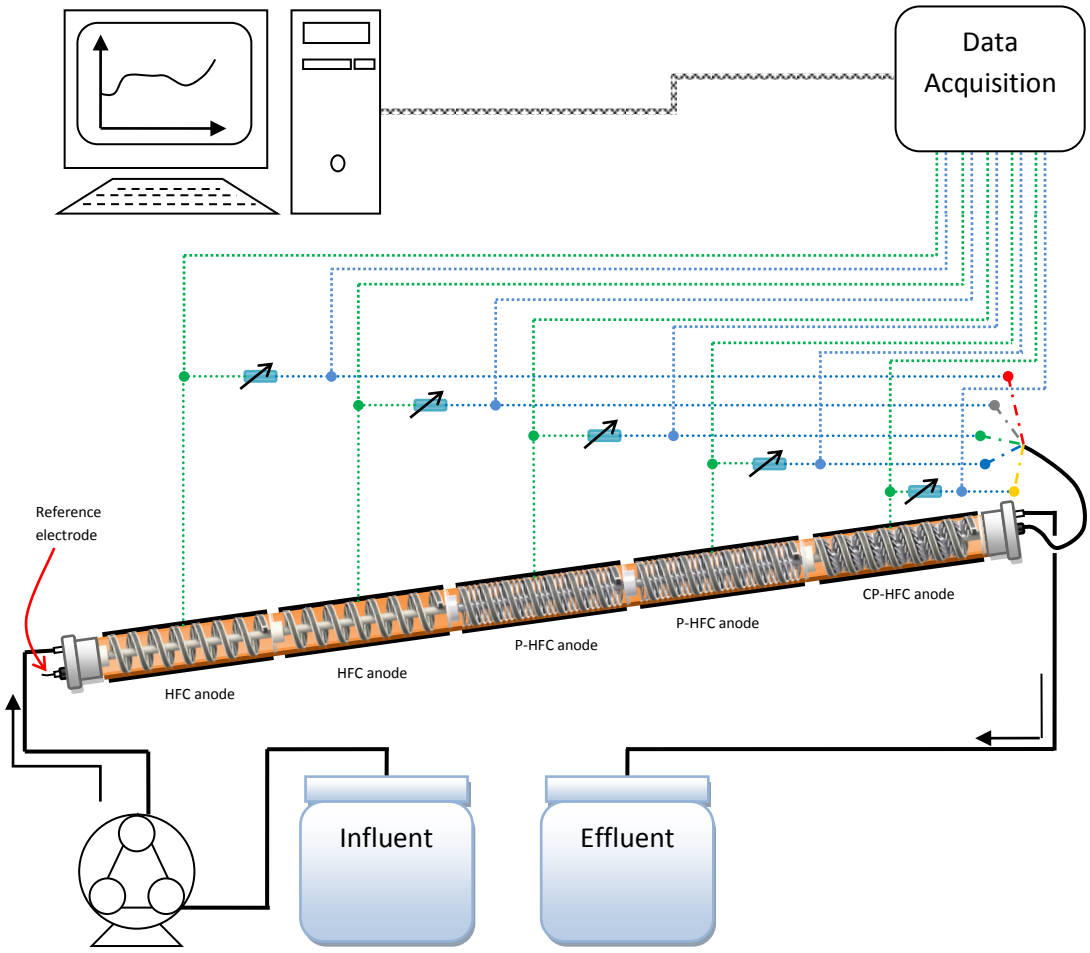

Figure 7.2: Experimental setup to determine the optimum length of a single MFC module. All MFCs in the multi-module tube are electrically independently connected. MFCs are shown in cross-section to show the helical configurations used in the study.

During the experiment, media containing 10 mM sodium acetate was fed to the MFC tube at a flow rate of approximately 3 mL min^{-1} with influent and effluent containers kept separate (Figure 7.2). The media from influent and effluent container, and MFC tube was

replaced with fresh media before starting each set of the measurements (each set lasting approximately 24 hours). The MFC was run at a temperature of 22 ± 3 °C.

7.2.3 Electrochemical analyses

Voltages from MFCs were measured using a personal computer as described before in section 3.2.3.1 but with NI-USB 6343 device (National Instruments, Newbury, UK). Electrical power and current measured and calculated from MFCs as described before (section 3.2.3.1), varying electrical load from the highest load to the lowest load with load values ranging as shown in the Table 7.1.

Table 7.1: Load values that were used in the measurements of power from MFCs in various configurations.

MFC configuration	Load values used in power measurements	
	set 1	set 2
O1-MFC	4.2 Ω – 130.3 Ω	4.2 Ω – 130.3 Ω
2P-MFC	6.9 Ω – 235.7 Ω	3.8 Ω – 116.7 Ω
3P-MFC	3.8 Ω – 118.2 Ω	1.9 Ω – 58.8 Ω
4P-MFC	1.3 Ω – 39.5 Ω	1.3 Ω – 39.5 Ω

Estimated power for the electrically parallel connected MFCs was determined by averaging voltages and summing the current produced by the same MFCs when connected to the load independent. Impedance of the MFC was considered to be matched with the load connected to it when it produced the maximum power and so, the value of load at this point was noted to be the internal impedance of the MFC.

Coulombic efficiency (ϵ_c) was measured for the whole tube in batch mode but with recirculation of 5 mM acetate from the reservoir at a flow rate of 3 mL min^{-1}, according to equation 7.1 (Liu and Logan, 2004).

$$\epsilon_c = \frac{C_{gen}}{C_{th}} \qquad \textit{Eq. 7.1}$$

Where; coulombs generated (C_{gen}) were determined by integrating current produced over the time it took to deplete the substrate and theoretical coulombs (C_{th}) were calculated considering that 8 moles of electrons would be released by complete degradation of 1 mole of acetate and 96485.34 coulombs of charge will be present in 1 mole of electrons.

Cyclic voltammetry (CV) was performed as described in section 3.2.3.2 after the power curve measurement was finished. The average oxidation peak current value was calculated by

dividing the oxidation peak current obtained from the CV to the number of MFCs that were connected in parallel (in the case of only one MFC, the dividend was 1).

7.2.4 Graphical analysis of multi-module MFC start-up

The voltage rise during start-up of all MFCs in the multi-module tube was plotted and observed. The curves were split into four different phases of start-up *viz.* lag phase, slow rise phase, fast rise phase and stabilisation phase and the time taken during each phase was also noted and termed t_{lag}, $t_{s.r.}$, $t_{f.r.}$ and t_{stbl}, respectively (Figure 7.3), for each MFC and; the total time taken to reach a plateau t_{total}, was summed as in Eq. 7.2.

$$t_{total} = \sum\left(t_{lag} + t_{s.r.} + t_{f.r.} + t_{stbl}\right) \qquad \textit{Eq. 7.2}$$

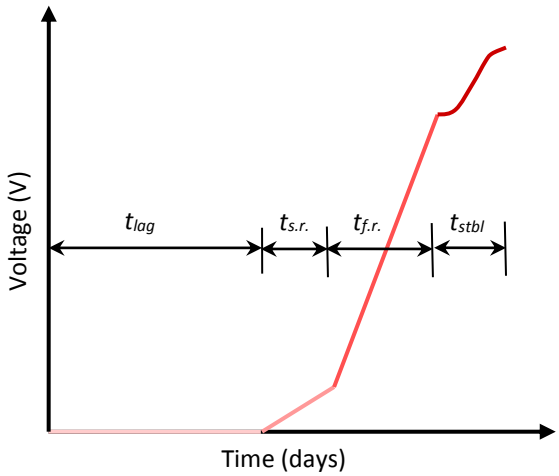

Figure 7.3: Proposed phases of start-up of MFCs in multi-module MFC.

Additionally, the slow rate of rise of voltage, $R_{s.r.}$ and fast rate of rise of voltage, $R_{f.r.}$ were also estimated for each of the MFCs.

Nonlinear regression was performed to obtain a linear relationship for t_{lag}, $t_{s.r.}$ and t_{total} and; exponential relationships for $R_{f.r.}$ and $R_{s.r.}$ against the position number of the MFC in the multi-module tube as per the following equations.

$$t_{phase} = m \cdot l + c \qquad \textit{Eq. 7.3}$$

$$R_{rise} = a \cdot e^{-b \cdot l} \qquad \textit{Eq. 7.4}$$

Where;

t_{phase} is t_{lag}, $t_{s.r.}$ or t_{total}, m is coefficient of phase time per module (day unit-length^{-1}), l is position of the MFC in multi-module MFC (unit-length), c is the intercept considered as bias time (day), R_{rise} is $R_{f.r.}$ or $R_{s.r.}$, a is coefficient of voltage rise (V day^{-1}) and b is normalisation factor for length (unit-lenth^{-1}). Here, only position of the MFC is considered in terms of the unit length instead of the actual distance of the MFC from the inlet as they were all identical and equispaced along the longitudinal length of the MFC. However, similar conclusions could be drawn using the actual position of an MFC from the inlet of multi-module MFC.

t_{stbl} was averaged over the 5 modules of MFCs as the stabilising period was not distinguishable (visually inspecting) for MFC-4 and MFC-5; and plotting t_{stbl} against the position of MFC curve seemed almost flat. Also, the voltage rise in stabilising period was assumed to be 0.025 V as 'rule of thumb' by visually comparing all the MFC start-up curves.

$t_{f.r.}$ was calculated using the relationships for t_{phase} and average value of t_{stbl}. Final value of voltage at steady state ($V_{steady-state}$) for the hypothetical MFC module positioned, at 10th twice the longer multi-module MFC tube than used in this study, was calculated as per the Eq. 7.5.

$$V_{steady-state} = (t_{s.r.} \cdot R_{s.r.}) + \left(t_{f.r.} \cdot R_{f.r.}\right) + 0.025\ V \qquad \textit{Eq. 7.5}$$

7.3 Results and discussion

7.3.1 Start-up of the multi-module tube MFC

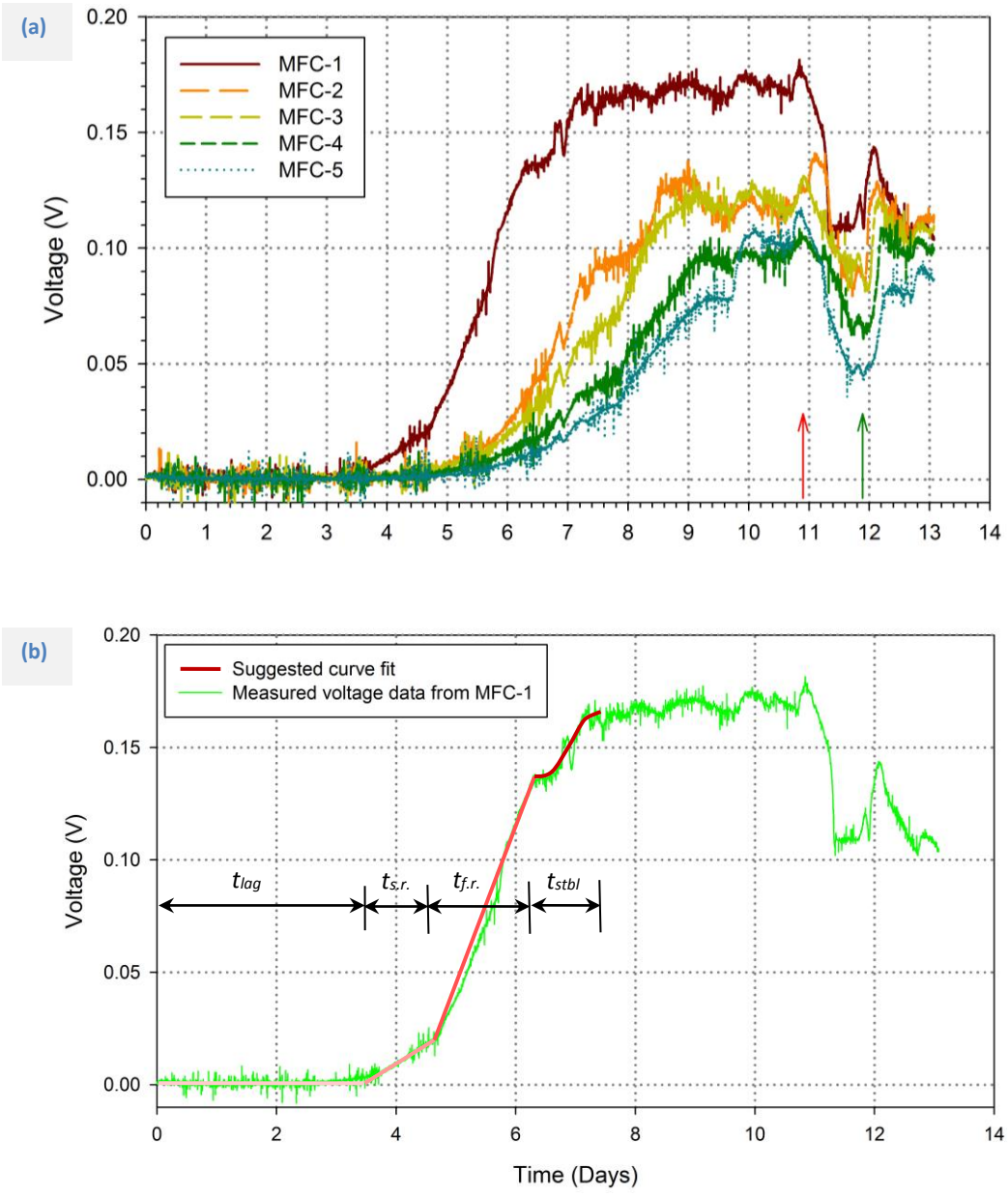

Figure 7.4: (a) Voltage plot showing the start-up of MFCs that are hydraulically in series and electrically independent. The red arrow shows when pump was stopped and green arrow shows when the pump was started again. The loads across each MFCs were 10 Ω. (b) Voltage plot showing start-up of MFC-1 and suggested curve fit to model the start-up of multi-module MFC.

Figure 7.4a shows voltage generation from 5 MFC modules placed in a multi-module tube. As an exemplar, Figure 7.4b shows the proposed typical phases of start-up of MFCs in such a multi-module MFC. The lag phase is considered the period during which no voltage is observed from the MFCs; the slow rise phase is considered when the voltage rise from the

MFC module is relatively slow compared to other phases described here apart from the lag phase; and similarly for the fast rise phase, when the voltage rise is rapid but with virtually constant rate, until it reaches the stabilising period. The stabilising period is considered when voltage from the MFC shows a sigmoidal response immediately after the fast rise phase.

The voltage plot in Figure 7.4a clearly shows a slower start-up of MFCs that are placed further from the inlet (MFC-1 being closest to the inlet). MFC-1 established steady-state voltage of 0.17 V with a start-up time (t_{total}) of 7.23 days, compared to the MFC-5 which reached to 0.11 V in 10.17 days. Oscillations in steady-state voltages are believed to be due to the daily temperature variations. The difference in steady-state voltages and the start-up times between two extreme MFCs (MFC-1 and MFC-5) is 0.06 V and 2.94 days which is 35.3% decrease in steady-state voltage and 40.7% increase in the start-up time which seems significant. Also, a trend toward lower steady-state voltage and increasing start-up time is observed as the position of MFC is increased from the inlet. This is clearly seen when time taken during each phase (described above) for each MFCs, and the rate of rise of voltage in each linear rise phases are plotted against the position of MFC in multi-module MFC (Figure 7.5). The reason for this phenomenon is not clear as the media waste-circulated with a concentration of 40 mM acetate at the start (as substrate), which is believed to be sufficient to be non-limiting. The hydraulic retention time (HRT) of the tube was 7.88 hours and all MFCs were also connected to the electrical load independently.

The MFC, anode connecting wires (soldered to the current collector) were longer for the MFC placed further from the inlet. The electrical resistance of the anode wire is 92 Ω km^{-1} as per the manufacturer's data sheet and so for a length of 210 mm, it would come to 0.019 Ω; which is clearly very small difference in electrical resistance to have a high impact on the start-up. The pressure due to fluid flow would be higher at the inlet end compared to the outlet end during the continuous feed of substrate via pumping. In the case of proton exchange membrane fuel cell (PEMFC), increased pressure would mean more mass of gaseous substrate would be available to anodes and cathodes but in the case of MFCs, the pressure was shown to have adverse effect on the performance (Cheng et al., 2014). The pressure may however, have affected the water permeation through the CEM, which was not investigated in this study.

When the pump was stopped on day 10.9, all MFCs voltages from MFC-1, MFC-2 and MFC-3 gradually dropped to 0.11 V, 0.9 V and 0.9 V, respectively in approximately half-a-day and; voltage from MFC-4 and MFC-5 dropped further to 0.07 V and 0.05 V in 0.7 day. A significant difference therefore, in steady-state voltages is also seen when the multi-module tube is in

batch mode without re-circulation of the media. The tube was placed at an angle of approximately 5° to maintain full liquid volume in the anode chamber, by allowing gasses to

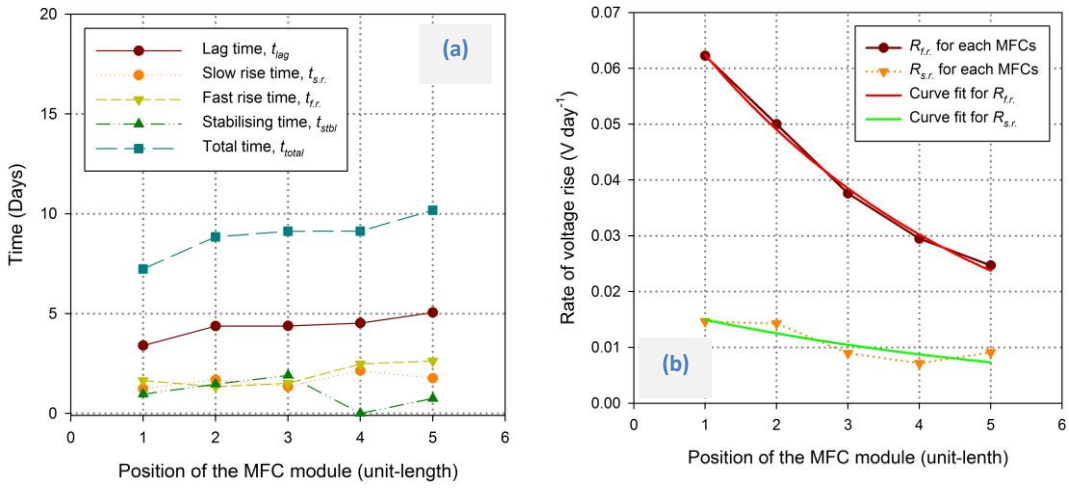

Figure 7.5: (a) Plot showing time duration of each phases of the start-up and (b) the rates of rise of voltage in linear rise phases from MFC-1, MFC-2, MFC-3, MFC-4 and MFC-5 when placed in their respective order from the inlet of multi-module MFC.

separate. This leads to a 20 mm static head between any two adjacent MFCs (anode length of 210 mm elevated at an angle of 5°) and would lead to pressure head of 2 cm of H_2O between two adjacent MFCs which seems quite an insignificant difference compared to the differences seen in voltage generation during day 11-12. When the pump was turned on again on day 11.9, voltages from all MFCs started rising again but they did not reach steady-state voltage as previously, except for the MFC-4. This may be due to substrate depletion. After replacing media and continuous operation showed that the difference in voltage generation from all MFC was not significant (within 0.05 V).

This could lead to one plausible explanation which is that the particulate of activated sludge could have accumulated by settling near the inlet of the multi-module tube and the MFC modules may have received different inoculum concentrations and possibly with different ecologies. There may be some dead zones near the inlet and also in the anodes which could have decelerated the flow sufficiently for sludge particulates to become immobile, which could have active archea and electrogenic components.

A linear trend is observed in t_{lag}, $t_{s.r.}$, $t_{f.r.}$ and t_{total} (Figure 7.5a) and exponential decay is observed in $R_{f.r.}$ and $R_{s.r.}$ against the position of MFC (Figure 7.5b). The relationships of $R_{f.r.}$ and $R_{s.r.}$ against the relative position of the MFC could also be represented by fitting a polynomial (such as linear, quadratic, etc), but such a fit would not represent the underlying physics and

the rates $R_{f.r.}$ and $R_{s.r.}$ would be negative at approximately 20th MFC in multi-module MFC that is 4-times the length (compared the tube fabricated in this study) which implies that the anode will be positive than the cathode. However in practice, it is believed that the anode will be negative relative to the cathode in an independently connected MFC and therefore, an exponential decay curve seems to be a good choice of curve fit for the rates which will tend to a steady-state value as MFC is placed further and further from the inlet. The values of constants in Eq. 7.3 and 7.4 are presented in Table 7.2.

Table 7.2: Values of coefficients of the equations for the curve fits.

	***m* (day unit-length^{-1})**	***c* (day)**	**R^2 value**
Curve fit for lag time, t_{lag}	0.345	3.309	0.837
Curve fit for slow voltage rise time, $t_{s.r.}$	0.152	1.174	0.441
Curve fit for total time, t_{total}	0.617	7.047	0.845
	a (V day^{-1})	**b (unit-lenth^{-1})**	**R^2 value**
Curve fit for $R_{f.r.}$	0.0795	0.2418	0.997
Curve fit for $R_{s.r.}$	0.0179	0.1789	0.758

When start-up time (t_{total}) and steady-state voltage ($V_{steady-state}$) for the MFC positioned 10th in a hypothetically twice long multi-module tube MFC, was calculated by using the obtained relationships, it appears that the start-up time could be 13.22 days which is nearly the double the time that required by MFC-1 and $V_{steady-state}$ for MFC-10 could be 0.054 V which is nearly 1/3rd of the voltage generated by MFC-1. It has to be emphasised here that the predicted values of start-up time and the steady-state voltages are not validated experimentally nor the model was validated beyond the data set available (MFC-1 to MFC-5 only). This could however, form a preliminary study into what delays there might occur in the start-up of MFCs, when they are deployed lengthwise hydraulically in series in the industry and if they would have any implication on the initial biofilm formation and the consequent power performances. After 1 month of continuous operation (fed-batch with re-circulation), the power production from all MFCs was 5.6 ± 0.7 mW. It is possible that even if the MFCs start-up time would be delayed along the length of the multi-module MFC, given sufficient time to develop and colonise the electrogens may reach their maximum power production capability.

Other strategy might be that the individual MFCs could be inoculated and fed hydraulically in parallel which may allow the MFCs to reach their full power production capability quicker than hydraulically in series (based on the experimental data of 5 MFCs in multi-module MFC).

7.3.2 Optimal hydraulic stack length of the MFC

Figure 7.6 shows the measured and estimated maximum power obtained from the MFC modules when their couples length is step-wise increased to 0.42, 0.63 and 0.84 m. The error bars show the variation of maximum power from duplicate measurements. To compare, an aggregated maximum power estimated from the same MFCs that were independently electrically connected is also presented (Figure 7.6).

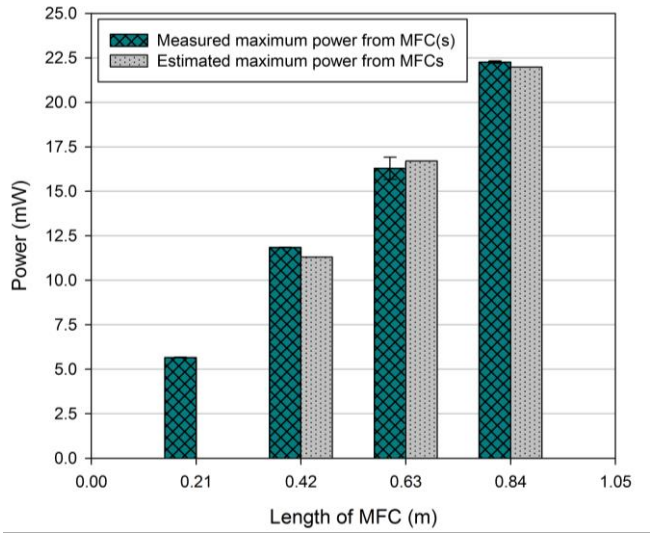

Figure 7.6: Measured and estimated maximum power from MFCs when MFC length varied from 0.21 m to 0.84 m in 0.21 m increment.

When all the MFC modules in the tube were electrically independently connected, the average maximum power measured from MFC-1, MFC-2, MFC-3 and MFC-4 was 5.67, 5.63, 5.40 and 5.33 mW, at 15.1 Ω, 13.2 Ω, 13.4 Ω and 18.2 Ω, respectively. In 2P-MFC, 3P-MFC and 4P-MFC, the average maximum power production was 11.85 mW, 16.29 mW and 22.26 mW, again respectively. This shows that the power from adjacent MFCs connected in parallel, i.e. increasing the tube length, did not affect the power available from individual MFC modules that were connected (MFC-1, MFC-2, MFC-3 and MFC-4). This is in contrast to the study by Kim et al. (2011a) where the power production seemed to have improved when connected independently compared to electrically connected in parallel. The lengths of MFCs are similar (230 mm compared to 210 mm in this study) to MFCs in Ref. (Kim et al., 2011a), but the anode

design, materials and the MEA are different. Anode used in this study is an optimised helical anode as discussed in Chapter 6 which offers more available surface area for anodic biofilm growth, optimised flow conditions for better substrate delivery and product removal from the electrode and also higher conductive carbon cloth anode all of which may affect the performance of hydraulic stack. Also, the flow rate studied here was approximately 10 times than that in Ref. (Kim et al., 2011a) which could mean that the substrate delivery to the successive MFCs hydraulically connected in line would have a higher concentration than that of when at lower flow rates, i.e. organic loading rate in this study is much higher than in previous study by Kim et al. (2011a).

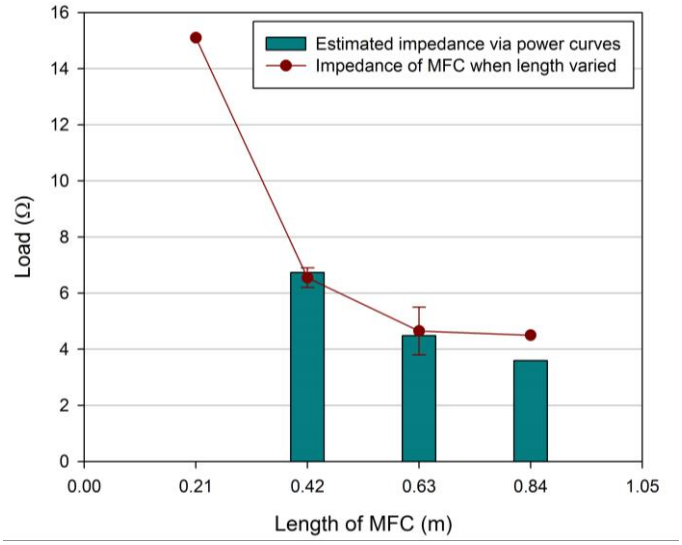

Figure 7.7: Estimated and measured impedance (Ω) from power curves when MFC length varied from 0.21 m to 0.84 m in 0.21 m increment.

In O1-MFC, 2P-MFC, 3P-MFC and 4P-MFC modes, the average impedance (load at which power was maximum) was found to be 15.1 Ω, 6.55 Ω, 4.65 Ω and 4.5 Ω, respectively (Figure 7.7). This shows that the impedances in 2P-MFC and 3P-MFC modes behaved similar to when the electrical resistors are connected in parallel. But, in 4P-MFC, the impedance was 0.82 Ω higher (22% approx.) than the estimated impedance assuming impedance from all MFCs in parallel. However, this did not have adverse effect on power as shown in Figure 7.6.

Carbon loading was found to be progressively higher on MFC-1 through to MFC-5 and also anodes that were placed were higher performing anodes progressively from inlet towards the outlet with highest performing anode (CP-HFC) nearest to the outlet. This could have offset the performance to higher from MFCs further from the inlet and altogether, similar power from all MFCs therefore was observed.

When identical power sources such as batteries are connected in parallel, generally voltages are averaged and electrical current is added. Here, by examining power curves obtained from individual MFCs (Figure 7.8), it appears that the internal resistances were similar and so all MFCs were considered identical in power. However, it did show lower power generations at higher current demand (lower electrical loadings) from succeeding MFCs in the multi-module tube perhaps due to mass transfer limitations and/or lower availability of substrate in successive MFCs (Kim et al., 2011a). So, it would be ideal to operate these MFCs at slightly higher loading than the impedance of individual MFCs which would allow all MFCs to be connected in series or parallel without any power losses.

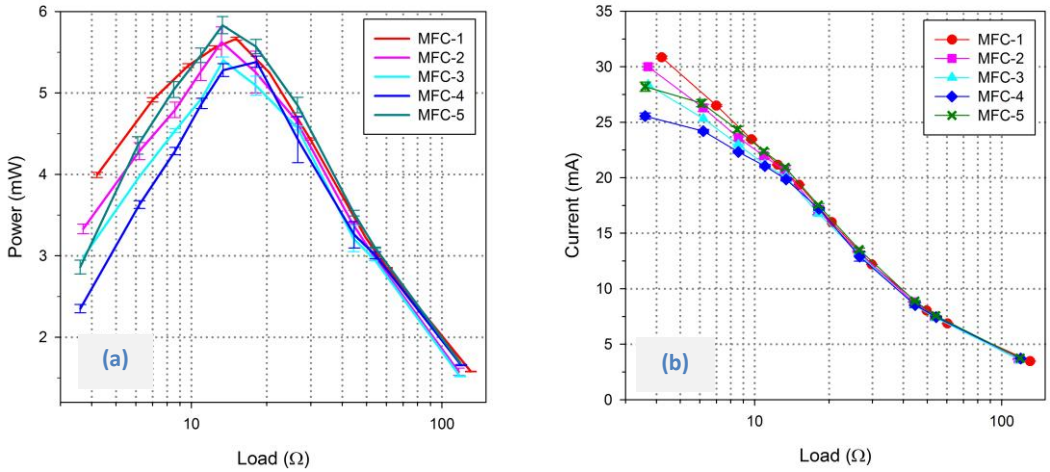

Figure 7.8: (a) Power curves (power against load) and (b) electric current measured from all MFCs in scaled-up tube. Error bars show deviation of measurement in power in (a) and current in (b) based on duplicate measurements at same values of loads.

7.3.3 Biocatalytic activity from different length of MFCs

When CV on O1-MFC, 2P-MFC2, 3P-MFC and 4P-MFC was performed, it appeared that the oxidation potential varied from -138 mV to -250 mV (Table 7.3). It is not clear why this variation has been seen but hypothetically, if two adjacent MFC anodes are operating at dissimilar anodic potentials, the current will flow internally from one MFC anode to the other when electrically connected together. This can be considered as parasitic current (Rismani-Yazdi et al., 2008) and would cause loss in power. In literature, the oxidation potential of acetate driven MFC has been reported to about -200 mV (Kim et al., 2006) and the oxidation values found in this study seems be closer to that. Also, Martin et al. (2013) observed two redox peaks, at around -330 mV and -170 mV vs. Ag/AgCl (saturated KCl, BASi), which they suggested to have occurred due to the dominant electrogens out of several species of

electrogens capable of transferring electrons. Measurement of CV on MFC-2, MFC-3 and MFC-4 anodes were difficult due to their position and placement of reference electrode close to these anodes was not possible without damaging the MEA. But, oxidation potential from anode in duplicate (set 1 and set 2) measurements with time delays of approximately 24 hours show significant difference. This however, did not seem to affect the power output as discussed in section7.3.2.

Table 7.3: Measured oxidation potential values (against Ag/AgCl electrode) from different lengths of MFCs.

MFC mode	Set 1 (mV)	Set 2 (mV)
O1-MFC	-165	-138
2P-MFC	-250	-227
3P-MFC	-225	-211
4P-MFC	-185	-213

The average oxidation peak current from anodes with different lengths as in O1-MFC, 2P-MFC, 3P-MFC and 4P-MFC were 127 mA, 161 mA, 320 mA and 452 mA, respectively. When the average oxidation peak current was normalised to the number of anodes connected, it seems that the oxidation peak current was maximum in O1-MFC a trend in slight increase in oxidation peak current was found when MFC length was increased from 0.42 m to 0.63 m and further to 0.84 m (Figure 7.9). In fact, the experiment was performed in chronological order to

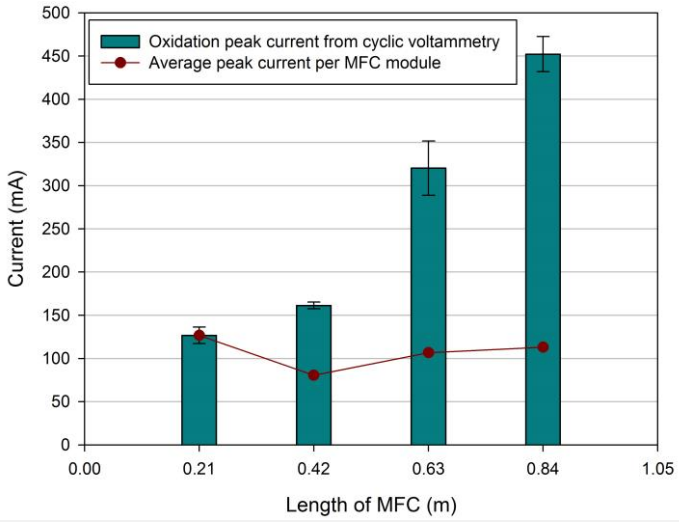

Figure 7.9: The plot showing oxidation peak current measured via cyclic voltammetry and average peak current per MFC module when MFC length varied from 0.21 m to 0.84 m in 0.21 m increment.

test for the 2P-MFC, 3P-MFC, 4P-MFC and O1-MFC, respectively. This could imply that the biofilm may still be growing during the experiment. The estimated power in section 7.3.2 for

2P-MFC, 3P-MFC and 4P-MFC was estimated using the power obtained in O1-MFC mode and it is possible that mode 2P-MFC, 3P-MFC and 4P-MFC could have probably produced slightly higher performance if it was measured after O1-MFC.

So, the up-scaling of MFC was demonstrated through the multi-module MFC that was fabricated to accommodate 5 MFCs hydraulically in series, all sharing a common cation exchange membrane and operated on acetate as the substrate. The equivalent power production from first 4 modules (from the inlet end) when they were connected together to create an effective continuous MFC of 0.84 m, matched with the power production from their electrically independent operation which suggests that with considering the design presented in this study, employing the helical anodes, can be fabricated with a longer length (of up to 0.84 m). However, this would need to be verified through their operation on real wastewater. The system produced the power of 5.61 ± 0.70 mW, i.e. 19.75 ± 2.47 W m^{-3} and considering a system that has 50 MFCs, it could potentially produce 280.5 mW and storing this energy for 24 hours, could give around 6.7 Wh of energy. This may not seem like much but it can be enough for powering the monitoring equipments through such as ultra-low power, energy saving microcontrollers. Bearing in mind that the aeration is eliminated in the MFC process, minimal energy spent on pumping where gravity fed mode can be utilised and the system's self-monitoring through its own generated power, this technology may have future in wastewater treatment industry. However, further enhancement in power is probably needed for the cost effectiveness of their deployment and operation.

7.3.4 Remarks on up-scaled multi-module MFC prototype

During continuous operation of the multi-module MFC, the large amount of salt appeared and accumulated on the cathode which seemed the likelihood of its travel through the membrane as shown in the photo in Figure 7.10. The collected salt weighed approximately 12.7 g in 11 days. Based on the measurements of volatile fatty acids (VFAs) on the salt as described by Cruwys et al. (2002) using the gas chromatograph (HS40XL Perkin Elmer, MA, USA), an average value of 27 mg L^{-1} was found and showed that the acetate content present in the salt was minimal although the feed was 2.36 g L^{-1} (The salt was diluted with 1:10 w/w ratio in deionised water for the measurements). It is believed that since the membrane utilised in the MFC was cation exchange membrane, the salt coming through the membrane could be rich in sodium (Gajda et al., 2014) or cations (Rabaey, 2009) that are present in the phosphate buffer which can be collected and recycled. Additionally, this salt formation accumulated into the electrical connection of the crocodile clip to the cathode which resulted in poor

conductivity and therefore the connection needed to be soldered or protected by applying adhesive/rubber coating on top of the electrical connection.

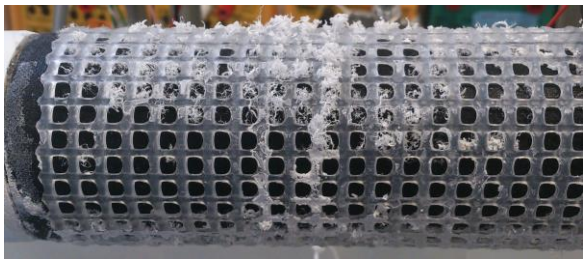

Figure 7.10: Photo showing salt formation/excretion on to the cathode of MFC.

The coulombic efficiency from multi-module MFC was found to be 89% when 5 mM of acetate was re-circulated through the media reservoir with total volume of 3.6 L. This shows that 89% of the energy in wastewater was recovered in terms of electricity. But, the coulombic efficiency may be lower when operated with real wastewater (Zhuang et al., 2012b).

8. Discussion

The automated start-up as demonstrated in Chapter 3 proved to be successful in terms of reaching the peak power in relatively short time. This approach such as in MFC-MPPT can be considered 'plug & play' where the MFC was provided with an MPPT load which was able to start as well as maintain the optimum load after the start-up, requiring less maintenance as far as the up-scaling of the MFC system is considered. Here, the MPPT loads were the electrical resistors which meant that the power was lost in terms of heat and the controlling processor was a personal computer. The future application however, could be implemented through the use of ultra-low power consuming microcontrollers which can be employed to do the Boolean based decisions and control the load (Boghani et al., 2014). The resistive loads can also be replaced by the low voltage DC/DC boosters such as presented by Weidong et al. (2004).

The MPPTs showed oscillations in tracking of the peak power which are due to the load steps and parsimonious nature of the control. Fast convergence can be obtained by combing voltage control or current sourcing using the piecewise linearised models as exemplified in Chapter 4. Another possibility would be to periodically measure the power curve and maintain an optimum load or voltage at which the MPP exists until unless drastic change in other operational parameters such as pH, temperature or OLR is observed. Although the identification was performed on a flat-type reactor, it is believed that the strategies and methodologies can be transferrable to other types of MFC architecture, too.

Voltage reversal was successfully avoided by providing bypass routes for the electrical current using hybrid series stack connectivity. One would argue that this led to an operation that can be identical to their electrically independent performances. It should be noted that since the MFCs were interconnected, upon an instance where one of the MFCs underperforms or all of the MFCs are operated at different power levels, the 'bridging' in stack connection can provide a passive control mechanism, delivering the current to the cells where required. While this approach avoided the voltage reversal, it was not investigated however, if the stack voltage could be utilised. It would need further investigation before its implementation.

The modeling techniques utilised in Chapter 6 were proved to be effective in assisting the design of anode geometry for the enhancement in power from the MFC. When these anodes were connected hydraulically in series together (multi-module MFC), the evidence showing minimal power loss suggests that the MFC may not have suffered problems such as cross conduction as others have found (Zhuang and Zhou, 2009). This may be due to improved

mass transfer using relatively better mixing due to the helical fluid channels in this study compared to their reactors employing plug flow. It could also mean that the length of the MFC could be increased further to the point that the power loss would be evident. Highly mixed system could be beneficial when operating on real wastewater where the conductivity can be limited and the ionic transport can be facilitated using convective or advective flow. The CP-HFC showed better capability in transport of product (H^+) from the anode towards the fluid channel and it could result in replenishing with a more mixed fluid from the surrounding. This may help electrogens perform well under limited buffering conditions. The high input energy in terms of pumping due to the addition of 'converging plates' was implicated by analysis of pressure but this is expected to be compensated by a recommendation presented in section 6.3.2.4 and it should be verified through the experiments. Also, buffering used in the experiments in this study was phosphate based. A less expensive alternative of carbonate based buffering (Rinaldi et al., 2008) should be considered in future implementation of the MFC system and the ionic conductivity could be achieved through the addition of salts such as NaCl. Likewise, The cathodes used in demonstration of scaled-up system utilised Pt cathode and, the future implementation of MFC system in treatment of real wastewater would need to consider a more sustainable but similar performing catalysts.

Based on the conclusions for Chapter 3 and the MPP load observed for the single module MFCs in Chapter 6, the load value of 10 Ω was chosen for the loading during the start-up of multi-module MFCs. Since, there was no control (MFC start-up at higher load than 10 Ω), it cannot be said if the MFCs started-up earlier but, the characteristic 'power undershoot' was not observed (Figure 7.8) when power curve was measured after the voltage rise. It was though, observed in single module MFC (HFC, P-HFC and CP-HFC) during their early stages of power development (Figure 6.6) since the MPPT on single modules was not able to apply the electrical load of lower than 17.8 Ω. This shows that the automated start-up strategy developed was transferable to significantly different design of MFCs. While it was evident that the MFCs in multi-module exhibited delayed start-up according to its position in the multi-module tube, the maximum power from all MFCs matched after 1 month of operation. Also, there was no validation performed for the analysis showed in section 7.3.1, so, it cannot be concluded if further modules were added to the multi-module MFC (longer), the trend would carry on unless otherwise validated by the experimentation. However, this possibility of delayed start-up or possibly no start-up at all from the further placed MFC in the multi-module tube cannot be ruled out, and shall be investigated further as it may find some industrial relevance.

A simpler MPPT algorithm was employed on the multi-module MFC reactor which looked at the slope of power vs. voltage where the load was increased if slope was positive and decreased if the slope was negative. This demonstrated that the MPPT applied continual demand on the MFC to produce maximum power (Figure 8.1) and the power seemed to match the potentiostatic measurements. The MFCs were fed with 40 mM acetate at flow rate of 3 mL min^{-1} and operated at ambient temperature of 22 ± 3 °C.

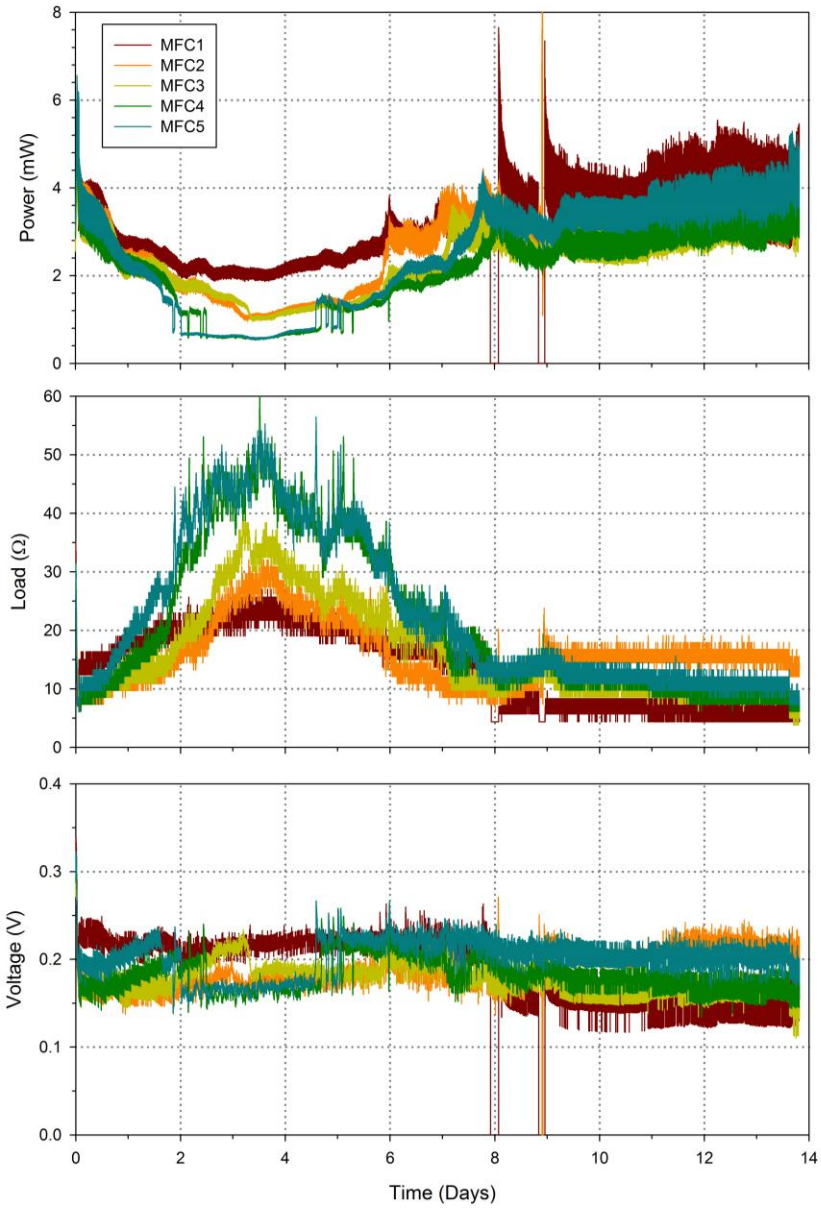

Figure 8.1: MPPT on multi-module MFC where the peak power point tracking is evidenced through the power and load plots due to variation in current.

9. Conclusions and future prospects

9.1 Conclusions

MFCs/BESs rely on the natural attachment of the electrogens to their anodes and providing the favourable conditions for their colonisation on the anode can enhance the power and enhance the system start-up time. PP-MPPT and MPPT loaded (electrical) MFC, as demonstrated on H-type MFCs; started-up in 23 days compared to the statically loaded (electrical) MFC which started in 42 days, thereby reducing the start-up time by 45% without compromising the power performance. PP-MPPT and MPPT applied lower loading than that of the MPP load (determined when fully operational) during the start-up, and that suggested that the acclimation of electrogens is favourable at higher current sourcing (lower loads) than at a relatively lower current sourcing (higher loads). PP-MPPT and MPPT loaded MFCs did not show power overshoot or undershoot at higher current loading in contrast to the statically loaded MFC, demonstrating that the underperformance of the MFC could be avoided by applying MPPT on MFCs. Also, the biocatalytic activity, as inferred by the CVs, from MFC-PP-MPPT and MFC-MPPT was 3.5-fold higher than the MFC-*Control* which was enriched with two static loads (1 kΩ until day 42 and then 500 Ω). So, the performance of MFC could be improved by control of current sourcing to operate the MFC at its MPP in real-time using MPPT.

System identification tools were found to be applicable to the MFC systems and wide range of operation (electrical loads) was investigated on a flat-type MFC through the parameter estimation applied to alternative model structures. The MFC system was piecewise linearised and represented by series of linear input (electrical load) – output (voltage) process models of 1st order structure for most input electrical loading (current sourcing) conditions. The time constants 1st order process models gradually increased from 0.5 s to 6.2 s with an increase in loading steps from lower loading step of 100 Ω - 150 Ω to higher loading step of 950 Ω - 1 kΩ and therefore, evidenced the nonlinearity and exhibited slower dynamics as the MPP was approached. The MFC system was found to be better represented by the 4th order ARX model structures near the loading region of MPP and the ARX models were best fit to the validation data but, for practical purposes such as control of voltage, power or current; it is likely that the lower order i.e. 1st order process models would likely represent the system adequately. By assembling series of linear models representing the full range of operation, could represent the MFC system which can be utilised for control purposes.

The practical uses of power from MFCs would require voltages to be increased above cell voltages which are only around 0.5 V, and this can be achieved by stacking the MFCs electrically in series. This approach however, jeopardises the MFCs with occurrence of voltage reversals in the case of feed or power imbalance and affects the whole stack. The connection strategy presented in this study, along with the application of MPPT can avoid the voltage reversal while extracting the maximum power from each MFCs in real-time.

The performance of MFC needs to be increased for their applicability and their practical uses such as in the treatment of wastewaters to minimise the cost of running the process and also increase the sustainability. Optimisation of the anode was sought through the finite element method modeling of the anode geometry to look at fluid flow and the effected mass transport. The modeling results suggested that the CP-HFC would facilitate removal of products from the anode electrode better than that of the P-HFC and HFC by creating differential pressure between the anode and the fluid channel using converging plates and accelerating the fluid near the anode electrode surface and in the centre of the fluid channel. Experimental results supplemented the modeling results whereby, the CP-HFC produced higher power (13.82, 13.90 and 20.88 W m^{-3}) than that of the P-HFC (6.92, 9.57 and 15.89 W m^{-3}) and HFC (3.95, 5.66 and 17.04 W m^{-3}) at all the flow rates that were tested (1, 3 and 8 mL min^{-1}) while keeping the OLR constant of 33.98 g L^{-1} day^{-1} and it demonstrated the importance of mixing and that the further optimisation is possible through the reactor design. This is particularly useful when a long tubes of MFCs would need to be deployed to achieve the capacity of the wastewater treatment plant and the performance of the MFC would need to be consistent or at least optimum throughout the length of the MFC.

Up-scaling of MFC system targeting for the treatment of wastewater was considered by lengthwise increasing the number of modules, projecting the multiplication of the tubes to achieve the capacity of the treatment plant. The up-scaling of MFCs was demonstrated through the multi-module MFC that was fabricated to accommodate 5 MFCs hydraulically in series utilising 2 × HFC, 2 × P-HFC and 1 × CP-HFC anodes and air cathodes, all sharing a common cation exchange membrane and subsequently operated on acetate as the substrate. The start-up of individual MFCs showed delay as they were placed further away from the inlet end but after continuous operation of MFC for at least 1 month similar power generation from all MFCs was achieved (5.61 ± 0.70 mW, i.e. 19.75 ± 2.47 W m^{-3}). The power production from first 4 modules when they were connected together to create an effective continuous MFC of 0.84 m, matched with the power production from the independent MFC modules that it

consisted of and so, the MFC of the design presented in this study, employing the helical anodes can be fabricated up to 0.84 m long providing that similar trend is observed when operating the presented MFC on real wastewater.

So, this study presented a series of optimisation and control mechanisms for the MFC system, which can be applied to enhance its performance and it can find its utility in various applications such as treatment of wastewater and with some tailoring, in hydrogen production, desalination, metal recovery from wastewater and also bio-sensing.

9.2 Future prospects

Several possibilities of further enhancement in understanding and improvement in the MFC system can be recommended upon the presented work, other than what has already been recommended in the relevant sections for the studies, are listed below.

- ⇒ From the biological point of view, the anodic biofilm obtained with PP-MPPT and MPPT loaded MFCs can be compared with the statically loaded MFC using molecular analysis techniques which can provide insight into understanding the difference and similarities of the bacterial community so obtained. This information can be further utilised to better engineer the anode in terms of colonising the MFC with selective bacteria to create 'plug and play' MFC and create a robust biofilm that may withstand the environmental influence to produce stable and enhanced power.
- ⇒ The identification of parameters of series of linear models representing the MFC system was performed offline as a demonstration purpose but for real-time application, more accurate and ever changing parameters can be determined and tracked using recursive identification methodologies that are widely known and available.
- ⇒ The connection strategy proved to be successful in avoiding the voltage reversal also an increase in stack voltage was seen. However, the stack voltage was not utilised to drive the load and it was the resultant of the stack of the loads that was connected to the MFC stack. Further studies need to be carried out on re-engineering of this strategy so that the stack voltage can be utilised to drive a load or for storing the energy in alternative systems such as conventional chargeable batteries with minimal loss of electrical current avoiding the voltage reversal in the stack operation.
- ⇒ MPPT controllers used in this study were for the demonstration purposes and the field application of such controllers can be achieved through the commercially available

ultra-low microcontrollers, which use minimal power in the standby mode and can be driven through the power harvested by the MFC system.

⇒ The multiphysics modeling of the MFC should be performed, which will include the ion exchange membrane and the cathode and also the electrochemistry and biological reactions that may be happening in the anode of the MFC. This would provide a tool for better designing the system for improvement in the power production and the efficiency.

⇒ The multi-module MFC should be extended further and the start-up of the modules of MFCs should be experimented to determine whether there is likelihood of dropping of performance permanently due to the slow start-up of MFCs which are placed further along the length of the long MFC tube (multi-module MFC).

⇒ Experimentation on multi-module MFC should be carried on further than that of four modules to determine at which length the MFC is likely to exhibit the power losses and therefore the cutting point of single long module of the MFC.

⇒ The MEA of multi-module MFC had weakened after 5 months of operation and the leakage of water appeared from the overlapping joint of the CEM. Further recommendation for the MEA would be to form a tube by overlapping the CEM twice around the tube as shown in the Figure 9.1 that would make it difficult for the water to travel through such a large distance and the water would need to be at much higher pressure to flow through the micro-gaps (if formed) rather than flowing through the main fluid channel, i.e. helical flow path.

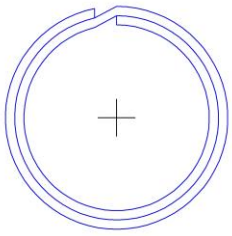

Figure 9.1: Cross sectional view of the proposed CEM tube manufacturing.

⇒ In practice, it is recommended that if MFCs are gravity-fed, the MFC should be kept inclined with the inlet being at the lower end of the MFC. This is because if the MFC was fed from the top end rather than bottom end, on becoming the outflow greater than the inflow, an air gap would form at the top end (assuming that the gas produced in the anode which fills the vacuum created by the difference in outflow and inflow

and/or if some leakages in MEA are present) hence the anode chamber would be partially filled only, rather than fully filled.

⇒ And lastly without a doubt, the multi-module MFC should be operated on real wastewater and its field application should be considered to determine its behaviour and efficacy when operated on real wastewater.

10. References

AELTERMAN, P., RABAEY, K., PHAM, H. T., BOON, N. & VERSTRAETE, W. 2006. Continuous Electricity Generation at High Voltages and Currents Using Stacked Microbial Fuel Cells. *Environmental Science & Technology,* 40**,** 3388-3394.

AELTERMAN, P., VERSICHELE, M., MARZORATI, M., BOON, N. & VERSTRAETE, W. 2008. Loading rate and external resistance control the electricity generation of microbial fuel cells with different three-dimensional anodes. *Bioresource Technology,* 99**,** 8895-8902.

AGENCY, I. E. 2013. *International Energy Outlook 2013 (IEO2013)* [Online]. International Energy Agency. Available: http://www.eia.gov/forecasts/ieo [Accessed 18/06/2014 2014].

AJAYI, F. F., KIM, K.-Y., CHAE, K.-J., CHOI, M.-J. & KIM, I. S. 2010. Effect of hydrodymamic force and prolonged oxygen exposure on the performance of anodic biofilm in microbial electrolysis cells. *International Journal of Hydrogen Energy,* 35**,** 3206-3213.

ALLEN, R. M. & BENNETTO, H. P. 1993. Microbial fuel-cells: Electricity production from carbohydrates. *Applied Biochemistry and Biotechnology,* 39-40**,** 27-40.

BOERO, M., IKESHOJI, T. & TERAKURA, K. 2005. Density and Temperature Dependence of Proton Diffusion in Water: A First-Principles Molecular Dynamics Study. *ChemPhysChem,* 6**,** 1775-1779.

BOGHANI, H. C., KIM, J. R., DINSDALE, R. M., GUWY, A. J. & PREMIER, G. C. 2013. Control of power sourced from a microbial fuel cell reduces its start-up time and increases bioelectrochemical activity. *Bioresource Technology,* 140**,** 277-285.

BOGHANI, H. C., PAPAHARALABOS, G., MICHIE, I., FRADLER, K. R., DINSDALE, R. M., GUWY, A. J., IEROPOULOS, I., GREENMAN, J. & PREMIER, G. C. 2014. Controlling for peak power extraction from microbial fuel cells can increase stack voltage and avoid cell reversal. *Journal of Power Sources,* 269**,** 363-369.

BONANNI, P. S., SCHROTT, G. D., ROBUSCHI, L. & BUSALMEN, J. P. 2012. Charge accumulation and electron transfer kinetics in Geobacter sulfurreducens biofilms. *Energy & Environmental Science,* 5**,** 6188-6195.

BOROLE, A. P., AARON, D., HAMILTON, C. Y. & TSOURIS, C. 2010. Understanding Long-Term Changes in Microbial Fuel Cell Performance Using Electrochemical Impedance Spectroscopy. *Environmental Science & Technology,* 44**,** 2740-2745.

BOROLE, A. P., HAMILTON, C. Y., VISHNIVETSKAYA, T. A., LEAK, D., ANDRAS, C., MORRELL-FALVEY, J., KELLER, M. & DAVISON, B. 2009. Integrating engineering design improvements with exoelectrogen enrichment process to increase power output from microbial fuel cells. *Journal of Power Sources,* 191**,** 520-527.

BRANDT, M. J., MIDDLETON, R. A. & WANG, S. 2010. Energy efficiency in the water industry: A compendium of best practices and case studies - Global report. Global Water Research Coalition.

CAO, X., HUANG, X., LIANG, P., XIAO, K., ZHOU, Y., ZHANG, X. & LOGAN, B. E. 2009. A New Method for Water Desalination Using Microbial Desalination Cells. *Environmental Science & Technology,* 43**,** 7148-7152.

CHANG, I. S., JANG, J. K., GIL, G. C., KIM, M., KIM, H. J., CHO, B. W. & KIM, B. H. 2004. Continuous determination of biochemical oxygen demand using microbial fuel cell type biosensor. *Biosensors and Bioelectronics,* 19**,** 607-613.

CHEN, S., HOU, H., HARNISCH, F., PATIL, S. A., CARMONA-MARTINEZ, A. A., AGARWAL, S., ZHANG, Y., SINHA-RAY, S., YARIN, A. L., GREINER, A. & SCHRODER, U. 2011. Electrospun and solution blown three-dimensional carbon fiber nonwovens for application as electrodes in microbial fuel cells. *Energy & Environmental Science,* 4**,** 1417-1421.

CHENG, K. Y., HO, G. & CORD-RUWISCH, R. 2008. Affinity of Microbial Fuel Cell Biofilm for the Anodic Potential. *Environmental Science & Technology,* 42**,** 3828-3834.

CHENG, S., LIU, H. & LOGAN, B. E. 2005. Power Densities Using Different Cathode Catalysts (Pt and CoTMPP) and Polymer Binders (Nafion and PTFE) in Single Chamber Microbial Fuel Cells. *Environmental Science & Technology,* 40**,** 364-369.

CHENG, S., LIU, H. & LOGAN, B. E. 2006. Increased performance of single-chamber microbial fuel cells using an improved cathode structure. *Electrochemistry Communications,* 8**,** 489-494.

CHENG, S., LIU, W., GUO, J., SUN, D., PAN, B., YE, Y., DING, W., HUANG, H. & LI, F. 2014. Effects of hydraulic pressure on the performance of single chamber air-cathode microbial fuel cells. *Biosensors and Bioelectronics,* 56**,** 264-270.

CHENG, S. & LOGAN, B. E. 2007. Ammonia treatment of carbon cloth anodes to enhance power generation of microbial fuel cells. *Electrochemistry Communications,* 9**,** 492-496.

CHOI, C. & CUI, Y. 2012. Recovery of silver from wastewater coupled with power generation using a microbial fuel cell. *Bioresource technology,* 107**,** 522-525.

CLAUWAERT, P., RABAEY, K., AELTERMAN, P., DE SCHAMPHELAIRE, L., PHAM, T. H., BOECKX, P., BOON, N. & VERSTRAETE, W. 2007. Biological denitrification in microbial fuel cells. *Environmental science & technology,* 41**,** 3354-3360.

CRUWYS, J., DINSDALE, R., HAWKES, F. & HAWKES, D. 2002. Development of a static headspace gas chromatographic procedure for the routine analysis of volatile fatty acids in wastewaters. *Journal of Chromatography A,* 945**,** 195-209.

DÁVILA, D., ESQUIVEL, J. P., SABATÉ, N. & MAS, J. 2011. Silicon-based microfabricated microbial fuel cell toxicity sensor. *Biosensors and Bioelectronics,* 26**,** 2426-2430.

DEGRENNE, N., BURET, F., MOREL, F., ADAMI, S.-E., LABROUSSE, D., ALLARD, B. & ZAOUI, A. Year. Self-starting DC:DC boost converter for low-power and low-voltage microbial electric generators. *In:* Energy Conversion Congress and Exposition (ECCE), 17-22 Sept 2011 USA. IEEE, 889-896.

DEKKER, A., HEIJNE, A. T., SAAKES, M., HAMELERS, H. V. & BUISMAN, C. J. 2009. Analysis and improvement of a scaled-up and stacked microbial fuel cell. *Environmental science & technology,* 43**,** 9038-9042.

DI LORENZO, M., CURTIS, T., HEAD, I., VELASQUEZ-ORTA, S. & SCOTT, K. 2009a. A single chamber packed bed microbial fuel cell biosensor for measuring organic content of wastewater. *Water Science & Technology,* 60**,** 2879-2887.

DI LORENZO, M., CURTIS, T. P., HEAD, I. M. & SCOTT, K. 2009b. A single-chamber microbial fuel cell as a biosensor for wastewaters. *Water Research,* 43**,** 3145-3154.

DI LORENZO, M., SCOTT, K., CURTIS, T. P. & HEAD, I. M. 2010. Effect of increasing anode surface area on the performance of a single chamber microbial fuel cell. *Chemical Engineering Journal,* 156**,** 40-48.

DI LORENZO, M., SCOTT, K., CURTIS, T. P., KATURI, K. P. & HEAD, I. M. 2009c. Continuous feed microbial fuel cell using an air cathode and a disc anode stack for wastewater treatment. *Energy & Fuels,* 23**,** 5707-5716.

DI LORENZO, M., THOMSON, A. R., SCHNEIDER, K., CAMERON, P. J. & IEROPOULOS, I. 2014. A small-scale air-cathode microbial fuel cell for on-line monitoring of water quality. *Biosensors and Bioelectronics,* 62**,** 182-188.

DU, Z., LI, H. & GU, T. 2007. A state of the art review on microbial fuel cells: A promising technology for wastewater treatment and bioenergy. *Biotechnology Advances,* 25**,** 464-482.

EMMANOUILIDES, C. & PETROU, L. 1997. Identification and control of anaerobic digesters using adaptive, on-line trained neural networks. *Computers & Chemical Engineering,* 21**,** 113-143.

ERABLE, B., RONCATO, M.-A., ACHOUAK, W. & BERGEL, A. 2009. Sampling Natural Biofilms: A New Route to Build Efficient Microbial Anodes. *Environmental Science & Technology,* 43**,** 3194-3199.

FAN, Y., HU, H. & LIU, H. 2007. Enhanced Coulombic efficiency and power density of air-cathode microbial fuel cells with an improved cell configuration. *Journal of Power Sources,* 171**,** 348-354.

FAN, Y., XU, S., SCHALLER, R., JIAO, J., CHAPLEN, F. & LIU, H. 2011. Nanoparticle decorated anodes for enhanced current generation in microbial electrochemical cells. *Biosensors and Bioelectronics,* 26**,** 1908-1912.

FINKELSTEIN, D. A., TENDER, L. M. & ZEIKUS, J. G. 2006. Effect of Electrode Potential on Electrode-Reducing Microbiota. *Environmental Science & Technology,* 40**,** 6990-6995.

FORNERO, J. J., ROSENBAUM, M., COTTA, M. A. & ANGENENT, L. T. 2008. Microbial fuel cell performance with a pressurized cathode chamber. *Environmental science & technology,* 42**,** 8578-8584.

FRADLER, K. R., KIM, J. R., SHIPLEY, G., MASSANET-NICOLAU, J., DINSDALE, R. M., GUWY, A. J. & PREMIER, G. C. 2014a. Operation of a bioelectrochemical system as a polishing stage for the effluent from a two-stage biohydrogen and biomethane production process. *Biochemical Engineering Journal,* 85**,** 125-131.

FRADLER, K. R., MICHIE, I., DINSDALE, R. M., GUWY, A. J. & PREMIER, G. C. 2014b. Augmenting Microbial Fuel Cell power by coupling with Supported Liquid Membrane permeation for zinc recovery. *Water Research,* 55**,** 115-125.

FREGUIA, S., RABAEY, K., YUAN, Z. & KELLER, J. 2008. Sequential anode–cathode configuration improves cathodic oxygen reduction and effluent quality of microbial fuel cells. *Water Research,* 42**,** 1387-1396.

GAJDA, I., GREENMAN, J., MELHUISH, C., SANTORO, C., LI, B., CRISTIANI, P. & IEROPOULOS, I. 2014. Water formation at the cathode and sodium recovery using Microbial Fuel Cells (MFCs). *Sustainable Energy Technologies and Assessments,* 7**,** 187-194.

GOSTICK, J. T., FOWLER, M. W., PRITZKER, M. D., IOANNIDIS, M. A. & BEHRA, L. M. 2006. In-plane and through-plane gas permeability of carbon fiber electrode backing layers. *Journal of Power Sources,* 162**,** 228-238.

GREENMAN, J., IEROPOULOS, I. & MELHUISH, C. 2011. Microbial Fuel Cells - Scalability and their Use in Robotics. *In:* ELIAZ, N. (ed.) *Applications of Electrochemistry and Nanotechnology in Biology and Medicine I.* Springer.

GUSTAVSSON, I. 1975. Survey of applications of identification in chemical and physical processes. *Automatica,* 11**,** 3-24.

HA, P. T., MOON, H., KIM, B. H., NG, H. Y. & CHANG, I. S. 2010. Determination of charge transfer resistance and capacitance of microbial fuel cell through a transient response analysis of cell voltage. *Biosensors and Bioelectronics,* 25**,** 1629-1634.

HARNISCH, F., SCHRÖDER, U. & SCHOLZ, F. 2008. The suitability of monopolar and bipolar ion exchange membranes as separators for biological fuel cells. *Environmental science & technology,* 42**,** 1740-1746.

HE, Z. & MANSFELD, F. 2009. Exploring the use of electrochemical impedance spectroscopy (EIS) in microbial fuel cell studies. *Energy & Environmental Science,* 2**,** 215-219.

HE, Z., MINTEER, S. D. & ANGENENT, L. T. 2005. Electricity Generation from Artificial Wastewater Using an Upflow Microbial Fuel Cell. *Environmental Science & Technology,* 39**,** 5262-5267.

HOBBS, D. M. & MUZZIO, F. J. 1997. The Kenics static mixer: a three-dimensional chaotic flow. *Chemical Engineering Journal,* 67**,** 153-166.

HONG, Y., CALL, D. F., WERNER, C. M. & LOGAN, B. E. 2011. Adaptation to high current using low external resistances eliminates power overshoot in microbial fuel cells. *Biosensors and Bioelectronics,* 28**,** 71-76.

HUANG, J., YANG, P., GUO, Y. & ZHANG, K. 2011. Electricity generation during wastewater treatment: An approach using an AFB-MFC for alcohol distillery wastewater. *Desalination,* 276**,** 373-378.

IEROPOULOS, I., WINFIELD, J. & GREENMAN, J. 2010. Effects of flow-rate, inoculum and time on the internal resistance of microbial fuel cells. *Bioresource Technology,* 101**,** 3520-3525.

JADHAV, G. S. & GHANGREKAR, M. M. 2009. Performance of microbial fuel cell subjected to variation in pH, temperature, external load and substrate concentration. *Bioresource Technology,* 100**,** 717-723.

JURADO, F. 2004. Modeling SOFC plants on the distribution system using identification algorithms. *Journal of Power Sources,* 129**,** 205-215.

KATO MARCUS, A., TORRES, C. I. & RITTMANN, B. E. 2007. Conduction-based modeling of the biofilm anode of a microbial fuel cell. *Biotechnology and Bioengineering,* 98**,** 1171-1182.

KATURI, K. P. & SCOTT, K. 2010. Electricity generation from the treatment of wastewater with a hybrid up-flow microbial fuel cell. *Biotechnology and Bioengineering,* 107**,** 52-58.

KAUR, A., KIM, J. R., MICHIE, I., DINSDALE, R. M., GUWY, A. J. & PREMIER, G. C. 2013. Microbial fuel cell type biosensor for specific volatile fatty acids using acclimated bacterial communities. *Biosensors and Bioelectronics,* 47**,** 50-55.

KHALIL, H. K. 2002. *Nonlinear Systems*, Prentice Hall.

KIM, B., KIM, H., KIM, J. & YU, J. 2014. Computational fluid dynamic analysis in microbial fuel cells with different anode configurations.

KIM, G. T., WEBSTER, G., WIMPENNY, J. W. T., KIM, B. H., KIM, H. J. & WEIGHTMAN, A. J. 2006. Bacterial community structure, compartmentalization and activity in a microbial fuel cell. *Journal of Applied Microbiology,* 101**,** 698-710.

KIM, J. R., BOGHANI, H. C., AMINI, N., AGUEY-ZINSOU, K.-F., MICHIE, I., DINSDALE, R. M., GUWY, A. J., GUO, Z. X. & PREMIER, G. C. 2012. Porous anodes with helical flow pathways in bioelectrochemical systems: The effects of fluid dynamics and operating regimes. *Journal of Power Sources,* 213**,** 382-390.

KIM, J. R., MIN, B. & LOGAN, B. E. 2005. Evaluation of procedures to acclimate a microbial fuel cell for electricity production. *Applied Microbiology and Biotechnology,* 68**,** 23-30.

KIM, J. R., PREMIER, G. C., HAWKES, F. R., DINSDALE, R. M. & GUWY, A. J. 2009. Development of a tubular microbial fuel cell (MFC) employing a membrane electrode assembly cathode. *Journal of Power Sources,* 187**,** 393-399.

KIM, J. R., PREMIER, G. C., HAWKES, F. R., RODRÍGUEZ, J., DINSDALE, R. M. & GUWY, A. J. 2010. Modular tubular microbial fuel cells for energy recovery during sucrose wastewater treatment at low organic loading rate. *Bioresource Technology,* 101**,** 1190-1198.

KIM, J. R., RODRIGUEZ, J., HAWKES, F. R., DINSDALE, R. M., GUWY, A. J. & PREMIER, G. C. 2011a. Increasing power recovery and organic removal efficiency using extended longitudinal tubular microbial fuel cell (MFC) reactors. *Energy & Environmental Science,* 4**,** 459-465.

KIM, Y., HATZELL, M. C., HUTCHINSON, A. J. & LOGAN, B. E. 2011b. Capturing power at higher voltages from arrays of microbial fuel cells without voltage reversal. *Energy & Environmental Science,* 4**,** 4662-4667.

KIRUBAKARAN, A., JAIN, S. & NEMA, R. K. 2009. A review on fuel cell technologies and power electronic interface. *Renewable and Sustainable Energy Reviews,* 13**,** 2430-2440.

KRISTINSSON, K. & DUMONT, G. A. 1992. System identification and control using genetic algorithms. *Systems, Man and Cybernetics, IEEE Transactions on,* 22**,** 1033-1046.

LARMINIE, J., DICKS, A. & MCDONALD, M. S. 2003. *Fuel cell systems explained*, Wiley New York.

LE BARS, M. & WORSTER, M. G. 2006. Interfacial conditions between a pure fluid and a porous medium: implications for binary alloy solidification. *Journal of Fluid Mechanics,* 550**,** 149-173.

LEWIS, K. 1966. Symposium on bioelectrochemistry of microorganisms. IV. Biochemical fuel cells. *Bacteriological reviews,* 30**,** 101.

LI, J., ZHANG, J., YE, D., ZHU, X., LIAO, Q. & ZHENG, J. 2014. Optimization of inner diameter of tubular bamboo charcoal anode for a microbial fuel cell. *International Journal of Hydrogen Energy*.

LIANG, D., SHEN, Q., HOU, M., SHAO, Z. & YI, B. 2009. Study of the cell reversal process of large area proton exchange membrane fuel cells under fuel starvation. *Journal of Power Sources,* 194**,** 847-853.

LIU, H. & LOGAN, B. E. 2004. Electricity Generation Using an Air-Cathode Single Chamber Microbial Fuel Cell in the Presence and Absence of a Proton Exchange Membrane. *Environmental Science & Technology,* 38**,** 4040-4046.

LIU, H., RAMNARAYANAN, R. & LOGAN, B. E. 2004. Production of Electricity during Wastewater Treatment Using a Single Chamber Microbial Fuel Cell. *Environmental Science & Technology,* 38**,** 2281-2285.

LIU, Y., HARNISCH, F., FRICKE, K., SIETMANN, R. & SCHRÖDER, U. 2008. Improvement of the anodic bioelectrocatalytic activity of mixed culture biofilms by a simple consecutive electrochemical selection procedure. *Biosensors and Bioelectronics,* 24**,** 1006-1011.

LJUNG, L. 1999. *System Identification: Theory for the User*, Prentice Hall PTR.

LJUNG, L. 2012. *System Identifiation Toolbox™ User's Guide,* Natick, MA, The MathWorks, Inc.

LOGAN, B., CHENG, S., WATSON, V. & ESTADT, G. 2007. Graphite Fiber Brush Anodes for Increased Power Production in Air-Cathode Microbial Fuel Cells. *Environmental Science & Technology,* 41**,** 3341-3346.

LOGAN, B. E., HAMELERS, B., ROZENDAL, R., SCHRÖDER, U., KELLER, J., FREGUIA, S., AELTERMAN, P., VERSTRAETE, W. & RABAEY, K. 2006. Microbial Fuel Cells: Methodology and Technology†. *Environmental Science & Technology,* 40**,** 5181-5192.

LOGAN, B. E. & REGAN, J. M. 2006. Electricity-producing bacterial communities in microbial fuel cells. *Trends in Microbiology,* 14**,** 512-518.

LOWY, D. A., TENDER, L. M., ZEIKUS, J. G., PARK, D. H. & LOVLEY, D. R. 2006. Harvesting energy from the marine sediment–water interface II: kinetic activity of anode materials. *Biosensors and Bioelectronics,* 21**,** 2058-2063.

LYON, D. Y., BURET, F., VOGEL, T. M. & MONIER, J.-M. 2010. Is resistance futile? Changing external resistance does not improve microbial fuel cell performance. *Bioelectrochemistry,* 78**,** 2-7.

MANOHAR, A. K., BRETSCHGER, O., NEALSON, K. H. & MANSFELD, F. 2008. The use of electrochemical impedance spectroscopy (EIS) in the evaluation of the electrochemical properties of a microbial fuel cell. *Bioelectrochemistry,* 72**,** 149-154.

MANUEL, M. F., NEBURCHILOV, V., WANG, H., GUIOT, S. R. & TARTAKOVSKY, B. 2010. Hydrogen production in a microbial electrolysis cell with nickel-based gas diffusion cathodes. *Journal of Power Sources,* 195**,** 5514-5519.

MARTIN, E., SAVADOGO, O., GUIOT, S. R. & TARTAKOVSKY, B. 2013. Electrochemical characterization of anodic biofilm development in a microbial fuel cell. *Journal of Applied Electrochemistry,* 43**,** 533-540.

MICHIE, I. S., KIM, J. R., DINSDALE, R. M., GUWY, A. J. & PREMIER, G. C. 2011. The influence of psychrophilic and mesophilic start-up temperature on microbial fuel cell system performance. *Energy & Environmental Science,* 4**,** 1011-1019.

MICHIE, I. S., KIM, J. R., DINSDALE, R. M., GUWY, A. J. & PREMIER, G. C. 2014. The influence of anodic helical design on fluid flow and bioelectrochemical performance. *Bioresource technology,* 165**,** 13-20.

MIN, B. & LOGAN, B. E. 2004. Continuous Electricity Generation from Domestic Wastewater and Organic Substrates in a Flat Plate Microbial Fuel Cell. *Environmental Science & Technology,* 38**,** 5809-5814.

MIN, B., ROMÁN, Ó. & ANGELIDAKI, I. 2008. Importance of temperature and anodic medium composition on microbial fuel cell (MFC) performance. *Biotechnology Letters,* 30**,** 1213-1218.

MINK, J. E., ROJAS, J. P., LOGAN, B. E. & HUSSAIN, M. M. 2012. Vertically grown multiwalled carbon nanotube anode and nickel silicide integrated high performance microsized (1.25 μL) microbial fuel cell. *Nano letters,* 12**,** 791-795.

MOHAN, S. V., RAGHAVULU, S. V., SRIKANTH, S. & SARMA, P. N. 2001. Bioelectricity production by mediatorless microbial fuel cell under acidophilic condition using wastewater as substrate: Influence of substrate loading rate. *Current Science,* 92**,** 1720-1726.

MOLOGNONI, D., PUIG, S., BALAGUER, M. D., LIBERALE, A., CAPODAGLIO, A. G., CALLEGARI, A. & COLPRIM, J. 2014. Reducing start-up time and minimizing energy losses of Microbial Fuel Cells using Maximum Power Point Tracking strategy. *Journal of Power Sources,* 269**,** 403-411.

MONTEBELLI, A., R., L., IEROPOULOS, I., MELHUISH, C., GREENMAN, J. & ZIEMKE, T. Year. Microbial Fuel Cell Driven Behavioral Dynamics in Robot Simulations. *In:* Proc. of the Alife XII Conference, 2010 Odense, Denmark.

NIEN, P.-C., LEE, C.-Y., HO, K.-C., ADAV, S. S., LIU, L., WANG, A., REN, N. & LEE, D.-J. 2011. Power overshoot in two-chambered microbial fuel cell (MFC). *Bioresource Technology,* 102**,** 4742-4746.

OH, S., KIM, J., JOO, J. & LOGAN, B. 2009. Effects of applied voltages and dissolved oxygen on sustained power generation by microbial fuel cells. *Water science and technology,* 60**,** 1311.

OH, S. E. & LOGAN, B. E. 2007. Voltage reversal during microbial fuel cell stack operation. *Journal of Power Sources,* 167**,** 11-17.

OH, S. T., KIM, J. R., PREMIER, G. C., LEE, T. H., KIM, C. & SLOAN, W. T. 2010. Sustainable wastewater treatment: How might microbial fuel cells contribute. *Biotechnology Advances,* 28**,** 871-881.

OLIVEIRA, V. B., SIMÕES, M., MELO, L. F. & PINTO, A. M. F. R. 2013. Overview on the developments of microbial fuel cells. *Biochemical Engineering Journal,* 73**,** 53-64.

PANT, D., VAN BOGAERT, G., DIELS, L. & VANBROEKHOVEN, K. 2010. A review of the substrates used in microbial fuel cells (MFCs) for sustainable energy production. *Bioresource Technology,* 101**,** 1533-1543.

PHAM, H. T., BOON, N., AELTERMAN, P., CLAUWAERT, P., DE SCHAMPHELAIRE, L., VAN OOSTVELDT, P., VERBEKEN, K., RABAEY, K. & VERSTRAETE, W. 2008. High shear enrichment improves the performance of the anodophilic microbial consortium in a microbial fuel cell. *Microbial Biotechnology,* 1**,** 487-496.

PICIOREANU, C., HEAD, I. M., KATURI, K. P., VAN LOOSDRECHT, M. C. M. & SCOTT, K. 2007. A computational model for biofilm-based microbial fuel cells. *Water Research,* 41**,** 2921-2940.

PINTO, R., SRINIVASAN, B., MANUEL, M.-F. & TARTAKOVSKY, B. 2010. A two-population bio-electrochemical model of a microbial fuel cell. *Bioresource technology,* 101**,** 5256-5265.

POTTER, M. C. 1911. Electrical Effects Accompanying the Decomposition of Organic Compounds. *Proceedings of the Royal Society of London. Series B, Containing Papers of a Biological Character,* 84**,** 260-276.

PREMIER, G., KIM, J. R., MICHIE, I., DINSDALE, R. & GUWY, A. 2011. Automatic control of load increases power and efficiency in a microbial fuel cell. *Journal of Power Sources,* 196**,** 2013-2019.

PREMIER, G. C., DINSDALE, R., GUWY, A. J., HAWKES, F. R., HAWKES, D. L. & WILCOX, S. J. 1999. A comparison of the ability of black box and neural network models of ARX structure to represent a fluidized bed anaerobic digestion process. *Water Research,* 33**,** 1027-1037.

RABAEY, K. 2009. Bioelectrochemical systems: a new approach towards environmental and industrial biotechnology. *Bioelectrochemical systems: from extracellular electron transfer to biotechnological application.* London: IWA Publishing.

RABAEY, K., BOON, N., SICILIANO, S. D., VERHAEGE, M. & VERSTRAETE, W. 2004. Biofuel Cells Select for Microbial Consortia That Self-Mediate Electron Transfer. *Applied and Environmental Microbiology,* 70**,** 5373-5382.

RABAEY, K., CLAUWAERT, P., AELTERMAN, P. & VERSTRAETE, W. 2005. Tubular Microbial Fuel Cells for Efficient Electricity Generation. *Environmental Science & Technology,* 39**,** 8077-8082.

RAMASAMY, R. P., REN, Z., MENCH, M. M. & REGAN, J. M. 2008. Impact of initial biofilm growth on the anode impedance of microbial fuel cells. *Biotechnology and Bioengineering,* 101**,** 101-108.

RICHTER, H., NEVIN, K. P., JIA, H., LOWY, D. A., LOVLEY, D. R. & TENDER, L. M. 2009. Cyclic voltammetry of biofilms of wild type and mutant Geobacter sulfurreducens on fuel cell anodes indicates possible roles of OmcB, OmcZ, type IV pili, and protons in extracellular electron transfer. *Energy & Environmental Science,* 2**,** 506-516.

RINALDI, A., MECHERI, B., GARAVAGLIA, V., LICOCCIA, S., DI NARDO, P. & TRAVERSA, E. 2008. Engineering materials and biology to boost performance of microbial fuel cells: a critical review. *Energy & Environmental Science,* 1**,** 417-429.

RINGEISEN, B. R., HENDERSON, E., WU, P. K., PIETRON, J., RAY, R., LITTLE, B., BIFFINGER, J. C. & JONES-MEEHAN, J. M. 2006. High Power Density from a Miniature Microbial Fuel Cell Using Shewanella oneidensis DSP10. *Environmental Science & Technology,* 40**,** 2629-2634.

RISMANI-YAZDI, H., CARVER, S. M., CHRISTY, A. D. & TUOVINEN, O. H. 2008. Cathodic limitations in microbial fuel cells: An overview. *Journal of Power Sources,* 180**,** 683-694.

ROTHAUSEN, S. G. S. A. & CONWAY, D. 2011. Greenhouse-gas emissions from energy use in the water sector. *Nature Climate Change,* 1**,** 210-219.

ROZENDAL, R. A., HAMELERS, H. V. & BUISMAN, C. J. 2006. Effects of membrane cation transport on pH and microbial fuel cell performance. *Environmental science & technology,* 40**,** 5206-5211.

RUGH, W. J. & SHAMMA, J. S. 2000. Research on gain scheduling. *Automatica,* 36**,** 1401-1425.

SCHAETZLE, O., BARRIÈRE, F. & SCHRÖDER, U. 2009. An improved microbial fuel cell with laccase as the oxygen reduction catalyst. *Energy & Environmental Science,* 2**,** 96-99.

SCHRÖDER, U. & HARNISCH, F. 2009. Electrochemical losses. *Bioelectrochemical systems: from extracellular electron transfer to biotechnological application.* London: IWA Publishing.

SRIKANTH, S., VENKATA MOHAN, S. & SARMA, P. N. 2010. Positive anodic poised potential regulates microbial fuel cell performance with the function of open and closed circuitry. *Bioresource Technology,* 101**,** 5337-5344.

STEIN, N. E., HAMELERS, H. M. V., VAN STRATEN, G. & KEESMAN, K. J. 2012. On-line detection of toxic components using a microbial fuel cell-based biosensor. *Journal of Process Control,* 22**,** 1755-1761.

STEYER, J.-P., BUFFIÈRE, P., ROLLAND, D. & MOLETTA, R. 1999. Advanced control of anaerobic digestion processes through disturbances monitoring. *Water Research,* 33**,** 2059-2068.

SUN, M., SHENG, G.-P., MU, Z.-X., LIU, X.-W., CHEN, Y.-Z., WANG, H.-L. & YU, H.-Q. 2009. Manipulating the hydrogen production from acetate in a microbial electrolysis cell–microbial fuel cell-coupled system. *Journal of Power Sources,* 191**,** 338-343.

TAN, K. C., LI, Y., MURRAY-SMITH, D. J. & SHARMAN, K. C. Year. System identification and linearisation using genetic algorithms with simulated annealing. *In:* Genetic Algorithms in Engineering Systems: Innovations and Applications, 1995. GALESIA. First International Conference on (Conf. Publ. No. 414), 12-14 Sep 1995 1995. 164-169.

TANIGUCHI, A., AKITA, T., YASUDA, K. & MIYAZAKI, Y. 2004. Analysis of electrocatalyst degradation in PEMFC caused by cell reversal during fuel starvation. *Journal of Power Sources,* 130**,** 42-49.

TER HEIJNE, A., HAMELERS, H. V., SAAKES, M. & BUISMAN, C. J. 2008. Performance of non-porous graphite and titanium-based anodes in microbial fuel cells. *Electrochimica Acta,* 53**,** 5697-5703.

WAEWSAK, C., NOPHARATANA, A. & CHAIPRASERT, P. 2010. Neural-fuzzy control system application for monitoring process response and control of anaerobic hybrid reactor in wastewater treatment and biogas production. *Journal of Environmental Sciences,* 22**,** 1883-1890.

WANG, H. P., KALCHEV, B., TIAN, Y., SIMEONOV, I., CHRISTOV, N. & VASSEUR, C. Year. Composed Adaptive Control for a second-order nonlinear model of a biotechnological process. *In:* Control & Automation (MED), 2011 19th Mediterranean Conference on, 20-23 June 2011 2011. 1140-1143.

WANG, X., FENG, Y., REN, N., WANG, H., LEE, H., LI, N. & ZHAO, Q. 2009. Accelerated start-up of two-chambered microbial fuel cells: Effect of anodic positive poised potential. *Electrochimica Acta,* 54**,** 1109-1114.

WATSON, V. J. & LOGAN, B. E. 2011. Analysis of polarization methods for elimination of power overshoot in microbial fuel cells. *Electrochemistry Communications,* 13**,** 54-56.

WEI, J., LIANG, P. & HUANG, X. 2011. Recent progress in electrodes for microbial fuel cells. *Bioresource technology,* 102**,** 9335-9344.

WEIDONG, X. & DUNFORD, W. G. Year. A modified adaptive hill climbing MPPT method for photovoltaic power systems. *In:* Power Electronics Specialists Conference, 2004. PESC 04. 2004 IEEE 35th Annual, 20-25 June 2004 2004. 1957-1963 Vol.3.

WILCOX, S., HAWKES, D., HAWKES, F. & GUWY, A. 1995. A neural network, based on bicarbonate monitoring, to control anaerobic digestion. *Water Research,* 29**,** 1465-1470.

WINFIELD, J., IEROPOULOS, I., GREENMAN, J. & DENNIS, J. 2011. The overshoot phenomenon as a function of internal resistance in microbial fuel cells. *Bioelectrochemistry,* 81**,** 22-27.

WOODWARD, L., TARTAKOVSKY, B., PERRIER, M. & SRINIVASAN, B. 2009. Maximizing power production in a stack of microbial fuel cells using multiunit optimization method. *Biotechnology Progress,* 25**,** 676-682.

YONG, Y.-C., DONG, X.-C., CHAN-PARK, M. B., SONG, H. & CHEN, P. 2012. Macroporous and monolithic anode based on polyaniline hybridized three-dimensional graphene for high-performance microbial fuel cells. *ACS nano,* 6**,** 2394-2400.

YOSHIDA, N., NAKAMURA, H., KARUBE, I., YANO, K., MORITA, T. & MCNIVEN, S. J. 2000. A mediator-type biosensor as a new approach to biochemical oxygen demand estimation. *The Analyst,* 125**,** 2280-2284.

YOU, S. J., ZHAO, Q. L., JIANG, J. Q., ZHANG, J. N. & ZHAO, S. Q. 2006. Sustainable Approach for Leachate Treatment: Electricity Generation in Microbial Fuel Cell. *Journal of Environmental Science and Health, Part A,* 41**,** 2721-2734.

YOUNG, P. C. 2011. Gauss, Kalman and advances in recursive parameter estimation. *Journal of Forecasting,* 30**,** 104-146.

ZHANG, B., FENG, C., NI, J., ZHANG, J. & HUANG, W. 2012. Simultaneous reduction of vanadium (V) and chromium (VI) with enhanced energy recovery based on microbial fuel cell technology. *Journal of Power Sources,* 204**,** 34-39.

ZHANG, P.-Y. & LIU, Z.-L. 2010. Experimental study of the microbial fuel cell internal resistance. *Journal of Power Sources,* 195**,** 8013-8018.

ZHANG, X.-C. & HALME, A. 1995. Modelling of a microbial fuel cell process. *Biotechnology Letters,* 17**,** 809-814.

ZHANG, Y. & ANGELIDAKI, I. 2012. Self-stacked submersible microbial fuel cell (SSMFC) for improved remote power generation from lake sediments. *Biosensors and Bioelectronics,* 35**,** 265-270.

ZHAO, F., RAHUNEN, N., VARCOE, J. R., ROBERTS, A. J., AVIGNONE-ROSSA, C., THUMSER, A. E. & SLADE, R. C. T. 2009a. Factors affecting the performance of microbial fuel cells for sulfur pollutants removal. *Biosensors and Bioelectronics,* 24**,** 1931-1936.

ZHAO, F., SLADE, R. C. T. & VARCOE, J. R. 2009b. Techniques for the study and development of microbial fuel cells: an electrochemical perspective. *Chemical Society Reviews,* 38**,** 1926-1939.

ZHUANG, L., YUAN, Y., WANG, Y. & ZHOU, S. 2012a. Long-term evaluation of a 10-liter serpentine-type microbial fuel cell stack treating brewery wastewater. *Bioresource technology,* 123**,** 406-412.

ZHUANG, L., ZHENG, Y., ZHOU, S., YUAN, Y., YUAN, H. & CHEN, Y. 2012b. Scalable microbial fuel cell (MFC) stack for continuous real wastewater treatment. *Bioresource Technology,* 106**,** 82-88.

ZHUANG, L. & ZHOU, S. 2009. Substrate cross-conduction effect on the performance of serially connected microbial fuel cell stack. *Electrochemistry Communications,* 11**,** 937-940.

ZUO, Y., CHENG, S., CALL, D. & LOGAN, B. E. 2007. Tubular Membrane Cathodes for Scalable Power Generation in Microbial Fuel Cells. *Environmental Science & Technology,* 41**,** 3347-3353.

11. Appendix A

The following material is supporting information for Chapter 3 (On improving initiation and the performance of MFC). The experiment for the start-up of H-type MFC was to verify if connecting the H-type MFC to the load value of 500 Ω during the start-up would facilitate the MFC-*Control* to start as early as MFC-MPPT.

11.1 Materials and Methods

Two identical H-type MFCs were set up as described in section 3.2.1. The inoculum was sieved through a 250 µm sieve to remove dirt and grit and remain the sludge particulates containing anaerobes. The anodes of MFCs were filled with inoculum in anaerobic environment inside the glove box (in contrast to section 3.2.1 where it was inoculated in aerobic environment) to remove the time lag due to natural air filled headspace in the anode chamber.

MFC-MPPT was connected to an MPPT load as described in section 3.2.2 but with a different digital potentiometer, X9C102PZ (Intersil® X9C102, Farnell UK Ltd., Leeds) and so the load values ranged from 28.4 Ω to 869 Ω. The starting load on MFC-MPPT was 500 Ω. MFC-*Control* was connected to a load of 500 Ω which seems like a more appropriate choice of load after the power measurement from identical system as in Chapter 3.

11.2 Results and discussion

Figure 11.1 shows power generation from MFC-MPPT and MFC-*Control* when they were connected to the variable electrical load (MPPT load) and a static load of 500 Ω, respectively. The red arrow on day 14 indicates when 10 mM acetate was injected in MFC-MPPT and intermittent gaps in the data indicates loss of data due to unexpected shut down of the personal computer. On day 6, 8, 9, 11, 12, 14, 16, 18, 19, 23 and 26, the MPPT was restarted since there was no perturbation in the load when the load climbed down to the minimum value and so it was unable to track the power and/or there was not enough substrate in the MFC to generate electrical power.

On day 6, the power rise was observed from MFC-MPPT (connected to virtually a constant load of 28.4 Ω) and therefore, the MPPT algorithm was restarted to provide perturbation so that gradient of the power can be calculated by the MPPT algorithm enabling it to track the power. It seems that the MFC on MPPT had started generating power between

day 5 and day 6 (current plot in Figure 11.1) and restarting the algorithm and it is clearly seen (Figure 11.2) that the MFC was generating similar power to the power seen from MFC-MPPT in Chapter 3. Also, the impedance load applied was about 400 Ω and it sustained for more than 1

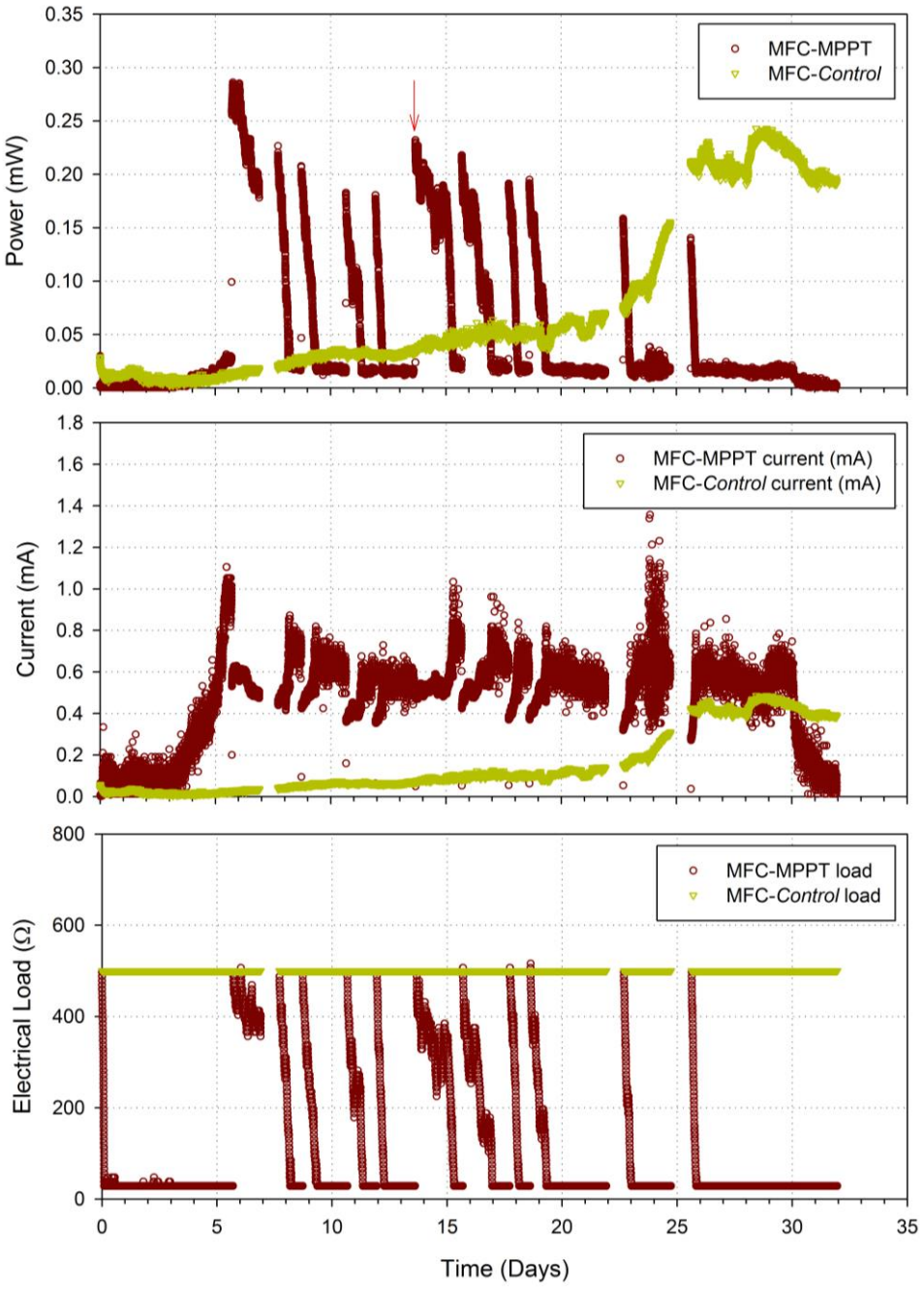

Figure 11.1: Electrical power and current generation from MFC-MPPT and MFC-*Control* during the start-up. Red arrow indicates when 10 mM substrate was added in the MFC-MPPT.

day after which, the personal computer had shut down and the data was not measured. After day 7.7, the MPPT was started couple of times but the MFC did not show any power so 10 mM acetate was injected in the MFC which allowed it to generate power for almost 2 days. If the

inoculums was discarded and fresh media was supplied to the MFC-MPPT, it would generate the power continuously like in between day 5.7 – 6.9 and also day 14 – 15. However, the electric current plot clearly indicates that the electric current generation had established since day 6 and hence the power generation from MFC-MPPT can be considered to have established from the day 6 onwards.

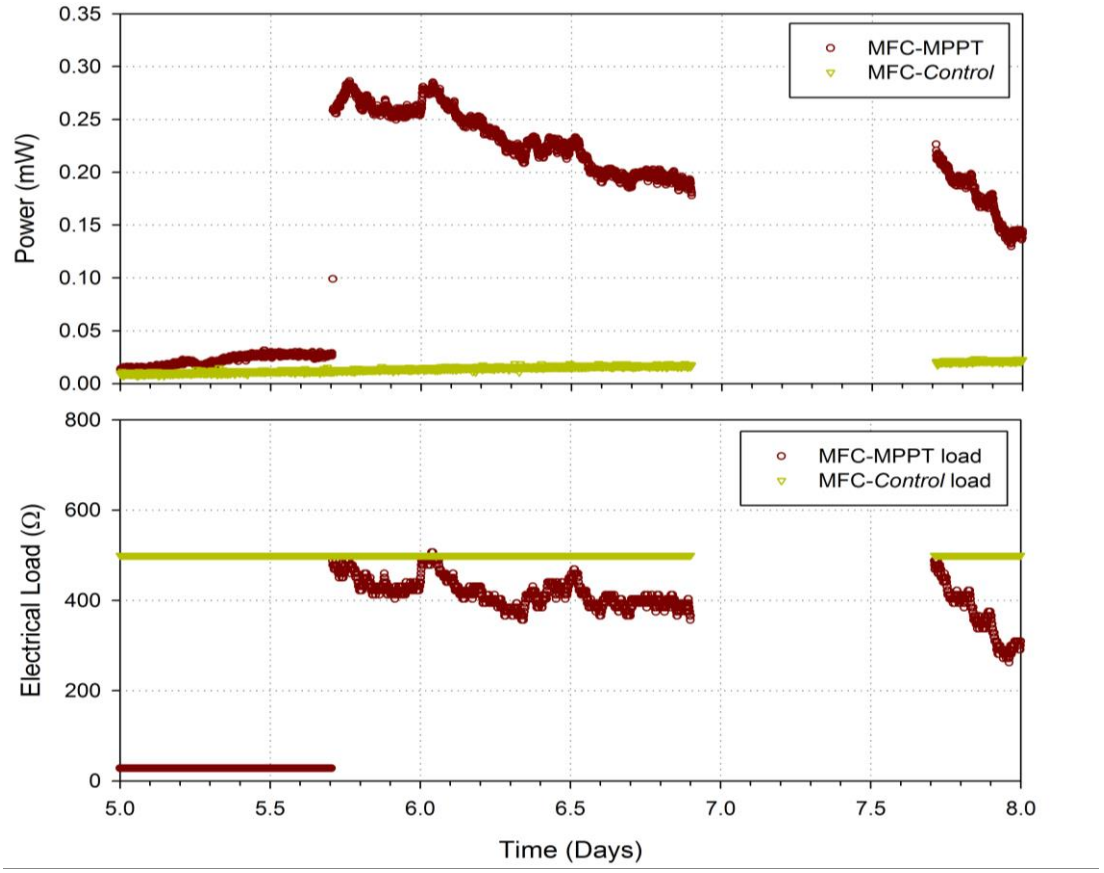

Figure 11.2: Electrical power and current generation from MFC-MPPT and MFC-*Control* during the day 5 – 8.

MFC-*Control* showed a slow rise in power until day 26 when the power generation seems to have established (Figure 11.1). This is even when static load of 500 Ω was used as opposed to 1 kΩ as in Chapter 6. This suggests that the relatively lower load than that of the impedance (when MFC is fully operational), facilitates early start-up. However, continuous impedance matching could further enhance the power performance of MFC.

12. Appendix B

12.1 List of journal publications associated with this study

1. KIM, J. R., BOGHANI, H. C., AMINI, N., AGUEY-ZINSOU, K.-F., MICHIE, I., DINSDALE, R. M., GUWY, A. J., GUO, Z. X. & PREMIER, G. C. 2012. Porous anodes with helical flow pathways in bioelectrochemical systems: The effects of fluid dynamics and operating regimes. *Journal of Power Sources,* 213**,** 382-390.
2. BOGHANI, H. C., KIM, J. R., DINSDALE, R. M., GUWY, A. J. & PREMIER, G. C. 2013. Analysis of the dynamic performance of a microbial fuel cell using a system identification approach. *Journal of Power Sources,* 238**,** 218-226.
3. BOGHANI, H. C., KIM, J. R., DINSDALE, R. M., GUWY, A. J. & PREMIER, G. C. 2013. Control of power sourced from a microbial fuel cell reduces its start-up time and increases bioelectrochemical activity. *Bioresource Technology,* 140**,** 277-285.
4. BOGHANI, H. C., PAPAHARALABOS, G., MICHIE, I., FRADLER, K. R., DINSDALE, R. M., GUWY, A. J., IEROPOULOS, I., GREENMAN, J. & PREMIER, G. C. 2014. Controlling for peak power extraction from microbial fuel cells can increase stack voltage and avoid cell reversal. *Journal of Power Sources,* 269**,** 363-369.

12.2 List of oral presentation at conference(s), associated with this study

1. BOGHANI, H. C., FRADLER, K., MICHIE, I., DINSDALE, R. M., GUWY, A. J. & PREMIER, G. C. Year. Enhanced microbial fuel cell performance from hybrid helical anode designed using multiphysics approach. *In:* World Renewable Energy Congress/Network, 03-04 August 2014 London.

12.3 List of poster presentations at conferences, associated with this study

1. BOGHANI, H. C., KIM, J. R., DINSDALE, R. M., GUWY, A. J. & PREMIER, G. C. Year. A parametric study of spiral electrodes in microbial fuel cells. *In:* 3rd International Microbial Fuel Cell Conference, 6-8 June 2011 Leeuwarden.
2. BOGHANI, H. C., KIM, J. R., DINSDALE, R. M., GUWY, A. J. & PREMIER, G. C. Year. Microbial Fuel Cell System Identification using PRBS. *In:* World Renewable Energy Forum, 13-17 May 2012 Denver, Colorado. American Solar Energy Society.

3. BOGHANI, H. C., KIM, J. R., DINSDALE, R. M., GUWY, A. J. & PREMIER, G. C. Year. Enhancement of Start-up and Performance of Microbial Fuel Cell Using Potential and Load Control Strategies. *In:* European International Society for Microbial Electrochemical Technologies Meeting, 27-28 September 2012 Ghent.
4. BOGHANI, H. C., MICHIE, I., DINSDALE, R. M., GUWY, A. J. & PREMIER, G. C. Year. Control of cell potential improves power extraction from microbial fuel cells in stacks. *In:* 11th IWA Conference on Instrumentation Control and Automation, 18-20 September 2013 Narbonne, France. IWA.